Sediment mobility in steep channels and the transition to landsliding

Thesis by

Jeff Prancevic

In partial fulfillment of the requirements for the degree of
Doctor of Philosophy in Geology

2016

California Institute of Technology
Pasadena, CA
Defended Dec 1, 2015

Acknowledgements

The work that I present in this dissertation and my success as a graduate student would not have been possible without the support of my advisors, colleagues, friends, and family.

First, my PhD advisor, Mike Lamb, has been a fantastic source of new ideas, inspiration, and advice to improve my abilities as a scientist. A side project that Mike completed during his PhD provided the impetus for the first flume experiments that I conducted at Caltech, which in turn provided the foundation for my entire dissertation. He has helped me develop and test hypotheses throughout the process, and his abilities as a scientist are those to which I constantly aspire.

Before coming to Caltech, I also had the great benefit of learning from Bill Dietrich. There is a reason why a disproportionate number of active researchers in geomorphology have origins at UC Berkeley. Bill's curiosity is contagious, and he is incredibly generous with both his time and ideas.

Three of the four enclosed chapters are based on flume experiments that I performed in the Caltech Earth Surface Dynamics Laboratory. I thank Brian Fuller for his tireless efforts to make things work in the lab. He built the original flume that I worked on throughout my PhD and helped me make modifications when necessary. Brian, along

with Marisa Palucis, Jabari Jones, Cindy Tran, and Connor O'Toole, also helped me conduct many of the flume experiments described in this dissertation.

Before I even knew what geomorphology was, a single email exchange that I had with Joel Scheingross in 2007 may have set me on my current career path. Since arriving at Caltech, Joel has been a great friend and my favorite person to nerd-out with on topics related to geomorphology.

The ever-evolving group of graduate students, post-docs, and visiting faculty studying geomorphology at Caltech has made for a dynamic and fun learning environment. I've learned a great amount by spending time in the field with Luca Malatesta, Joel Scheingross, Ryan Ewing, Roman DiBiase, Mathieu Lapôtre, and Ben Mackey. Long days and late nights in the flume lab were easier with the company of Austin Chadwick, Vamsi Ganti, and Phairot Chatanantavet. Alistair Hayden, Isaac Larsen, and Adam Booth were fantastic officemates. In our near-daily coffee breaks, Luca has been greatly supportive with anything from troubles with experiments to trouble with bicycles. During their visits to Caltech, Jeremy Venditti and Gary Parker shared important insights in flow hydraulics and sediment transport.

One of the greatest aspects of the division is it's collaborative spirit, and I have benefitted greatly from interactions outside of my own research group. In addition to being a supportive academic advisor, Jean-Philippe Avouac has a fantastic intuition for erosional processes and sediment transport, even if his primary expertise is in tectonics rather than geomorphology. François Ayoub has been incredibly patient in helping me with the technical details of processing optical imagery. My interactions with Victor Tsai, Florent Gimbert, and Maxime Farin have inspired me to think about the information that

we can extract from the seismic signals of bedload transport and debris flows. Melany Hunt has patiently listened to me try to explain my ideas on fluid and granular mechanics, and provided me with useful insights on slope stability. Woody Fischer has an incredible range of interests that make him a fun and inspiring person for geoscience discussions.

If I had spent all of my time in graduate school working, I may not have made it through. Adventuring with Alison, be it backpacking in the Sierras, eating in the SGV, or road-tripping up the coast, has been the best motivation for not working all the time. I owe a lot to Alison and all of my friends who kept me adequately distracted from research and a more balanced person. Fortunately, most of this debt can probably be paid with a day at the crag with Hayden, sneaking into the Langham hot tub with Brian, actually riding my bike with Luca, a lively political debate over beer with Stephen, a dance party with Sophie, livin' that aloha lifestyle with Frank, a night of grilling with Ted, making an overly involved dinner with Elizabeth, a game of pong with Max, and a day of surfing with Kyle, Jesse, Adam, and Kahner. All of which I will gladly do.

Finally, I thank my family for providing opportunities early on to develop a curiosity about the natural world to pursue an education in science. Family vacations were always centered around some outdoor activity, be it surfing, skiing, hiking, or snorkeling. These experiences instilled in me a fascination with the natural world in all of its complexities. In addition, my parents have always encouraged me to pursue a career that brings me joy, above all else. Also, although it was not conscious, it's hard to imagine that the experiences of my dad and brother fighting fires throughout California didn't influence my decision to work a bit on the sediment response to wildfires.

Thanks to all of you for your support.

Abstract

Our understanding of mountain evolution, landslide hazards, and long-term sediment budgets across earth's surface hinges on our ability to predict the necessary conditions for sediment transport in steep terrain. Empirical expectations for the onset of the transport of sediment by rivers have existed for 80 years. Similarly, models were developed almost 70 years ago to predict the occurrence of shallow landsliding driven by seepage flow through sediment beds. Initially, data to support these expectations was limited to low-gradient rivers (for river transport) or nonexistent (for landsliding). Over the past few decades, datasets have been collected from field and flume observations that suggest that sediment is more stable than expected in steep terrain, both in channel beds and steep hillslopes. Proposed explanations for this enhanced stability for both regimes include granular stability, sediment and root cohesion, altered hydraulics in steep and shallow flows, and morphologic form drag. However, the relative importance of these mechanisms has not been fully resolved within either regime. In addition, data on sediment mobility has remained extremely limited on slopes steeper than 5% or so.

To help resolve this debate, I have conducted several series of laboratory flume experiments to extend the database of sediment transport observations to untested slopes.

In Chapter 1 of this dissertation, I present the first set of controlled observations of sediment transport across the river-debris flow transition, with bed angles ranging from 1.8° to 33°. I identify the transition from river transport to landsliding for these experimental conditions at $\theta \approx 22°$ and suggest that this process transition could be predicted for natural channels using appropriate models for fluvial sediment transport and slope stability. Once predicted, this transitional slope could be used to identify source areas for catastrophic landslides and debris flows. However, consistent with previous observations my experiments show that sediment is always more stable than predicted by traditional transport models (for both fluvial transport and landsliding), limiting our predictive abilities. In order to improve our ability to predict the occurrence of sediment transport with both regimes, I spend the following three chapters identifying the mechanisms responsible for this enhanced stability.

In Chapter 2, I present the results of laboratory flume experiments that examine the effect shallow flow hydraulics in reducing sediment transport rates. By performing two experiment sets with grains of different densities ($\rho_s = 2.65$ g/cm^3 and $\rho_s = 1.15$ g/cm^3), I show that shallow flows are disproportionately weak at moving sediment, independent of changes in channel-bed slope. In Chapter 3, I directly test the hypothesis that grains have more frictional resistance to movement in steep channels by measuring the forces required to dislodge cobbles and boulders from eight natural channel beds in Southern California. Results indicate that grains in steep channel beds are not more stable, on average, than in lower-sloping environments. However, measurements indicate that coarse grains are more stable than typically assumed, and that boulder steps are more stable than surrounding grains. This indicates that grains are most stable where fluid stresses

are highest, providing a means to exert increased drag on the flow without the occurrence of sediment transport. Comparing the data in these two chapters with measurements of incipient sediment transport in natural channels indicates that most of the reduction in sediment transport rate observed in steep channels is due inefficient hydraulics inherent to shallow flows. The shear stresses required to mobilize sediment in natural channels are generally offset compared to those required in laboratory experiments, indicating that the drag exerted by immobile objects reduces sediment transport rates at all channel slopes.

In Chapter 4, I test for the cause of enhanced stability within the landsliding regime by conducting four additional sets of laboratory experiments. These experiments were designed to test for the relative importance of pore-water turbulence and friction along the margins of landslides in enhancing the stability of the experimental landslides of Chapter 1. Each experiment set used a different grain size, spanning Darcian and turbulent flow regimes. All experimental sets showed that sediment beds are far more stable than predicted by traditional slope stability models independent of grain size, indicating that grain size turbulence does not play a major role in the stability of slopes. However, by including the frictional stresses acting on the margins of the landslide (lateral walls and downslope toe), the slope stability model accurately predicted my experimental observations. This model requires some knowledge of the 3-D landslide geometry. However, these experiments reveal that landslides occur with a characteristic length-to-width ratio of 2:1 in the absence of topographic constraints. I also present a model to explicitly predict landslide depth if the surface geometry is known. Consequently, the saturation level required to initiate shallow landslides can be predicted if the landslide width can

be estimated.

Combined, these results provide new expectations for the conditions required to transport sediment by fluvial and landslide processes throughout steep landscapes (Fig. 1). These sediment transport predictions also provide mechanistic expectations for which mode of transport should dominate for a given topographic slope, allowing us to partition the landscape according to process regime (Figs. 1 and 2).

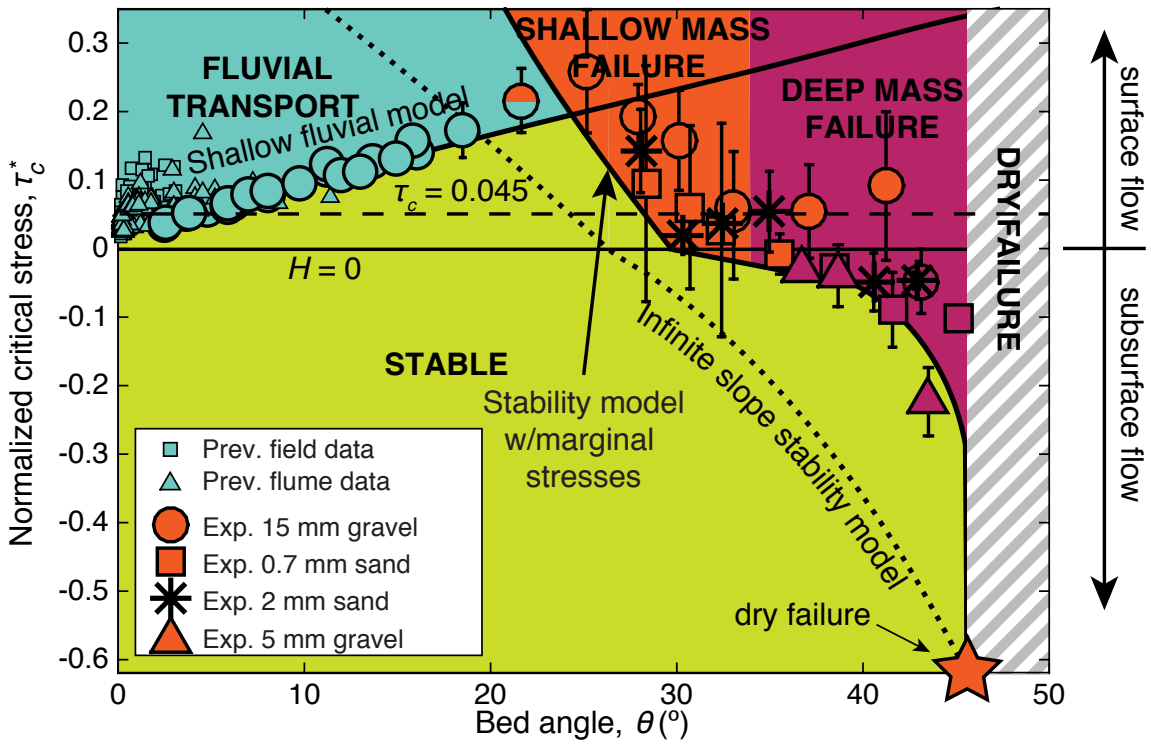

Figure 1: A new phase space for sediment transport throughout steep landscapes. This plot shows the critical Shields stress required to initiate sediment transport by both fluvial processes and shallow landslides. Most of the experimental observations presented in this dissertation are included in this figure (excluding the acrylic data from Chapter 2). Also shown is the previous compilation of flume and field observations of initial sediment motion. The model predictions presented herein allow the landscape to be partitioned according to transport regime by the local topographic slope, as indicated by the colored areas of the plot.

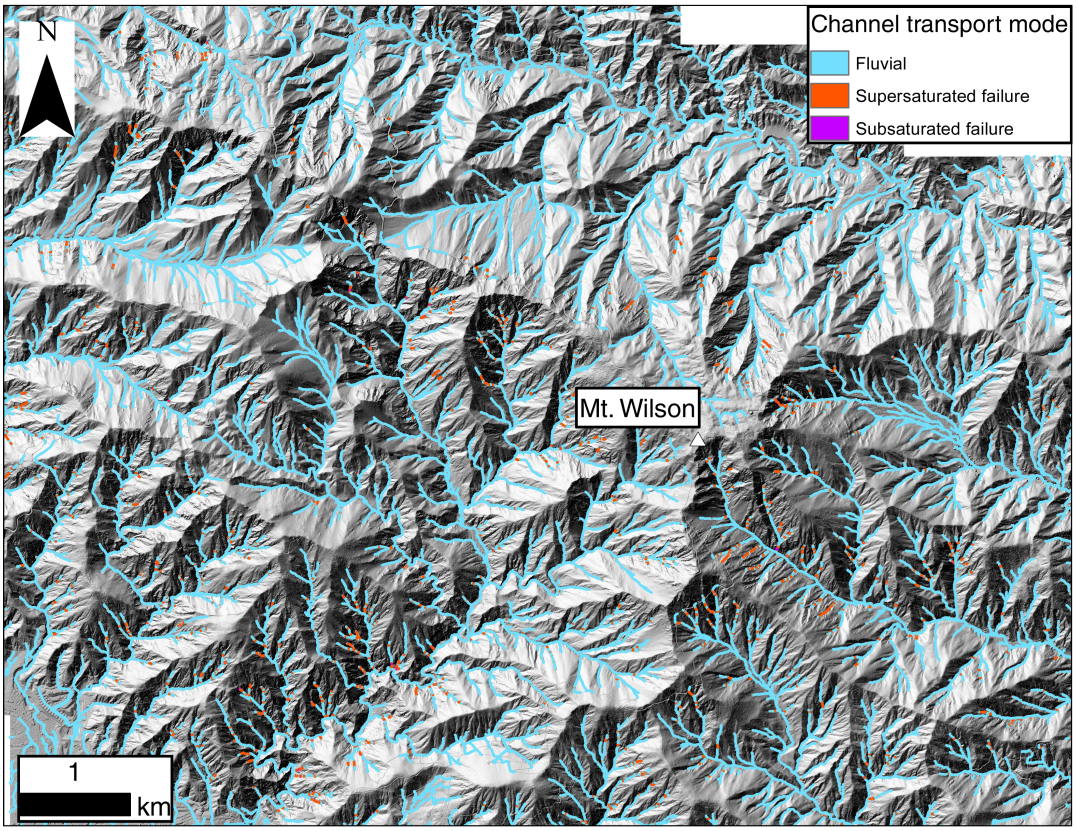

Figure 2: A hillshade map of the San Gabriel mountains in Southern California with channel segments color-coded according to process regime. This map utilizes the phase space presented in Fig. 1 to partition the drainage network according to transport regime as a function of the local channel slope. While the landslide channel segments occupy only a small portion of the drainage network, it is important to note that these channel segments are not capable of transporting sediment fluvially. Thus, if transport is to occur by flowing water in these segments, it will do so by catastrophic landslides that may develop into debris flows.

Published Content and Contributions

Prancevic, J. P., M. P. Lamb, and B. M. Fuller, (2014) Incipient sediment motion across the river to debris-flow transition, *Geology*, 42 (3), 191–194, doi: 10.1130/G34927.1

J.P.P. participated in the conception of the study, led the majority of experiments, processed the experimental data, and led in the writing of the manuscript.

Prancevic, J. P., and M. P. Lamb (2015), Unraveling bed slope from relative roughness in initial sediment motion, *J. Geophys. Res.*, 120 (3), 474–489, doi: 10.1002/2014JF003323

J.P.P. participated in the conception of the study, led the majority of experiments, processed the experimental data, and led in the writing of the manuscript.

Prancevic, J. P., and M. P. Lamb, (2015) Particle friction angles in steep mountain channels, *J. Geophys. Res.*, 120 (2), 242–259, doi: 10.1002/2014JF003286

J.P.P. participated in the conception of the study, participated in all field measurements, processed the field data, and led in the writing of the manuscript.

Contents

List of Figures

List of Tables

Introduction

0.1 Motivation

Understanding how rock, uplifted and exposed at earth's surface, is eroded and transported downstream is a fundamental goal of geomorphology. Our fascination with this problem is not drawn only from the grandeur of the resultant terrain, but also from practical concerns related to hazards and habitat, and the role of mountains in driving a variety of large-scale geologic processes. It is these concerns that warrant the continued investigation of the erosion and transport of sediment in mountainous terrain.

Over human timescales, mountainous terrain often has the appearance of being unchanging. Hiking around on most steep hillslopes, firm ground and well-established vegetation give the impression that this landscape is actually quite stable. We are bluntly reminded, however, that this is not always the case when catastrophic movements of sediment directly impact human life. Steep hillslopes in and out of mountainous terrain present formidable hazards to those living downslope in the form of shallow landslides and debris flows. At least at a qualitative level, the physical processes driving these failures are understood: we know that failures occur during intense rainfall and runoff

that can destabilize a mobile layer of soil. In practice, however, predicting the occurrence of these events remains a challenge. Part of the work presented herein is aimed at better understanding where shallow mass failures are expected to occur and the conditions required to initiate them.

Moving down from the steep interfluves of mountainous terrain and into the steep network of interconnected drainage channels, the movement of sediment becomes more apparent. Meter-scale levees of coarse rock fragments and boulders organized into steps give the sense that these deposits have been organized by flow events that were powerful enough to lift and carry boulders. Still, these coarse channel beds often feel firm beneath our feet, and repeated visits to the same steep channels often reveal that most of the cobbles and boulders remain in place, even if sand is actively transported by a flowing stream. While these channels may be capable of transporting sediment downstream by normal river processes, they do so rarely and some evidence suggests that the majority of transport in these very steep channels is still driven by extreme events in the form of debris flows. Again, deciphering the relative roles of fluvial and debris flow transport in these channels is difficult because we generally lack an understanding of the conditions required to mobilize sediment by these respective processes.

Moving further downslope still, only when the slope of the channel bed relaxes below a meager $\sim$5% do river channels achieve a somewhat well-organized bed with sediment grains sorted according to their size and regularly occurring bed topography. It is on these channels, and those downstream, that geomorphologists have historically focused most of their efforts, and we have a relatively good understanding of when sediment moves in these "low-sloping" channels. I should note, however, that $\sim$5% is still quite steep for

most people that study river channels. This is mostly for practical reasons, and very low-sloping rivers are demonstrably more important (at least directly) for a variety of humanitarian concerns. Human populations are centered around large lowland rivers, and rely on these rivers for water supplies, energy, and navigation. They also suffer greatly when these rivers swell and flood the human settlements that were opportunistically established on the banks.

Still, it is channels that are steeper than this that comprise the majority of mountain drainage networks, and thus bound the majority of mountain topography. This means that these steep channels are responsible for initially conveying most of the sediment that eventually arrives at lower-sloping rivers. In determining sediment supply to lower-sloping channels, steep channels play a key role in determining the equilibrium geometry and flood risks of larger rivers.

In addition, numerous studies have found that in rapidly uplifting, non-glaciated terrain the average slope of hillslopes is insensitive to the average erosion rate. This theory of "threshold hillslopes" suggests that hillslopes at their maximum angle will respond to changes in channel incision only by eroding more quickly or slowly while their relief remains the same. Instead, changes in relief can only occur by adjusting the slope of the channels draining the uplifting mountain range. Consequently, understanding what controls the incision of mountain channels is key to understanding both the total erosion rates of mountain belts and also the total relief.

Over long timescales, several researchers have shown that large-scale mountain-erosion patterns can interact with climate and tectonics in important ways. First, mountain topography will extract moisture from the atmosphere through orographic precipitation.

This increased precipitation can, in turn, enhance erosion rates and affect tectonic strains deeper in the lithosphere by inducing localized exhumation. Sufficiently high mountains can even affect global circulation patterns. Mountain erosion can also affect atmospheric chemistry through its crucial role in the silicate weathering cycle. All of these effects, however, require an understanding of how channels incise into mountain ranges, and incision into bedrock channels is primarily determined by the ability of water to mobilize sediment. The work presented in this dissertation is aimed at understanding how sediment is transported throughout steep drainage networks (dilute river transport vs. debris flows), measuring the conditions required to mobilize sediment within each regime, and improving our physical understanding of how fluid forces interact with solid sediment grains to mobilize them.

0.2 Background

Despite its broad relevance to natural hazards, downstream sediment supply, global tectonics, and global climate, the movement of sediment in steep channels and hillslopes has proven difficult to predict. Our development of theoretical predictions of both fluvial transport and landslide/debris flow initiation is primarily limited by a lack of observations in both the laboratory and the field, particularly at the moderately steep slopes that comprise the majority of mountain drainage networks.

Slope stability and fluvial sediment transport both have long histories of research interest, but over most of that history they were only considered within their end-member environments. That is, fluvial sediment transport was initially only studied in very

low-sloping rivers, while the stability of slopes to shallow landsliding was considered only on steep hillslopes that failed due to subsurface flow. The research approaches to understanding these two phenomenon were also very different.

Fluvial transport of riverbed sediment is difficult to predict for two important reasons: 1) the driving forces are derived from turbulent flowing water, for which no analytical description exists, and 2) the frictional resistance to transport for each grain is derived from a unique set of contact points with surrounding grains, each with their own size and shape. At the time when the first studies of sediment transport were first conducted, boundary layer theory had only recently been introduced and there were no quantitive estimates of the stresses imparted on a channel bed by flowing water. With both sides of the force balance seemingly unresolvable, the pioneering studies of sediment transport were restricted to observations in natural channels or laboratory flumes (e.g., Gilbert, 1914; Shields, 1936). Using dimensional analysis, relevant nondimensional metrics of stress and transport rates were developed, but the findings were strictly empirical. Shields (1936) cautioned that these relationships were not likely to hold in steep, shallow flows, but it would be several decades until observations were made to confirm this prediction and even then a single mechanistic explanation was elusive.

Shortly following the efforts by Shields (1936) to describe the hydraulic conditions required to move sediment in rivers, other researchers tried to predict the hydrologic and topographic conditions required to mobilize an entire mass of soil on a hillslope in the form of a shallow landslide (e.g. Taylor, 1948; Haefeli, 1948). Soil on hillslopes is typically fine-grained, and the subsurface flow moving through the pore space of this soil is rarely turbulent. In addition, because these failures occur as ensemble movements by definition,

much of the variability that results from grain size and shape for the case of fluvial transport is averaged out in the resulting resisting stress that stabilizes shallow landslides. Consequently, the stability of a hillslope to failure by elevated pore pressure could be calculated directly using simple force balance models and measured friction angles (e.g. Taylor, 1948; Haefeli, 1948). The most basic and foundational kind of slope stability model assumes an inclined planar slope that extends infinitely in the cross-slope and downslope directions. This so-called 'infinite-slope stability model' is simple 1-D force balance model. However, unlike fluvial transport, observations of the pore water required to initiate these failures were difficult to make, preventing any tests of this model. The infrequency of events, hazardous conditions, and lack of instrumentation made observations of the hydrologic conditions required to initiate failures on natural hillslopes nearly impossible. Laboratory-scale experiments were possible, but were never performed, perhaps because the model was so simple that it's validity was taken for granted. As a result, the pioneering studies of slope stability provided us with the opposite body of work compared with the first studies of fluvial transport: simple theoretical predictions without any rigorous observations to test those predictions.

Although sediment transport by dilute water flow (fluvial transport) and shallow landsliding are fundamentally distinct in their granular behavior, both ultimately result from flowing water and gravity pulling sediment downslope. The tendency for one mode of transport to dominate over the other is simply due to the relative contribution of gravitational and fluid forces acting on the grains. Turbulent fluid forces vary both spatially and temporally, episodically concentrating stresses on a small portion of the bed to transport one or a few grains. Gravity, on the other hand, exerts a steady and

uniform force on all grains, leaving the entire sediment mass in a similarly unstable (or stable) condition. Consequently, as slopes become steeper and the gravitational force pulling grains downslope becomes stronger, then shallow landsliding is expected to dominate. Below some transitional slope where turbulent fluid force become more important, fluvial transport should dominate.

The first recognition of this theoretical transition occurred in the 1970s when researchers began to measure sediment transport on steep slopes (Ashida et al., 1973; Aguirre-Pe, 1975; Mizuyama, 1977) and to think about how catastrophic debris flows were initiated (Takahashi, 1978). Importantly, Takahashi (1978) proposed that shallow landslides were not limited to the steep regime where shallow landslides occur only with subsurface seepage flow. Instead, he hypothesized that mass movement of sediment could occur at lower slopes (although still relatively steep), where the stress from flow over the bed surface would more easily initiate a very shallow landslide (one grain layer) rather than transporting sediment fluvially. However, when Takahashi (1981) combined theories for fluvial transport and shallow landsliding, he discovered that the transition between these two transport regimes still occurred at a slope very close to the saturated angle of repose. This suggested that initial sediment motion should either occur by fluvial transport or shallow landsliding initiated by subsurface flow only and the transition between the two should occur at the saturated angle of repose. These predictions have remained unverified, however, because observations of sediment transport by either fluvial process or shallow landsliding have mostly remained limited to slopes lower than 10°. In this dissertation I show that Takahashi's surface mass failures occupy a distinct transport regime that exists only because fluvial transport becomes very inefficient on steep slopes,

allowing shallow landslides to occur prior to fluvial transport at relatively low slopes.

Following these brief investigations into the fluvial-debris flow process transition, research efforts shifted towards lower slopes (mostly less than 5%), where there have been several studies aimed at better understanding fluvial transport in moderately steep channels. Numerous observations of sediment transport in steep flumes (Bathurst et al., 1984; Olivero, 1984; Graf et al., 1987; Torri et al., 1988; Aguirre-Pe et al., 1991; Picon, 1991; Gregoretti, 2008) and steep field sites (Bartnick, 1991; Mueller, E R et al., 2005; Lenzi et al., 2006; Bunte et al., 2013; Scheingross et al., 2013) have consistently shown that sediment requires *higher* shear stresses to initiate transport on *steeper* slopes, even after accounting for differences in grain diameter and grain weight. This observation is peculiar, as our intuition suggests that sediment on steep slopes should be more precarious than on lower slopes. A considerable amount of work has attempted to explain this phenomenon, and while I will not discuss them in detail here, discussions can be found in Chapters 2 and 3 of this dissertation. Broadly, though, three distinct mechanisms have been suggested to explain this counterintuitive observation: 1) large flow obstacles (woody debris, immobile boulders, bed morphology) exert extra drag on the flow (e.g., Zimmermann et al., 2001; Yager et al., 2007), 2) there may be changes in the granular stability of some beds (e.g., Church et al., 1998), and 3) shallow flows distribute stress less effectively for sediment transport (e.g., Shields, 1936; Lamb et al., 2008; Recking, 2009). In this dissertation I extend the database of observations of initial sediment motion to the steepest slopes possible in Chapter 1. I then use flumes experiments and field measurements to test for the relevant contribution of each of the three proposed mechanisms in stabilizing sediment on steep slopes in Chapters 2 and 3.

Over the past several decades, there has also been many observations of shallow landsliding. These observations include induced landslides using artificial rainfall on natural hillslopes (Ochiai et al., 2004; Montgomery et al., 2009) and failures in laboratory flumes (Moriwaki, 1993; Yagi et al., 1987; Reid et al., 1997; Iverson et al., 2000; Okura et al., 2002; Wang et al., 2003; Moriwaki et al., 2004). Most of these studies were not designed explicitly as a test of the infinite slope stability model and violate the key model assumption of having slope-parallel seepage. In other studies, key information is not reported, including insufficient information on soil characteristics and hydrological conditions at the time of failure. In the few studies where slope stability could be tested against the infinite slope model, the results revealed that slopes were far more stable than predicted. Similar to the increased stability observed within the fluvial regime, multiple mechanisms have been proposed to explain this enhanced stability. For field observations, enhanced stability is most commonly explained by root cohesion (e.g., Waldron et al., 1981; Schmidt et al., 2001; Montgomery et al., 2009). Recently, there has also been increased recognition of the role that wall and toe stresses might play in stabilizing hillslopes or channel beds (e.g., Dietrich et al., 2007; Montgomery et al., 2009; Milledge et al., 2014). In Chapters 1 and 4 of this dissertation I present a new database of controlled landslide observations that extend from the fluvial-debris flow transition up to the dry angle of repose. Using these results, in Chapter 4 I assess the role of frictional stresses acting on the walls and toes in stabilizing shallow landslides.

Overall, this dissertation is aimed at testing and improving predictions for the conditions required to mobilize sediment on steep channels and hillslopes, and identifying which modes of transport should dominate in specific parts of the landscape. Combined,

results from these four chapters provide new expectations for the conditions required to initiate sediment transport in both the fluvial and mass failure regimes of steep mountain topography. Somewhat surprisingly, all results indicate that sediment is generally more stable than researchers normally predict. This suggests that sediment likely moves less often than we might assume, and that rare transport events likely play an important role in shaping landscapes, delivering sediment to lowland rivers, and altering wildlife and human habitat.

0.3 References

Aguirre-Pe, J (1975). "Incipient erosion in high gradient open channel flow with artificial roughness elements." In: *Proc 16th Congr Int Assoc Hydraul Res San Paulo Brazil* 2, pp. 137–180.

Aguirre-Pe, J and R Fuentes (1991). "Movement of big particles in steep, macro-rough streams." In: *Proc 24th Congr Int Assoc Hydraul Res Madrid, Spain*, pp. 149–158.

Ashida, K and M Bayazit (1973). "Initiation of motion and roughness of flows in steep channels." In: *Hydraul Res, Proc 15th Congress, Istanbul, Turkey* 1, pp. 475–484.

Bartnick, W (1991). "Determination of the critical conditions of incipient motion of bed load in mountain rivers." In: *Fluvial Hyraulics in Mountain Regions*. Ed. by Aronne Armanini and G Di Silvio. Springer-Verlag, Berlin, pp. 83–88.

Bathurst, J C, H H Cao, and W H Graf (1984). *Hydraulics and sediment transport in a steep flume: Data from the EPFL study*. Tech. rep. Wallingford, U.K.

Bunte, Kristin et al. (2013). "Critical Shields values in coarse-bedded steep streams." In: *Water Resources Research* 49.11, pp. 7427–7447.

Church, Michael, Marwan A Hassan, and John F Wolcott (1998). "Stabilizing self-organized structures in gravel-bed stream channels: Field and experimental observations." In: *Water Resources Research* 34.11, pp. 3169–3179.

Dietrich, WE et al. (2007). "The prediction of shallow landslide location and size using a multidimensional landslide analysis in a digital terrain model." In: *C. L. Chen and J.J. Major (editors), Debris-Flow Hazards Mitigation: Mechanics, Prediction, and Assessment: Proceedings 4th International DFHM Conference, Chengdu, China, September 10-13, 2007*, pp. 1–12.

Gilbert, G K (1914). "The transportation of debris by running water." In: *US Geol. Surv. Prof Pap* 86, p. 263.

Graf, W H and L Suszka (1987). "Sediment transport in steep channels." In: *J. HydroSci. Hydraul. Eng.* 5.1, pp. 11–26.

Gregoretti, C (2008). "Inception sediment transport relationships at high slopes." In: *Journal of Hydraulic Engineering* 134.11, pp. 1620–1629.

Haefeli, R (1948). "The stability of slopes acted upon by parallel seepage." In: *International Conference on Soil Mechanics and Foundation Engineering*, pp. 57–62.

Iverson, R M et al. (2000). "Acute sensitivity of landslide rates to initial soil porosity." In: *SCIENCE* 290.513.

Lamb, Michael P, William E Dietrich, and Jeremy G Venditti (2008). "Is the critical Shields stress for incipient sediment motion dependent on channel-bed slope?" In: *Journal Of Geophysical Research-Earth Surface* 113.F2, F02008.

Lenzi, M A, L Mao, and F Comiti (2006). "When does bedload transport begin in steep boulder bedded streams?" In: *Hydrological Processes* 20, pp. 3517–3533.

Milledge, David G et al. (2014). "A multidimensional stability model for predicting shallow landslide size and shape across landscapes." In: *Journal Of Geophysical Research-Earth Surface* 119.11, pp. 2481–2504.

Mizuyama, T (1977). "Bedload transport in steep channels." PhD thesis. Kyoto University.

Montgomery, David R et al. (2009). "Instrumental record of debris flow initiation during natural rainfall: Implications for modeling slope stability." In: *Journal Of Geophysical Research-Earth Surface* 114.F, F01031.

Moriwaki, H (1993). "Behavior of pore-water pressure at slope failure." In: *Proceedings of the seventh International Conference and Field Workshop on Landslides in Czech and Slovak Republics. Landslides, Balkema, Rotterdam.* Proceedings of the Seventh International Conference & Field Workshop on Landslides, pp. 263–268.

Moriwaki, H et al. (2004). "Failure processes in a full-scale landslide experiment using a rainfall simulator." In: *Landslides* 1.4, pp. 277–288.

Mueller, E R, J Pitlick, and J M Nelson (2005). "Variation in the reference Shields stress for bed load transport in gravel-bed streams and rivers." In: *Water Resources Research* 41.4, W04006.

Ochiai, Hirotaka et al. (2004). "A fluidized landslide on a natural slope by artificial rainfall." In: *Landslides* 1.3, pp. 211–219.

Okura, Yoichi et al. (2002). "Landslide fluidization process by flume experiments." In: *Engineering Geology* 66.1-2, pp. 65–78.

Olivero, M (1984). “Movimiento incipiente de partículas en flujo torrencial.” In: *Special Report: University of Los Andes, Meridad, Venezuela*, pp. 1–169.

Picon, G A (1991). “Estudio experimental de transporte sedimentos en rios de montaña.” PhD thesis. Merida, Venezuela: Universidad de Los Andes.

Recking, A (2009). “Theoretical development on the effects of changing flow hydraulics on incipient bed load motion.” In: *Water Resources Research* 45, W04401.

Reid, ME, RG LaHusen, and RM Iverson (1997). “Debris-flow initiation experiments using diverse hydrologic triggers.” In: *Debris-Flow Hazards Mitigation, Proceedings, C. Chen, ed., American Society of Civil Engineers*, pp. 1–11.

Scheingross, Joel S et al. (2013). “Influence of bed patchiness, slope, grain hiding, and form drag on gravel mobilization in very steep streams.” In: *Journal Of Geophysical Research-Earth Surface* 118, pp. 1–20.

Schmidt, K M et al. (2001). “The variability of root cohesion as an influence on shallow landslide susceptibility in the Oregon Coast Range.” In: *Canadian Geotechnical Journal* 38.5, pp. 995–1024.

Shields, A (1936). “Anwendung der Ähnlichkeitsmechanik und der Turbulenzforschung auf die Geschiebebewegung.” In: *Mitt. Preuss Versuchsanst. Wasserbau Schiffbau* 26.

Takahashi, T (1978). “Mechanical Characteristics of Debris Flow.” In: *J Hydr Eng Div-ASCE* 104.HY8, pp. 1153–1169.

— (1981). “Debris flow.” In: *Annual Review of Fluid Mechanics* 13, pp. 57–77.

Taylor, D W (1948). *Fundamentals of Soil Mechanics*. New York, NY: John Wiley & Sons.

Torri, D and J Poesen (1988). "Incipient motion conditions for single rock fragments in simulated rill flow." In: *Earth Surface Processes and Landforms* 13.3, pp. 225–237.

Waldron, L J and Suren Dakessian (1981). "Soil Reinforcement by Roots: Calculation of Increased Soil Shear Resistance From Root Properties." In: *Soil Science* 132.6, p. 427.

Wang, Gonghui and Kyoji Sassa (2003). "Pore-pressure generation and movement of rainfall-induced landslides: effects of grain size and fine-particle content." In: *Engineering Geology* 69.1-2, pp. 109–125.

Yager, E M, J W Kirchner, and W E Dietrich (2007). "Calculating bed load transport in steep boulder bed channels." In: *Water Resources Research* 43.7, W07418.

Yagi, N and R Yatabe (1987). "Prediction method of slope failure in sandy soil due to rainfall." In: *Proceedings, 8th Asian Regional Conference on Soil Mechanics and Foundation Engineering*, pp. 217–220.

Zimmermann, A and M Church (2001). "Channel morphology, gradient profiles and bed stresses during flood in a step-pool channel." In: *Geomorphology* 40, pp. 311–327.

Chapter 1

Incipient sediment motion across the river to debris-flow transition

This chapter was adapted from the peer-reviewed journal article:

Prancevic, J. P., M. P. Lamb, and B. M. Fuller, (2014) Incipient sediment motion across the river to debris-flow transition, *Geology*, 42 (3), 191–194, doi: 10.1130/G34927.1

Abstract

Sediment transport in mountain channels controls the evolution of mountainous terrain in response to climate and tectonics and presents major hazards to life and infrastructure worldwide. Despite its importance, we lack data on when sediment moves in steep channels and whether movement occurs by rivers or debris flows. We address this knowledge gap using laboratory experiments on initial sediment motion that cross the river to debris-flow sediment-transport transition. Results show that initial sediment motion

by river processes requires heightened dimensionless bed shear stress (or critical Shields stress) with increasing channel-bed slope by as much as fivefold the conventional criterion established for lowland rivers. Beyond a threshold slope of $\sim 22^{\circ}$, the channel bed fails, initiating a debris flow prior to any fluvial transport, and the critical Shields stress within the debris-flow regime decreases with increasing channel-bed slope. Combining theories for both fluvial and debris-flow incipient transport results in a new phase space for sediment stability, with implications for predicting fluvial sediment transport rates, mitigating debris-flow hazards, and modeling channel form and landscape evolution.

1.1 Introduction

Outside of glaciated regions, channel morphology (e.g., Montgomery et al., 1997) and landscape response to changes in climate and tectonics (e.g., Howard, 1994; Stock et al., 2003) are determined by sediment transport within channels by rivers and debris flows. Fluvial sediment transport occurs through fluid-particle interactions in rivers that result in rolling, saltation, or dilute suspensions (e.g., Shields, 1936). Debris flows, on the other hand, are highly concentrated slurries where solid and fluids are intermixed and both influence motion (e.g., Iverson et al., 1997). Although the physics of fluvial and debris-flow transport are distinct, we lack observations of when sediment moves in very steep channels and where initial sediment motion by one mode of transport dominates over the other. Consequently, most landscape-scale models do not differentiate these two important processes (e.g., Howard et al., 1994), and debris-flow hazard predictions rely on site-specific, multiple-regression techniques (e.g., Coe et al., 2008).

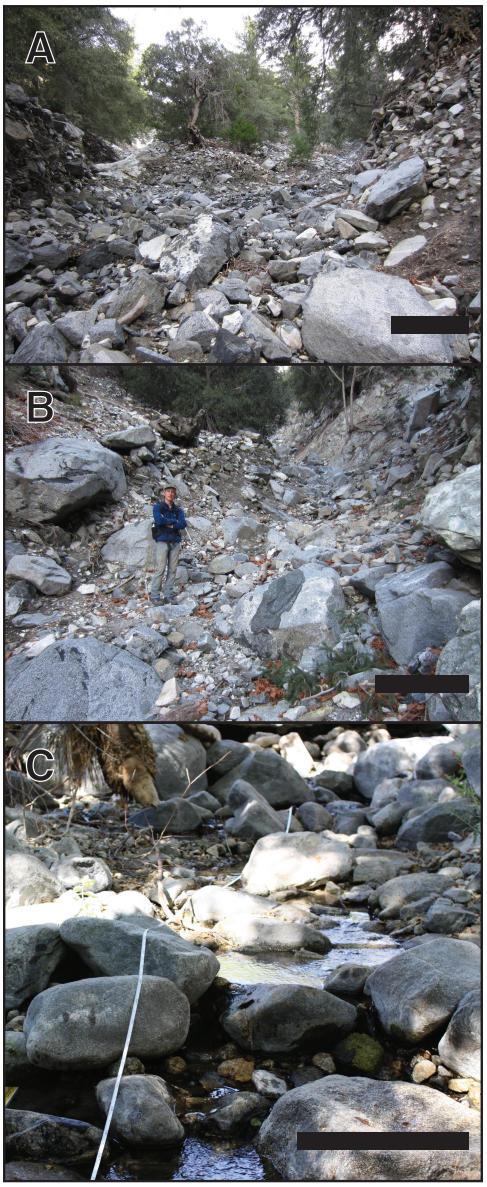

Figure 1.1: Photographs from steep channels in the San Gabriel Mountains, CA, USA (A & B: 34°14'50" N, 118°06'03" W; C: 34°15'58"N, 118°08'38" W). Scale bars correspond to approximately one meter in the foreground. A) Channel reach with a bed slope of 31° containing unsorted, angular boulders and cobbles with no apparent development of fluvial bed morphology. B) Channel reach at bed slope of 24° where boulders are more rounded and are sorted into more uniform distributions within the active channel. C) Channel reach at bed slope of 3.2° exhibiting fluvial step-pool bedforms with steps composed of rounded boulders and finer grains present in the pools.

There is a paucity of data on sediment motion in channels steeper than $\theta = 6°$, where θ is the channel-bed angle. Classic theoretical models for initial sediment motion by river

processes indicate that sediment transport occurs at lower near-bed fluid stresses (τ) with increasing bed slope due to the increased component of gravity acting on sediment in the downstream direction (e.g., Wiberg et al., 1987), consistent with experiments in sealed ducts (e.g., Chiew et al., 1995). Limited field and experimental data (Zimmermann et al., 2001; Mueller, E R et al., 2005; Gregoretti, 2008; Scheingross et al., 2013) and more recent theory (e.g., Lamb et al., 2008; Recking, 2009) suggest the opposite, however: sediment transport is less efficient in steep channels, as compared to lowland rivers, possibly due to bedforms such as step pools (Fig. 1.1), changes in the hydrodynamics of shallow, rough flows, or incomplete submergence of grains during transport.

Field observations indicate that debris flows can dominate bedrock incision in very steep channels ($\theta > 6°$) and control the supply of sediment to channels downstream (e.g., Benda et al., 2005) (Fig. 1.1). For example, topographic analyses indicate that the power-law scaling between channel slope and drainage area expected for river incision does not exist at very steep slopes, with the transition occurring between $\theta = 6°$ to $35°$ in different landscapes (e.g., Dibiase et al., 2012), potentially signifying the onset of debris-flow transport (Stock et al., 2003). Debris flows can be triggered on hillslopes from shallow landslides (e.g., Iverson, 1997) or within channels due to bulking and failure of the channel bed (e.g., Takahashi, 1978; Gregoretti, 2000; Tognacca et al., 2000; Coe et al., 2008). The latter mechanism must control initial sediment motion in channels steeper than a critical slope, but this slope has yet to be identified. Herein we show results from exploratory experiments designed to identify the onset of sediment motion for a range of steep channel slopes that cross the river to debris-flow transition.

1.2 Experimental design and rationale

We conducted 44 experiments in a 5-m-long tilting flume (Fig. 1.2) with variable channel widths (35 and 13 cm) and 19 bed slopes ranging from $\theta = 1.8°$ to 33° (Table 1.1). In natural channels, mixed sediment sizes and bedforms can influence initial sediment motion, and both these effects have been explored previously (e.g., Parker et al., 1982; Zimmermann et al., 2010). Here we focus on isolating the effect of channel-bed slope on initial sediment motion by using a planar bed of natural, well-sorted, semi-angular river gravel with a median intermediate grain diameter (D) of 1.5 cm. The grain size was chosen to achieve a sufficiently high particle Reynolds number,

$$Re_p \equiv \left(\frac{\tau}{\rho}\right)^{1/2} \frac{D}{\nu} \tag{1.1}$$

where $\tau = \rho g H \sin\theta$ is the spatially and temporally averaged basal shear stress from surface flow, H is flow depth, g is gravitational acceleration, $\rho = 1000$ kg/m^3 is water density, and ν is the kinematic viscosity of water, such that viscosity and particle size do not affect initial motion (Shields, 1936). All experiments were repeated 24 times to assess error and natural variability.

We incrementally increased the water discharge (by 5%–15%; measured using a flow meter), pausing for 35 min at each discharge for measurements of sediment transport. In experiments with fluvial transport, we measured the volumetric sediment flux per unit width, q_b, for 13 min using a trap (Fig. 1.2). As in previous work (e.g., Parker et al., 1982), the dimensionless bedload flux,

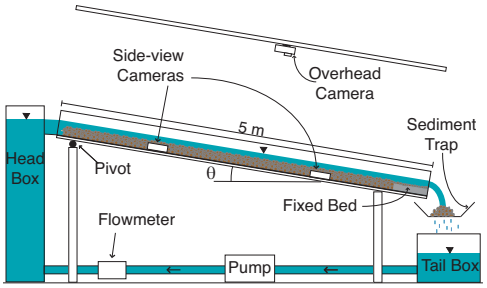

Figure 1.2: Flume schematic. Not to scale. In experiments with fluvial transport we used the sediment trap for one to three minutes beginning two minutes after each increase in discharge. Total discharge was measured using a flow meter in the plumbing. The overhead camera was used to track dye pulses in order to measure flow velocity. The photographs used to map sediment-water and water-air interfaces were taken with the side-view cameras.

$$q_b^* = \frac{q_b}{\sqrt{\frac{\rho_s - \rho}{\rho} g D^3}} \tag{1.2}$$

was a nonlinear function of the dimensionless bed stress, or Shields stress,

$$\tau^* = \frac{\tau}{(\rho_s - \rho) g D} \tag{1.3}$$

where $\rho_s = 2650$ kg/m^3 is sediment density. The critical Shields stress at initial motion, τ_c^*, was calculated by interpolating a power-law fit between τ^* and q^* to a standard reference transport rate of $q^* = 6.3 \times 10^{-5}$ corresponding to near initial-motion conditions (Parker et al., 1982) (Fig. 1.4). Average flow velocity was calculated by tracking pulses of dye. Non-Darcian subsurface discharge was calculated using a calibrated Forchheimer relation (Forchheimer, 1901) (Fig. 1.3). Flow depth (H) was calculated by one or both of the following methods (see Table 1.1): mapping and differencing sediment-water and water-air interfaces in side-view photographs at two locations (Fig. 1.6); or using continuity, flow velocity, and surface-flow discharge (i.e., differencing fully saturated subsurface discharge from total water discharge). For cases in which both methods were used, the

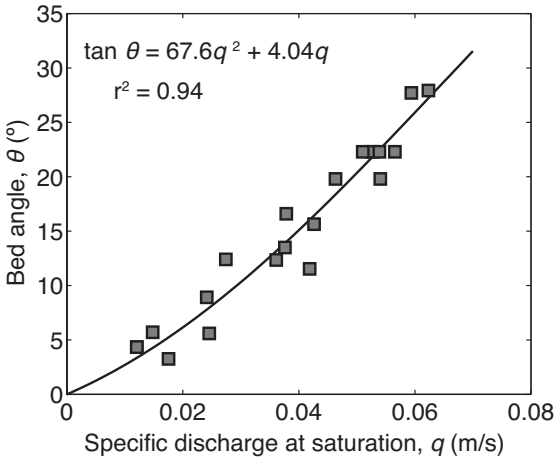

Figure 1.3: Bed slope as a function of measured saturated subsurface discharge. Because of the high Reynolds numbers in the experiments (200 to 750), the linear Darcy relationship for subsurface discharge does not hold. Instead, we use a calibrated Forchheimer equation, shown in the upper left corner, to calculate the subsurface discharge for each slope. This equation is the best-fit second-degree polynomial (solid black line) to the displayed data. Surface-flow discharge was calculated by subtracting the sub-surface discharge using the calibrated Forchheimer equation from the total discharge.

difference between the two flow-depth methods was less than 30%, error that is smaller than variance between repeat experiments. There was no sediment feed, and experiments were ceased when sediment transport significantly altered the bed surface from its initial planar configuration to avoid the influence of bedforms.

To characterize the mode of transport we collected video from cameras oriented orthogonal to the flume's clear sidewall. We made measurements of grain displacement by running statistical correlations between successive frames using a 10-pixel (5 mm) correlation window in COSI-Corr software (Leprince et al., 2007). These maps were reduced to vertical velocity profiles by summing the total displacement in the rows and dividing by the number of columns and the elapsed time. Short video clips (Movies DR1 and DR2) provided 122 and 194 independent frames for particle correlations (25 fps) for fluvial transport and bed failure, respectively (Fig. 1.6).

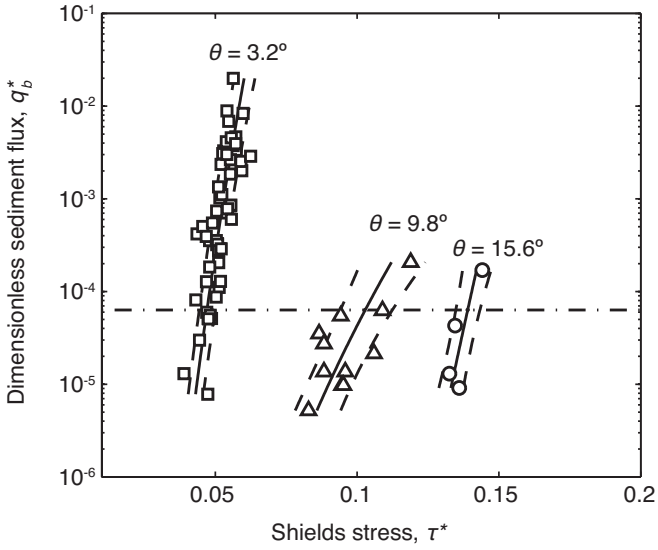

Figure 1.4: Dimensionless sediment flux (q^*) for experiments with fluvial transport at three different slopes (θ) as function of dimensionless shear stress (Shields stress, τ^*). Solid lines are power-law fits and sub-parallel dashed lines represent 50% confidence limits. Critical Shields stress for each slope is defined at a reference dimensionless sediment flux for near-initial motion conditions (Parker et al., 1982) (horizontal dashed line).

The fluvial sediment transport models (Lamb et al., 2008; Wiberg et al., 1987) require an input of grain-pocket friction angle (ϕ_g). The friction angles of individual grains were measured by gluing a single layer of the grains to a flat surface, placing individual loose grains on the glued grains, and tilting until the test grain dislodged (Miller and Byrne, 1966). We performed two series of measurements: one in which 24 individual grains were placed in 10 numbered pockets each (totaling 240 measurements) and another in which random grains were dropped on the board (56 measurements). The first series of measurements yielded an average friction angle of $\phi_g = 59.3° \pm 14.0°$, and the second gave $\phi_g = 57.0° \pm 12.4°$. The value reported in the main text, $\phi_g = 58.8° \pm 13.7°$, is the average of all experiments.

To apply the Takahashi (1978) bed-failure model the failure plane was assumed to

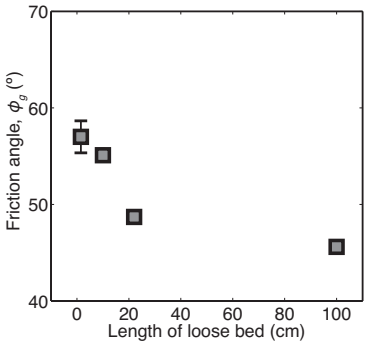

Figure 1.5: Bed friction angle as function of the length of the loose bed. Each data point is representative of a series of tilt table experiments in which one or several loose particles were placed on a bed of fixed gravel. For the case with a 1.5 cm length of loose bed, a single particle with $D = 1.5$ cm was dropped at random on a bed and allowed to settle before tilting the bed. The experiments with longer loose beds were performed by having two layers of glued particles on the tilt table, the second acting as a downstream buttress to the length of loose grains. The error bars represent the standard error of the experiment series, and are hidden behind symbols where errors are small.

be at one grain diameter depth as advocated by Takahashi (1978). Porosity was measured by comparing material density to bulk density with similar grain packing as in the experimental flume and found to have a value of 0.43. It is not clear how to measure the friction angle of the failure plane (ϕ_f) for the discrete failures we observed in our experiments and we tried a number of different methods. 1) We built a tilting chute with the same width as our experimental flume (13-cm) but only 1 m long to allow for very steep slopes. Following the setup for the initial motion experiments, we screed a planar, 10 cm-thick bed and then tilted the short flume slowly until a dry granular avalanche occurred. We performed this test ten times and the experiments yielded an avalanche angle of $\phi_f = 45.6° \pm 1.6°$ (100 cm bed length in Fig. 1.5). With such a low avalanche angle, the Takahashi model underpredicts stability from our experiments. 2) To test for the effect of water lubrication and buoyancy, we performed the same tests with the 1-m long chute but this time completely submerged in static water. The average friction angle

measured was $\phi_f = 45.4°$, within one standard deviation of the dry measurements. 3) To test whether the length of the chute influenced the friction angle, we performed a single experiment in which we placed a dry screed bed in the larger flume used for experiments and raised the upstream end until the bed failed. The resulting avalanche angle was $\phi_f = 44.5°$, within the range reported for the first series of experiments. 4) Finally, to mimic our observed experimental failure conditions in which a single layer initially fails with some discrete length, we modified our short flume accordingly: we glued two layers of gravel at the lower half of the tilt table, and only a single layer of gravel in the upper half of the tilt table. We placed variable amounts of loose gravel extended upstream of the double-thick gravel and performed similar tilting experiments as above. The resulting avalanche angles were $\phi_f = 48.9° \pm 1.2°$ for a 22-cm length, 1-grain diameter deep loose bed, and $\phi_f = 55.1° \pm 3.16°$ for a 10-cm length, 1-grain diameter deep loose bed (Fig. 1.5). All cases had a 13-cm chute width. We chose the latter angle for use in the Takahashi model, because these relatively short failure initiations are what we most commonly observed in our experiments (e.g., Movie DR4).

1.3 Results

Initial sediment motion for experiments with $1.8° < \theta < 19.6°$ occurred by river processes in which individual particles rolled and bounced along the bed driven by dilute surface flow (Fig. 1.6; Movie DR1 in the Data Repository). Although sediment transport is typically assumed to be a function of the Shields stress (τ^*) only (e.g., Parker et al., 1982), our data show a clear shift to larger Shields stresses with steeper channel slopes

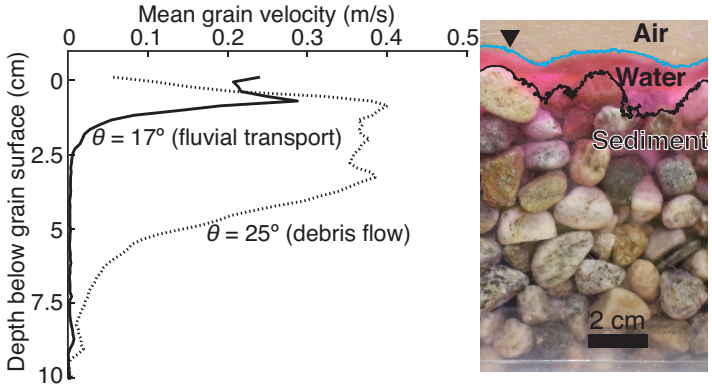

Figure 1.6: Grain velocity profiles in experiment with fluvial sediment transport (channel-bed angle $\theta = 17°$) and mass failure of bed ($\theta = 25°$), and side-view photograph of experimental bed with same vertical scale. Grain velocities were calculated using an autocorrelation routine applied to side-view videos (Leprince et al., 2007) (Movies DR1 and DR2). Grain velocities for fluvial case and at initiation of bed failure exist only within first grain layer (∼1.5 cm). Bed failures developed into debris flows and entrained underlying grains, to depth of about five grains (∼7.5 cm) for example shown. Photograph shows air-water (blue) and water-gravel (black) interfaces, which we identified semi-automatically with user-defined threshold values for each image that were used to calculate flow depths in some experiments (Table 1.1).

for the same sediment flux (Fig. 1.4). Results show a marked increase in the critical Shields stress with channel slope from values typical of lowland rivers ($\tau_c^* = 0.035$ at $\theta = 1.8°$) (e.g., Buffington et al., 1997) to a value nearly 5 times as large at steep slopes (e.g., $\tau_c^* = 0.16$ at $\theta = 19.6°$; Fig. 1.7). Thus, counter-intuitively, sediment transport by river processes requires larger bed stresses on steeper slopes despite the increased component of gravity acting on the grains in the downslope direction.

Table 1.1: List of experimental conditions and measurements. For cases in which both flow-depth methods were used, the difference between them was less than 30%, error that is smaller than variance between repeat experiments. We found that both flow-depth methods worked well for low slopes, but favored the continuity method because it did not require labor-intensive image analysis. For the steepest slopes ($\theta > 22°$) we favored the interface-mapping method for depth as subsurface flow dominated the total discharge, resulting in larger error in calculated surface-flow discharge.

Bed angle θ (°)	Channel width (cm)	Number of experiments	Number of sediment flux measurements	Depth measurement method	Particle Reynolds Number, Re_p	Mode of Transport	Flow depth, H (cm)	Critical Shields stress, τ_c^*
1.8	35	1	7	Continuity	1350	River	2.63	0.034
3.2	35	2	17	Continuity	1612	River	2.11	0.047
5.6	35	5	37	Continuity	1820	River	1.54	0.061
5.9	13	2	12	Both	1856	River	1.52	0.063
6.8	35	1	10	Continuity	2025	River	1.57	0.075
8	35	5	17	Continuity	2087	River	1.42	0.08
9.8	35	3	11	Continuity	2243	River	1.34	0.093
11.5	13, 35	3, 1	4, 1	Both	2463	River	1.38	0.113
12.4	35	2	5	Continuity	2413	River	1.23	0.109
13.5	35	2	3	Continuity	2485	River	1.2	0.116
14.2	13	2	3	Both	2569	River	1.22	0.125
15.6	35	1	4	Continuity	2701	River	1.23	0.139
16.9	13	2	5	Both	2715	River	1.15	0.141
19.6	13	2	5	Both	3029	River	1.24	0.178
22.3	13	2	N/A	Interface mapping	3273	Transitional	1.28	0.211
25.2	13	2	N/A	Interface mapping	3426	Bed failure	1.25	0.238
27.9	13	2	N/A	Interface mapping	2909	Bed failure	0.82	0.176
30.1	13	2	N/A	Interface mapping	2618	Bed failure	0.62	0.145
33	13	2	N/A	Interface mapping	1550	Bed failure	0.2	0.053

In experiments with $\theta > 25.2°$, initial sediment motion occurred by mass failure of the bed (Fig. 1.6; Movies DR2DR4) prior to any fluvial sediment transport. For these cases, collections of many grains mobilized together with the initial failure plane occurring within one or two grain diameters of the bed surface, and extending 10 cm in the streamwise direction (Movie DR4). Bed failures mobilized into debris flows in which sediment and water were well mixed, and the dilute surface flow present at initial bed failure was mixed into the slurry (Movies DR2 and DR3). The debris flows often developed well-defined frontal snouts, and at very steep slopes would entrain sediment and run out through the end of the flume, and at lesser slopes would thicken, dewater, and stabilize. Unlike the fluvial transport regime, the Shields stress at initial sediment motion by bed failure decreased with increasing channel-bed slope from its maximum value of $\tau_c^* = 0.24$ at $\theta = 25.2°$ to $\tau_c^* = 0.053$ at $\theta = 33.0°$, indicating a rapid decline in bed stability at steeper slopes (Fig. 1.7).

Experiments at $\theta = 22.3°$ exhibited both transport behaviors, with fluvial sediment transport occurring in some parts of the flume and small failures occurring elsewhere, representing a mixed transport regime. Therefore, $\theta \approx 22°$ is the threshold slope in our experiments for the transition from initial motion by river to debris-flow transport.

Flume data for $\theta < 19.6°$ are consistent with the models of Lamb et al. (2008) and Recking (2009) that predict increased τ_c^* with increasing bed slope due to changes in surface-flow hydrodynamics and partially submerged grains in shallow, rough flows, and are inconsistent with models that do not consider these effects (Wiberg et al., 1987) (Fig. 1.7). Rather than changes in hydrodynamics, other workers have attributed enhanced sediment stability in steep channels to interlocking across the channel width or changes

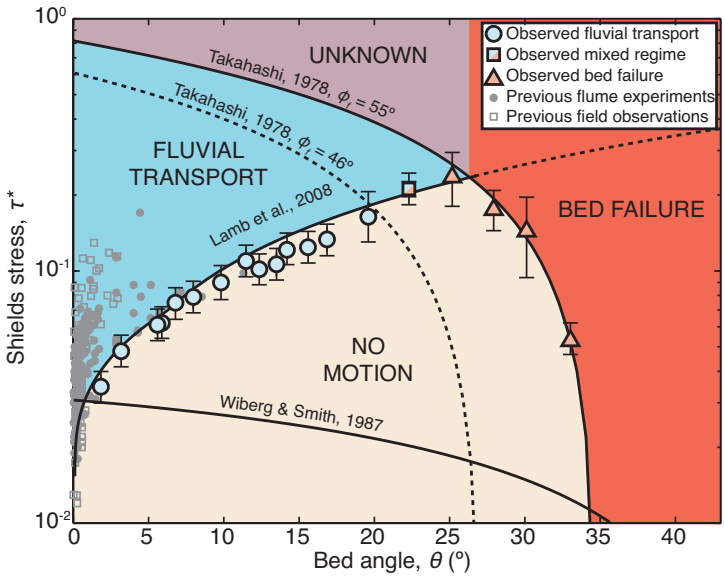

Figure 1.7: Experimental data of Shields stress at initial sediment motion as function of bed angle for both fluvial transport and bed failure. Error bars are 50% confidence limits for fluvial transport, and range of observed values for repeat bed failure experiments. Also shown are data from previous compilations (Lamb et al., 2008; Buffington et al., 1997) of initial sediment motion by fluvial transport including both field and laboratory observations. Curves are model predictions for incipient fluvial transport by Lamb et al. (2008) (dotted line shows model prediction within observed bed failure regime) and Wiberg et al. (1987), and bed-failure model of Takahashi (1978) using failure-plane friction angle (ϕ_f) equal to bulk angle of repose (dashed line) and equal to what we measured for a loose patch of grains, $\phi_f = 55°$ (solid line). Data support division of parameter space into conditions that produce no sediment motion, fluvial sediment transport, and bed failure. Data are not available to test mode of transport at shallow slopes and very large Shields stresses within regime marked "unknown".

in bed morphology (e.g., step-pool bedforms) (e.g., Zimmermann et al., 2010), or the presence of large immobile grains that increase flow resistance (Yager et al., 2007). These mechanisms cannot explain our results because our experiments had loose, planar beds of uniform grain sizes, and we observed no influence on incipient motion with changing channel width (Table 1.1).

Despite good agreement with the fluvial-sediment transport model for $\theta < 19.6$, Lamb et al. (2008) predict heightened τ_c^* values up to 0.4 at slopes that approach the grain-

pocket friction angle of $\phi_g = 58.8°$, which was not the case in our experiments due to the transition to bed failure at $\theta \approx 22°$. Instead, we compare the bed failure data to an infinite-slope, Mohr-Coulomb stability model in which the gravitational body force acting downslope on the groundwater and surface flow are balanced by frictional stress borne by the sediment grains (Takahashi, 1978) (Fig. 1.7). The model of Takahashi (1978) can be recast in terms of a critical Shields stress,

$$\tau_c^* = (1 - \eta)(\tan \phi_f - \tan \theta) - \frac{\rho}{\rho_s - \rho} \tan \theta, \tag{1.4}$$

where η is porosity, and we find that the model under-predicts our data when the failure-plane friction angle (ϕ_f) is set to the angle of repose ($\phi_f = 46°$). Alternatively, the model matches the data using a larger failure-plane friction angle ($\phi_f = 55°$), which is consistent with our measurements for a collection of loose grains of similar number to the observed failures (Fig. 1.7). It is also possible that the offset between data and model is due to turbulent subsurface flow, although the momentum balance of Takahashi (1978) does not require an explicit assumption of Darcian flow.

1.4 Discussion and Conclusions

Our results suggest that the threshold slope for initial sediment motion by debris-flow transport can be calculated by setting equal the transport models of Lamb et al. (2008) and Takahashi (1978) for specific failure-plane and grain-pocket friction angles. Given natural variability in these two friction angles [e.g., $\phi_f = 40°$ to $60°$ (Selby, 1993, p. 354); $\phi_g = 50°$ to $70°$ (Miller et al., 1966)], we expect the transitional slope in natural

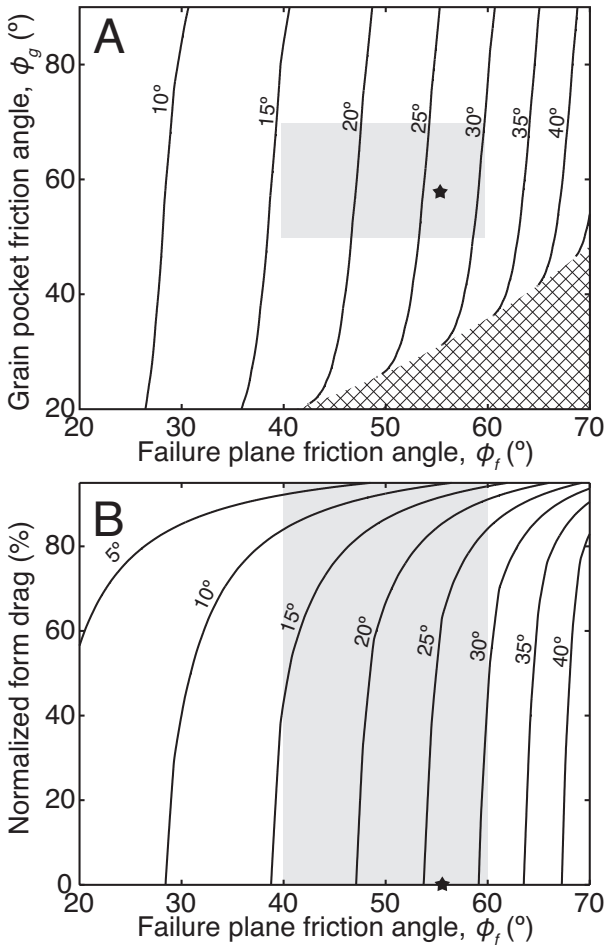

Figure 1.8: Contours of transitional slope between initial motion by fluvial and bed failure as calculated by matching models of Lamb et al. (2008) and Takahashi (1978) (e.g., Fig. 1.7) as function of grain-pocket friction angle (ϕ_g) and failure-plane friction angle (ϕ_f) with no drag due to bedforms (A), and as function of percentage form drag due to bedforms relative to total bed stress and failure-plane friction angle with constant 58.8° grain-pocket friction angle (B). Shaded regions denote range of parameter space likely in natural channels and black stars denote our experiments. Crosshatched region of A is model parameter space for dry bed failure.

channels to range from $\theta \approx 15°$ to 30° (Fig. 1.8A), which is consistent with the observed change in slopedrainage area relationships at these slopes (e.g., Stock et al., 2003; Dibiase et al., 2012). As in our experiments, failure plane friction angles may be a function of failure size for coarse-grained natural channels due to the effects of particle force chains (e.g., Cates et al., 1998). The transition from fluvial to debris-flow transport can also be

affected by drag due to flow separation behind bedforms or immobile boulders (i.e., form drag) in natural channels (Fig. 1.1). For example, an increase in form drag from 40% to 90% of the total bed stress corresponds to a decrease in the calculated transitional slope from $\theta = 22°$ to 13° (Fig. 1.8B). Thus, the propensity for in-channel debris-flow initiation on steep slopes results from both the reduced effectiveness of fluvial transport and the increased effectiveness of subsurface and surface flow in destabilizing the sediment bed en masse.

The threshold slope for the transition to bed failure defines the steepest-sloping channels in which river processes play a role in sediment transport and channel incision. Channels with $\theta > 25°$ are typically devoid of river-sorted sediment, and instead contain poorly sorted colluvium, rockfall, or debris-flow deposits (e.g., Fig. 1.1). This notwithstanding, debris flows influence channel processes at lesser slopes ($\theta < 25°$) because, even if initiated within steep channel reaches, they can run out long distances and across channels with slopes as little as $\theta = 1°$ (e.g., Iverson et al., 1997). In addition, Figure (1.7) suggests that mass failure of channel beds can occur at slopes lower than the transitional slope if Shields stresses during floods surpass substantially the critical value for fluvial transport (i.e., $\tau^* \rightarrow 1$). Shields stresses that substantially exceed the threshold for motion are rare in coarse-bedded rivers (e.g., Parker et al., 2007), but may occur due to infrequent, large-magnitude floods (which increase τ^* by increasing τ), or due to abrupt pulses of fine sediment (which increase τ^* by decreasing D). The latter mechanism may partly explain the propensity for debris flows (or debris floods) following landslides or wildfire (e.g., Coe et al., 2008; Lamb et al., 2011), for example, where hillslope-derived pulses of sediment can effectively resurface channels with finer sediment.

A quantitative framework for initial sediment motion across the river-debris flow transition allows for more realistic treatment of erosion and sediment transport in landscape-evolution models and hazard-mitigation efforts by providing process partitions in the landscape. Given that channels typically adjust their geometries to pass sediment at bed stresses that just exceed that required for initial sediment motion (e.g., Parker et al., 2007), the fivefold increase in the critical Shields stress near the transitional slope, as compared to the value typically assumed based on lowland river studies, provides new expectations of river form and may explain why sediment-transport models drastically over-predict sediment flux in steep channels (e.g., Rickenmann, 1997). Finally, our study adds to increased recognition of the role, in landscape evolution and mountain hazards, of debris flows initiated in-channel rather than on hillslopes (e.g., Takahashi, 1978; Gregoretti, 2000; Tognacca et al., 2000; Coe et al., 2008).

Acknowledgments

Funding was provided by National Science Foundation grant EAR-0922199, the Terrestrial Hazards Observations and Reporting center (THOR) at Caltech, and the Keck Institute for Space Studies. We thank C. Tran and C. O'Toole for help with experiments. Thanks to Editor J. Spotila, M. Church, and an anonymous reviewer for formal reviews, and R. Iverson, J. Andrade, N. Lapusta, and J.-P. Ampuero for helpful informal suggestions.

1.5 References

Benda, Lee et al. (2005). "Geomorphology Of Steepland Headwaters: The Transition From Hillslopes To Channels." In: *Journal of the American Water Resources Association* 41.4, pp. 835–851.

Buffington, J M and D R Montgomery (1997). "A systematic analysis of eight decades of incipient motion studies, with special reference to gravel-bedded rivers." In: *Water Resources Research* 33.8, pp. 1993–2029.

Cates, M E et al. (1998). "Jamming, Force Chains, and Fragile Matter." In: *Physical review letters* 81.9, pp. 1841–1844.

Chiew, Yee-Meng and G Parker (1995). "Incipient Sediment Motion on Non-Horizontal Slopes - Reply." In: *Journal of Hydraulic Research* 33.5, pp. 729–730.

Coe, J A, D A Kinner, and J W Godt (2008). "Initiation conditions for debris flows generated by runoff at Chalk Cliffs, central Colorado." In: *Geomorphology* 96.3-4, pp. 270–297.

Dibiase, Roman A, Arjun M Heimsath, and Kelin X Whipple (2012). "Hillslope response to tectonic forcing in threshold landscapes." In: *Earth Surface Processes and Landforms* 37.8, pp. 855–865.

Forchheimer, P H (1901). "Wasserbewegun Durch Boden." In: *Zeitschrift des Vereines Deutscher Ingenieure* 49-50, pp. 1736–1749–1781–1788.

Gregoretti, C (2000). "Experimental evidence from the triggering of debris flow along a granular slope." In: *Physics And Chemistry Of The Earth Part B-Hydrology Oceans And Atmosphere* 25.4, pp. 387–390.

Gregoretti, C (2008). "Inception sediment transport relationships at high slopes." In: *Journal of Hydraulic Engineering* 134.11, pp. 1620–1629.

Howard, A D (1994). "A detachment-limited model of drainage basin evolution." In: *Water Resources Research* 30.7, pp. 2261–2285.

Howard, A D, W E Dietrich, and M A Seidl (1994). "Modeling fluvial erosion on regional to continental scales." In: *J. Geophys. Res* 99.B7, pp. 13–971–13–986.

Iverson, R M, M E Reid, and R G LaHusen (1997). "Debris-flow mobilization from landslides." In: *Annual Review of Earth and Planetary Sciences* 25, pp. 85–138.

Iverson, RM (1997). "The physics of debris flows." In: *Reviews of Geophysics* 35.3, pp. 245–296.

Lamb, Michael P, William E Dietrich, and Jeremy G Venditti (2008). "Is the critical Shields stress for incipient sediment motion dependent on channel-bed slope?" In: *Journal Of Geophysical Research-Earth Surface* 113.F2, F02008.

Lamb, Michael P et al. (2011). "A model for fire-induced sediment yield by dry ravel in steep landscapes." In: *Journal of Geophysical Research* 116.F3, F03006.

Leprince, S et al. (2007). "Automatic and precise orthorectification, coregistration, and subpixel correlation of satellite images, application to ground deformation measurements." In: *Geoscience and Remote Sensing, IEEE Transactions on* 45.6, pp. 1529–1558.

Miller, Robert L and Robert J Byrne (1966). "The angle of repose for a single grain on a fixed rough bed." In: *Sedimentology* 6.4, pp. 303–314.

Montgomery, DR and JM Buffington (1997). "Channel-reach morphology in mountain drainage basins." In: *Geological Society of America Bulletin* 109.5, pp. 596–611.

Mueller, E R, J Pitlick, and J M Nelson (2005). "Variation in the reference Shields stress for bed load transport in gravel-bed streams and rivers." In: *Water Resources Research* 41.4, W04006.

Parker, G, P R Wilcock, and C Paola (2007). "Physical basis for quasi-universal relations describing bankfull hydraulic geometry of single-thread gravel bed rivers." In: *Journal of Geophysical Research* 112.F04005.

Parker, Gary, Peter C Klingeman, and David G McLean (1982). "Bedload and size distribution in paved gravel-bed streams." In: *Journal of the Hydraulics Division* 108.4, pp. 544–571.

Recking, A (2009). "Theoretical development on the effects of changing flow hydraulics on incipient bed load motion." In: *Water Resources Research* 45, W04401.

Rickenmann, D (1997). "Sediment transport in Swiss torrents." In: *Earth Surface Processes and Landforms* 22, pp. 937–951.

Scheingross, Joel S et al. (2013). "Influence of bed patchiness, slope, grain hiding, and form drag on gravel mobilization in very steep streams." In: *Journal Of Geophysical Research-Earth Surface* 118, pp. 1–20.

Selby, Michael John (1993). *Hillslope Materials and Processes*. Oxford University Press on Demand.

Shields, A (1936). "Anwendung der Ähnlichkeitsmechanik und der Turbulenzforschung auf die Geschiebebewegung." In: *Mitt. Preuss Versuchsanst. Wasserbau Schiffbau* 26.

Stock, J and W E Dietrich (2003). "Valley incision by debris flows: Evidence of a topographic signature." In: *Water Resources Research* 39.4, p. 1089.

Takahashi, T (1978). "Mechanical Characteristics of Debris Flow." In: *J Hydr Eng Div-ASCE* 104.HY8, pp. 1153–1169.

Tognacca, Christian, Gian Reto Bezzola, and H E Minor (2000). "Threshold criterion for debris-flow initiation due to channel-bed failure." In: *Debris-Flow Hazards Mitigation: Mechanics, Prediction, and Assessment*. Ed. by G F Wieczorek and N D Naeser. Balkema, Rotterdam, pp. 89–97.

Wiberg, Patricia L and Jim Dungan Smith (1987). "Calculations of the Critical Shear Stress for Motion of Uniform and Heterogeneous Sediments." In: *Water Resources Research* 23.8, pp. 1471–1480.

Yager, E M, J W Kirchner, and W E Dietrich (2007). "Calculating bed load transport in steep boulder bed channels." In: *Water Resources Research* 43.7, W07418.

Zimmermann, A and M Church (2001). "Channel morphology, gradient profiles and bed stresses during flood in a step-pool channel." In: *Geomorphology* 40, pp. 311–327.

Zimmermann, André, Michael Church, and Marwan A Hassan (2010). "Step-pool stability: Testing the jammed state hypothesis." In: *Journal Of Geophysical Research-Earth Surface* 115, F02008.

Chapter 2

Unraveling bed slope from relative roughness in initial sediment motion

This chapter was adapted from the peer-reviewed journal article:

Prancevic, J. P., and M. P. Lamb (2015), Unraveling bed slope from relative roughness in initial sediment motion, *J. Geophys. Res.*, 120 (3), 474–489, doi: 10.1002/2014JF003323

Abstract

Understanding incipient sediment transport is crucial for predicting landscape evolution, mitigating flood hazards, and restoring riverine habitats. Observations show that the critical Shields stress increases with increasing channel bed slope, and proposed explanations for this counterintuitive finding include enhanced form drag from bed forms, particle interlocking across the channel width, and large bed sediment relative to flow depth (relative roughness). Here we use scaled flume experiments with variable chan-

nel widths, bed slopes, and particle densities to separate these effects which otherwise covary in natural streams. The critical Shields stress increased with bed slope for both natural gravel ($\rho_s = 2.65$ g/cm^3) and acrylic particles ($\rho_s = 1.15$ g/cm^3), and adjusting channel width had no significant effect. However, the lighter acrylic particles required a threefold higher critical Shields stress for mobilization relative to the natural gravel at a fixed slope, which is unexpected because particle density is accounted for directly in the definition of Shields stress. A comparison with model predictions indicates that changes in local velocity and turbulence associated with increasing relative roughness for lighter materials are responsible for increasing the critical Shields stress in our experiments. These changes lead to concurrent changes in the hydraulic resistance and a nearly constant critical stream power value at initial motion. Increased relative roughness can explain much of the observed heightened critical Shields stresses and reduced sediment transport rates in steep channels and also may bias paleohydraulic reconstructions in environments with exotic submerged densities such as iron ore, pumice, or ice clasts on Titan.

2.1 Introduction

Predicting sediment transport in steep, shallow flows is of fundamental importance to several problems within Earth and planetary sciences: mitigating hazards from debris-laden floods (e.g., Prancevic et al., 2014), landscape evolution (e.g., Howard, 1994; Tucker et al., 1997), and Earth and planetary paleoflood reconstructions (e.g., Costa, 1983; Perron et al., 2006). For example, landscape evolution is driven by river incision, which

in turn is sensitive to the onset of sediment motion (e.g., Howard, 1994; Tucker et al., 1997). Studies show that normalized channel steepness in natural catchments is consistent with observed erosion rates only when thresholds for sediment motion are applied (e.g., Lague, 2003; Dibiase et al., 2011). Initial sediment motion is usually cast in terms of the bed stress normalized by grain weight per unit bed area, or Shields stress:

$$\tau^* = \frac{\tau_b}{(\rho_s - \rho)gD} \tag{2.1}$$

where τ_b is the spatially and temporally averaged basal shear stress, g is gravitational acceleration, D is the median grain diameter, ρ_s is sediment density, and ρ is fluid density. The Shields stress at initial sediment motion, or critical Shields stress (τ_c^*), is sediment-size dependent but has been shown to equal a constant value between about 0.03 and 0.06 for high particle Reynolds numbers ($Re_p > 10^2$) typical of gravel and coarser sediment (e.g., Buffington et al., 1997). Theoretical models that balance fluid forces and the frictional stability of grains support this finding (e.g., Wiberg et al., 1987).

Surprisingly, field and flume studies with steeper bed slopes reveal that sediment of a given size requires higher Shields stresses for mobilization despite the increased magnitude of gravity acting on the grains in the downstream direction (Ashida et al., 1973; Bathurst et al., 1984; Mueller, E R et al., 2005; Gregoretti, 2008; Bunte et al., 2013; Scheingross et al., 2013; Prancevic et al., 2014). Several different mechanisms have been proposed to explain this counterintuitive observation, but few have been isolated because all tend to covary with channel slope in natural streams. For example, steep channels tend to have channel widths (W) that are narrow relative to sediment size (e.g., $W/D < 10$), and

this may cause high τ_c^* due to particle force chains that span the channel width (i.e., a jammed state (Zimmermann et al., 2010)) and due to increased momentum loss through wall drag (e.g., Buffington et al., 1999). Steep channels also often contain large bed forms and immobile boulders, which extract momentum from the flow, reduce the basal shear stress available to move sediment, and therefore might cause higher than expected values of τ_c^* (e.g., Zimmermann et al., 2001; Yager et al., 2007).

Field and flume studies also show that flows over steep (>0.5°) erodible beds approach a critical Froude number ($Fr = \frac{U}{\sqrt{gH}}$, where U is the time-averaged and spatially averaged flow velocity and H is flow depth) (e.g., Grant, 1997). Experiments measuring the drag on an individual hemisphere in shallow flow show that supercritical Froude numbers induce up to an order-of-magnitude decrease in the drag coefficient relative to subcritical cases (Flammer et al., 1970). This effect could increase τ_c^* in steep channels. However, supercritical flows are rare in natural alluvial channels because of a coincident increase in frictional resistance with increasing slope. Observations of mean flow velocity indicate that the friction factor

$$C_f = \left(\frac{u^*}{U}\right)^2 \tag{2.2}$$

where $u^* = \left(\frac{\tau_b}{\rho}\right)^{1/2}$ is the shear velocity, increases sharply in steep, shallow flows (e.g., Rickenmann et al., 2011). In other studies researchers have observed that high relative roughness (i.e., D/H), typical of steep channels, causes changes in velocity profiles (e.g., Bayazit, 1976; Nikora et al., 2001) and near-bed turbulence intensity (Bayazit, 1976; Carollo et al., 2005), both of which may lead to heightened τ_c^* (Shields, 1936; Aksoy, 1973;

Bettess, 1984; Vollmer et al., 2007; Lamb et al., 2008; Recking, 2009) and heightened C_f. As an alternative to critical Shields stress, several researchers have advocated the use of unit stream power ($\omega = \tau_b U$) to predict sediment transport (Bagnold, 1980; Ferguson, 2005; Parker et al., 2011; Ferguson, 2012). Stream power is a particularly convenient parameter for landscape-scale studies of erosion (e.g., Howard, 1994; Whipple et al., 1999), where flow discharge is more easily approximated than flow depth by virtue of the scaling between discharge and drainage area (e.g., Hack, 1957). Ferguson (2005) proposed that the critical unit stream power needed to initiate sediment transport should be lower in steep channels due to the increased component of gravity in the downstream direction. A subsequent analysis of field and flume data (Parker et al., 2011) instead indicates that the nondimensional critical stream power,

$$\omega_c^* = \frac{\omega_c}{g(\rho_s - \rho)\sqrt{RgD^3}} \tag{2.3}$$

is a constant of $\omega_c^* = 0.1$, independent of bed slope. A revised theoretical model by Ferguson (2012) included a slope-dependent critical Shields stress and arrived at a similar prediction for critical unit stream power, $\omega_c^* \sim 0.1$, for bed slope angles smaller than $\sim 5°$. These findings indicate that changes in the critical Shields stress and flow resistance are interrelated as both depend on relative roughness, although a mechanistic rationale for this has not been established.

In a series of recent theoretical models, relative roughness has emerged as the leading hypothesis behind the heightened τ_c^* with increasing channel slope (Lamb et al., 2008; Recking, 2009; Ferguson, 2012). However, testing this theory is challenging because

channel slope, channel width, bed forms, Froude number, and relative roughness covary in natural channels. Although flume experiments offer an opportunity to separate their effects on initial sediment motion, few experimental studies have been conducted on incipient motion at very steep bed slopes (>5°) (Bayazit, 1976; Fernandez Luque et al., 1976; Chiew et al., 1994; Gregoretti, 2008; Prancevic et al., 2014). Of these studies, most confirm that steeper channel beds lead to heightened critical Shields stresses. However, no studies in steep channels separate the naturally covarying factors of relative roughness and channel slope (Ashida et al., 1973; Bathurst et al., 1984; Bettess, 1984; Shvidchenko et al., 2000; Prancevic et al., 2014). Therefore, results from these studies cannot be used to test for the effect of relative roughness on τ_c^* independent of channel slope and Froude number. In contrast, initial motion experiments conducted in sealed ducts, which contain no free surface and therefore no change in relative roughness or Froude number effects, show that τ_c^* decreases with increasing bed slope (Fernandez Luque et al., 1976; Chiew et al., 1994), consistent with classic theory (Wiberg et al., 1987), and opposite to observations in natural channels. These duct experiments suggest that heightened critical Shields stress cannot be explained in the absence of a water free surface. Open-channel flow experiments have yet to be conducted, however, to test whether heightened critical Shields stress can be explained by high relative roughness in the absence of steep channel slopes, particle interlocking, and bed form-induced form drag. This is our goal.

2.2 Experimental Design and Rationale

The experiments were designed as tests of recent theoretical models for initial sediment motion by isolating the effect of relative roughness from channel slope, Froude number, form drag due to bed forms, and particle jamming and interlocking across the channel width (Table 2.1). Of these factors, the most difficult to separate are channel slope and relative roughness. This can be illustrated by rewriting equation (2.1) for initial sediment motion in steady and uniform open-channel flow as

$$\tau_c^* = \frac{H \sin\theta}{RD} \tag{2.4}$$

where $R = \frac{\rho_s - \rho}{\rho}$ is the relative submerged density and θ is the inclination angle of the channel bed and water surface. Inspection of equation (2.4) shows that τ_c^* is the product of three dimensionless variables (H/D,$1/R$, and $\sin\theta$), and these must covary if τ_c^* is to remain constant over a wide range of channel conditions. In typical natural and experimental conditions, R is constant and relative roughness (D/H) therefore must covary with channel slope (θ) at initial motion if τ_c^* is constant. However, if τ_c^* varies with either θ or D/H, there will be an apparent dependence on both variables. It is clear from equation (2.4) that the only way to isolate the effects of relative roughness from channel slope in open-channel flow is by changing the submerged specific density of sediment (R). Changing the material density of the sediment results only in a change in the buoyant weight of the grain (e.g., Archimedes, 1897), which is already accounted for in the definition of τ_c^* . Indeed, previous studies have shown that at low slopes and small relative roughness, large changes in the relative submerged density (R = 0.06 to 6.9)

have a negligible effect on the critical Shields stress (e.g., Shields, 1936; White, 1940). However, in the steep, shallow flow regime, changing R at constant θ results in covarying changes in D/H, which may affect τ_c^* . Thus, submerged specific density is the key to testing the effect of relative roughness on τ_c^* independent of channel bed slope.

2.2.1 Experimental Setup

Here we build on the experiments of Prancevic et al. (2014), which measured the critical Shields stress of natural well-sorted, semiangular gravel ($D = 1.5$ cm; $\rho_s = 2.65$ g/cm^3; $R = 1.65$) over a wide range in channel slopes from $\theta = 1.8°$ to slopes steeper than the transition to mobilization by mass failure ($\theta > 22.3°$). To isolate relative roughness from channel slope, we conducted a series of complementary experiments using well-sorted, semiangular acrylic particles ($D = 2.3$ cm, $\rho_s = 1.15$ g/cm^3, $R = 0.15$). The acrylic particles were manufactured as spheres, and an initial set of experiments showed that initial sediment motion for perfect spheres was phenomenologically different from that of natural gravel (e.g., where sheets of particles translated together along planes of symmetry). To break the symmetrical packing, we heated and deformed the acrylic particles to create random, semiangular shapes similar to the natural gravel used in the experiments (Fig. 2.1). Owing to their lower submerged density, the acrylic particles require substantially less basal shear stress (τ_b) to move in comparison to gravel. Thus, for a given channel slope, the acrylic particles move under much larger relative roughness than the gravel, allowing us to isolate the effect of relative roughness (smaller flow depth) on initial motion from channel slope by comparing the gravel and acrylic results. The

particles are sufficiently large that the initial motion was particle Reynolds number (Re_p) and sediment size independent (Shields, 1936) (i.e., $Re_p > 10^3$, Table 2.1).

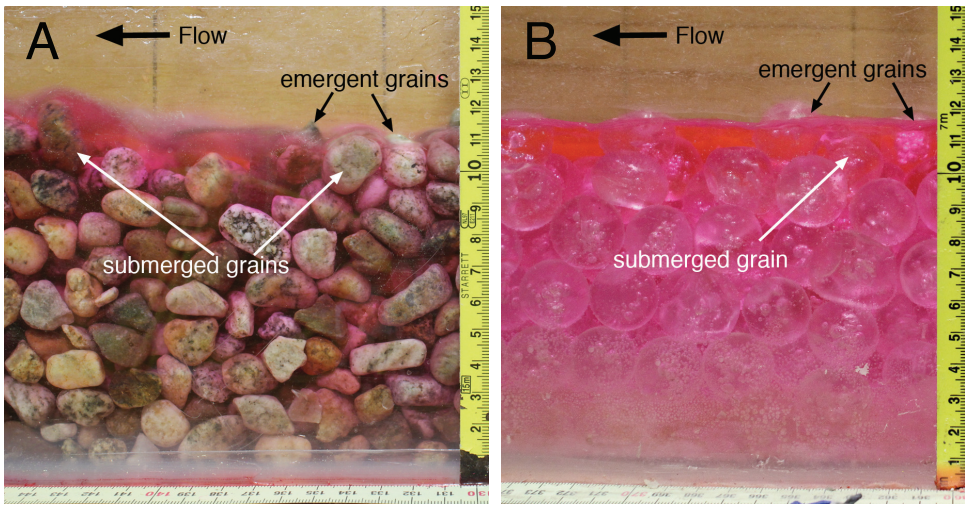

Figure 2.1: Photographs taken during (a) a gravel experiment at $\theta = 22.3°$ and (b) an acrylic experiment at $\theta = 2.6°$, showing some emergent grains, and others that remain submerged despite extending above the average water surface height.

We attempted to eliminate particle jamming in our experiments by using smooth walls and wide channels relative to the grain diameter (e.g., Zimmermann et al., 2010). To test whether particle jamming was occurring, experiments were conducted using two different channels widths for each material ($W/D = 23$ and 9 for gravel (Prancevic et al., 2014); $W/D = 6$ and 4 for acrylic). We also performed an additional set of experiments with gravel using rough walls (with gravel glued to the walls) to further test for any jamming effects (Table 2.1). To remove the stabilizing effect of bed forms (including morphologic form drag) on initial motion, all of our experiments started with a flat, hand-screed bed. Although initial water working can change initial motion criteria (e.g., Kirchner et al., 1990), we found that step-pools and alternate bars formed rapidly in our experiments, and the only means to eliminate bed forms as variables was to start from a planar, unworked bed. In addition, we ceased the experiments when sediment transport

significantly altered the bed from its initial state by building bed forms that were two grain diameters in relief or more.

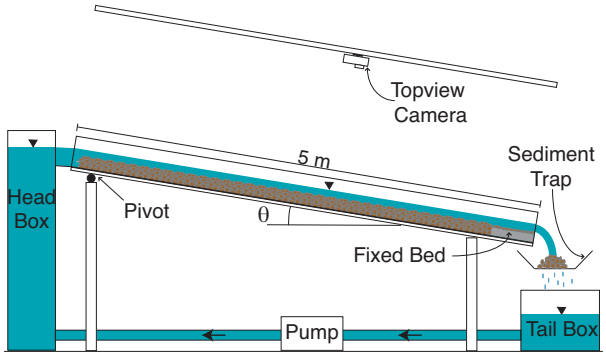

Figure 2.2: Flume schematic showing the general experimental setup. Not to scale.

We conducted 28 new experiments over a broad range of bed slopes ($\theta = 0.7°$ to 8.0°) in a 5 m long tilting flume (Fig. 2.2), the same as that used in Prancevic et al. (2014). All experiments began with a planar loose bed, ∼10.5 cm thick. The sediment bed was primarily composed of loose gravel. However, there was a single layer of fixed gravel at the base of loose material to prevent basal sliding of the entire bed. Also, the downstream-most section of the flume was protected from erosion due to water surface drawdown at the flume outlet using a 40 cm long fixed bed, also ∼10.5 cm in thickness.

2.2.2 Measuring the Critical Shields Stress

We incrementally increased the water discharge, pausing for 3 to 12 min at each discharge for flow measurements and observations of sediment transport. Because our target was initial motion, no sediment was fed into the flume. We calculated the critical Shields stress using equation (2.4) and by making a low-slope approximation ($\sin\theta \approx \tan\theta$) to be consistent with previous work. Owing to the rough water surface in steep and

shallow flows (Fig. 2.1), point measurements of flow depth were difficult to collect and yielded considerable scatter. Instead, flow depth was calculated using conservation of mass ($H = q_{surf}/U$) and measurements of surface flow discharge per unit width (q_{surf}) and width- and depth-averaged flow velocity (U). The total discharge was measured using an inline flow meter, and surface flow discharge was determined by subtracting the saturated subsurface discharge (Fig. 2.3). We defined the saturated subsurface discharge as that required to fully saturate the average thickness of the bed. To calculate these values, we mapped the air-water interface at a subsaturated level between 7 and 9 cm and extrapolated the discharge (measured using a flow meter) linearly to the full bed thickness (10.5 cm). These measured values were averaged for each slope. Due to high subsurface Reynolds numbers ($250 < Re_s = \frac{u_{sub}D}{\nu} < 700$, where u_{sub} (m/s) is the subsurface flow velocity and ν (m^2/s) is the kinematic viscosity), our observed specific discharges followed a Forchheimer curve rather than Darcy's law for natural gravel and acrylic, respectively:

$$\tan\theta = 3.59 q_{sub} + 78.1 q_{sub}^2 \tag{2.5}$$

and

$$\tan\theta = 0.899 q_{sub} + 69.1 q_{sub}^2. \tag{2.6}$$

where q_{sub} (m^2/s) is the depth-integrated specific discharge through the sediment bed (Forchheimer, 1901) (Fig. 2.3). Equations (2.5) and (2.6) were used for the calculation of saturation discharge at all slopes. We measured surface flow velocity by introducing a red dye pulse at the flume inlet and tracking the dye front over a 2.6 m section of the

flume using overhead videos recorded from a camera-oriented orthogonal to the water surface at 30 frames per second. We tracked the dye front rather than the dye peak because significant hyporheic exchange slowed the velocity of the dye peak relative to the mean flow velocity. Velocity is assumed to be constant across the channel width, which is true for the initial planar bed. If bed topography develops and the flow becomes confined, this method overpredicts flow velocity and underpredicts flow depth. Accordingly, data collected during the final discharges of some experiments were not used due to the presence of flow confinement.

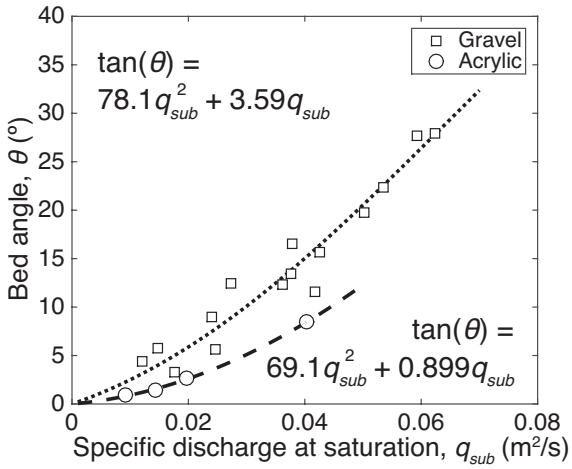

Figure 2.3: Bed angle as a function of measured specific discharge of subsurface flow. The best fit second-degree polynomial to measured discharges for the natural gravel (dashed line) and acrylic (dotted line) are those used in calculating the saturated subsurface discharge for all slopes (equations shown in the upper left and lower right corners, respectively).

In calculating flow depth using conservation of mass there are several potential sources of error. These include error in the partitioning of surface and subsurface discharge, error in the measurement of total discharge, and error in the velocity measurement. A maximum error associated with approximating the mean flow velocity by measuring the velocity of the dye front was assessed by comparing measured velocities of the dye front

and dye peak, which were typically within 10% of each other. Through repeated calibration of the flowmeter throughout the experiments, errors in the measurement of total discharge were found to typically be less than 3%. Errors in calculating the subsurface discharge were conducted by comparing the depths calculated using conservation of mass to depths measured by mapping the bed surface and water surface in side-view photographs for select experiments (e.g., Fig. 2.1). A direct comparison between flow depths measured using both methods for five bed angles between $\theta = 5.6°$ and 19.6° indicates that the errors in flow depth are typically less than 30%. Consequently, a maximum measurement error of 30% for flow depth, H, is assumed in our presentation of the experimental results (section 3).

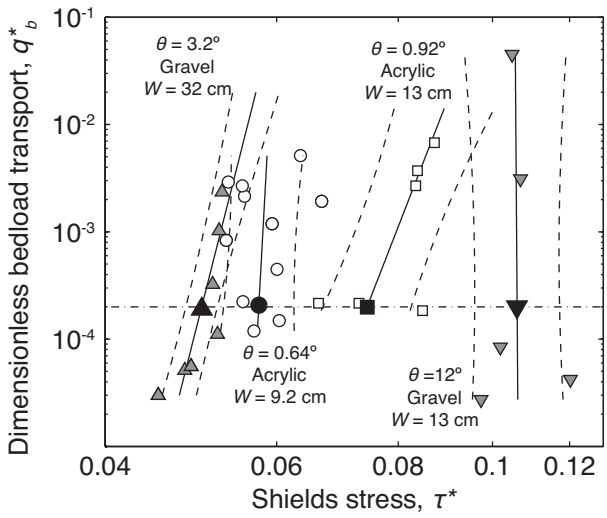

Figure 2.4: Dimensionless bed load transport as a function of Shields stress for several example experiments with different slopes. Data for both the acrylic (circle and square) and natural (shaded triangle and inverted triangle) gravel experiments are shown. Solid lines are power law fits, and subparallel dotted lines represent 50% confidence limits. Critical Shields stress for each slope is defined at a standard reference dimensionless sediment flux, $q^*_b = 0.0002$ (horizontal dashed line) (Parker et al., 1982).

We measured sediment flux for 1 to 10 min at each flow discharge using a sediment trap at the end of the flume (Fig. 2.2). For most experiments we found the critical

Shields stress by interpolating the bed load measurements to a reference nondimensional transport rate of $q_b^* = \frac{q_b}{\sqrt{RgDD}} = 2 \times 10^{-4}$, where q_b is the bed load transport rate per unit channel width (e.g., Parker et al., 1982) (Fig. 2.4). The only exception was the steepest case tested for both the natural gravel and acrylic (22.3° and 2.6°, respectively), which exhibited bed failure in addition to low rates of fluvial transport (e.g., Prancevic et al., 2014). While fluvial transport was observed in these experiments, subsequent failure of the bed prevented the construction of a power law correlation between bed load transport rate and Shields stress (e.g., Fig. 2.4). In these experiments, the flow conditions at the time of bed failure were taken as critical.

2.2.3 Model Comparison

We compared the results with existing models for initial motion of bed sediment (Wiberg et al., 1987; Lamb et al., 2008; Recking, 2009; Parker et al., 2011; Ferguson, 2012), which required inputs of grain pocket friction angles, ϕ. ϕ was measured for both the natural gravel (ϕ_g) and acrylic particles (ϕ_a) using tilt table experiments in which a single grain was placed on a planar bed of the same material glued to a board and tilted until the grain dislodged (e.g., Miller et al., 1966). The mean and standard deviation of these angles were $\phi_g = 58.8° \pm 13.7°$ (n=296) and ϕ_a =$40.8° \pm 7.1°$ (n = 100).

The Wiberg et al. (1987) model balances driving and resisting forces acting on individual grains to calculate the threshold stress required for motion. However, it was designed for application to relatively deep, low-sloping rivers and includes no components to account for hydraulic changes in steep, shallow flows. The Lamb et al. (2008)

model builds on that of Wiberg by including components that account for particle emergence from the flow (reducing buoyancy and the cross-sectional area experiencing drag force), reduced turbulence intensity, and a quadratic (instead of logarithmic) velocity profile within the grain layer. The Recking (2009) and Ferguson (2012) models instead rely on observations of C_f, and its dependence on relative roughness to predict sediment motion. The Recking model uses flow resistance data to predict an average flow velocity around a sediment grain and also considers the effects of particle emergence. The Ferguson model theorizes that excess flow resistance in shallow flows dissipates the stress available for sediment transport, requiring larger flow depths for incipient motion. We also assess the viability of a constant critical stream power for predicting the onset of sediment transport (e.g., Ferguson, 2005; Parker et al., 2011). Comparing each of these models with our experimental observations allows us to assess their applicability and the validity of the underlying mechanisms.

2.3 Results

2.3.1 Shields Stress

Scatter exists in the bed load transport curves (Fig. 2.4) due to both the stochasticity of sediment transport rates and the sources of measurement error discussed in Section (2.2.2). For most of our experiments the sediment flux increased nonlinearly with increased Shields stress, and a fairly wide range of bed load transport rates was observed for a narrow range in Shields stresses (Fig. 2.4). The measured Shields stresses in our

experiments varied more so with channel slope than they did with bed load flux at a given slope (Fig. 2.4), and results show a trend of increasing critical Shields stress with increasing bed slope (Fig. 2.5). The error bars in Figures (2.5) to (2.9) reflect either the 50% confidence intervals of the best fit bed load curves displayed in Fig. 2.4 or the 30% uncertainty in the depth measurements (Section 2.2.2), whichever is larger.

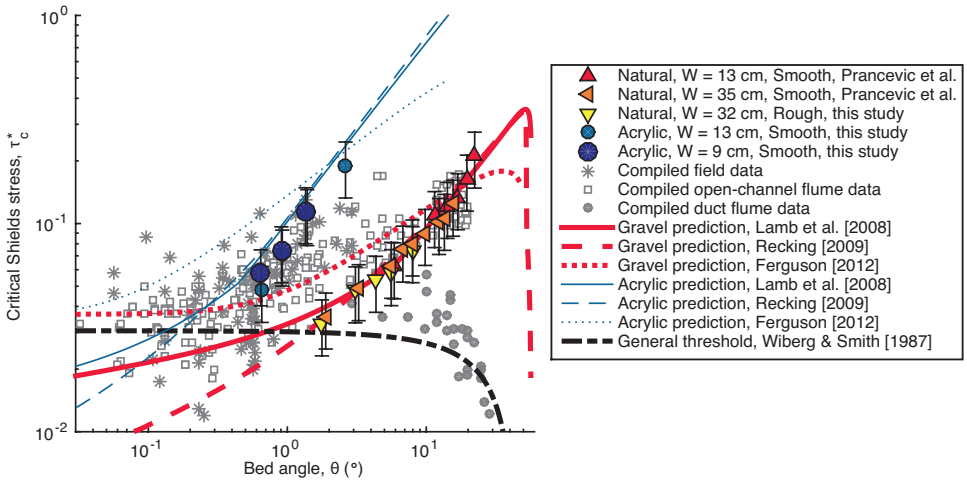

Figure 2.5: The critical Shields stress as a function of bed angle for all experimental results (solid symbols), model predictions (dotted, dashed, and solid lines), and data compilation (grey asterisks are field observations from the Buffington compilation with $Re_p > 102$ (Buffington et al., 1997) and subsequent studies (Mueller, E R et al., 2005), open squares are open channel flume measurements from the Buffington compilation with $Re_p > 102$ (Buffington et al., 1997) and subsequent studies (Shvidchenko et al., 2000; Gregoretti, 2008), and grey circles are sealed duct flume measurements (Fernandez Luque et al., 1976; Chiew et al., 1994; Dey et al., 2000). "Rough" refers to those experiments that had a fixed layer of gravel on each wall. All other experiments had walls of smooth acrylic and epoxy-covered wood. The error bars represent 30% measurement error or confidence limits calculated from bed load curves (e.g., Fig. 2.4). The model of Wiberg et al. (1987) makes the same prediction for acrylic and gravel.

Table 2.1: Experimental conditions and results

Particle Material	Particle Relative Submerged Density, R	Median Particle Diameter, D (cm)	Flume Width, W (cm)	W/D	Wall Texture	Bed Slope Angle, $\theta(^\circ)$	Critical Shields Stress, τ_c^*	Critical Unit Discharge, q_{surf} (m^2/s)	Relative Roughness D/H	Particle Reynolds Number at the Onset of Motion[a], Re_p	Froude Number at the Onset of Motion, Fr_c	Friction Factor, C_f
Data from **C**hapter 3												
Gravel	1.65	1.5	35	23	Smooth	1.9	0.036	0.019	0.56	1400	1.38	0.018
						3.3	0.049	0.0173	0.71	1600	1.82	0.018
						5.6	0.063	0.0098	0.94	1900	1.57	0.04
						6.8	0.075	0.0079	0.96	2000	1.31	0.07
						8	0.08	0.0062	1.06	2100	1.19	0.1
						9.8	0.09	0.0056	1.16	2200	1.23	0.114
						12.4	0.1	0.004	1.33	2300	1.08	0.188
						13.5	0.11	0.0036	1.32	2500	0.96	0.263
						15.6	0.12	0.0028	1.41	2600	0.82	0.413
Gravel	1.65	1.5	13	8.7	Smooth	5.9	0.062	0.0057	1.01	1800	1.01	0.101
						11.5	0.11	0.0039	1.12	2500	0.81	0.313
						14.2	0.12	0.0037	1.28	2600	0.94	0.288
						16.9	0.13	0.0021	1.42	2700	0.61	0.813
						19.6	0.16	0.0022	1.35	3000	0.6	1
						22.3[b]	0.21	0.0032	1.18	3400	0.71	0.813
New data												
Gravel	1.65	1.5	32	21	Rough	1.8	0.033	0.0182	0.58	1300	1.39	0.016
						3.1	0.048	0.0167	0.68	1600	1.65	0.02
						4.3	0.054	0.0126	0.84	1700	1.69	0.026
						5.6	0.058	0.0093	1.02	1800	1.67	0.035
						8	0.074	0.0065	1.15	2000	1.4	0.071
Acrylic	0.15	2.3	9	3.9	Smooth	0.7	0.058	0.0055	1.4	1000	0.84	0.018
						0.9	0.074	0.0057	1.42	1200	0.89	0.02
						1.4	0.11	0.0031	1.48	1400	0.51	0.093
Acrylic	0.15	2.3	13	5.7	Smooth	0.7	0.048	0.0047	1.7	900	0.94	0.014
						0.9	0.072	0.0031	1.45	1100	0.49	0.065
						1.4	0.11	0.0024	1.48	1400	0.4	0.15
						2.6[b]	0.19	0.0022	1.59	1800	0.41	0.275

[a] The particle Reynolds number is defined as $Re_p = (\tau^* RgD)^{1/2} D/\nu$, where ν is the kinematic viscosity.

[b] At the steepest slope tested for each material bed failure was observed, in addition to fluvial transport.

Results from the smooth-walled gravel experiments show that τ_c^* increases dramatically from 0.036 at $\theta = 1.9°$ to a maximum value of $\tau_c^* = 0.21$ at $\theta = 22.3°$. Results are similar for the gravel experiments for both channel widths, and for the experiments with rough walls, suggesting that we successfully eliminated effects from particle jamming on initial motion within error (Fig. 2.5). Results of the acrylic experiments are strikingly different from those of the gravel experiments. For example, at the same bed slope of about 2°, τ_c^* for the acrylic data are approximately a factor of 3 larger than for the gravel (Fig. 2.5). Like the gravel experiments, changing channel width had no effect on initial sediment motion in the acrylic experiments, such that enhanced particle jamming cannot explain the offset between the gravel and acrylic data sets. Furthermore, at low slopes the acrylic experiments had subcritical Froude numbers, whereas the gravel had supercritical Froude numbers (Fig. 2.6a), which is opposite to the expected trend if the heightened critical Shields stresses for the acrylic were due to $Fr > 1$. Instead, the observed difference in Froude number is likely a secondary effect of increased frictional resistance as flow depth shallows relative to grain size (Fig. 2.6b), causing anomalously slow velocities in the shallow and low-sloping acrylic experiments. This increased frictional resistance is expected for flows with increasing D/H (e.g., Bathurst, 1985; Grant, 1997).

The effect of relative roughness (independent of channel slope) may be further evaluated by recasting τ_c^* as a function of D/H using equation (2.4). The natural gravel and the acrylic particles exhibit substantially different particle friction angles ($\phi_g = 58.8°$ and $\phi_a = 40.8°$). Moreover, the steeper bed angles at which the gravel experiments were conducted increase the downstream component of gravity acting on the grains, relative to the acrylic experiments. In order to remove the gravitational and particle friction effects,

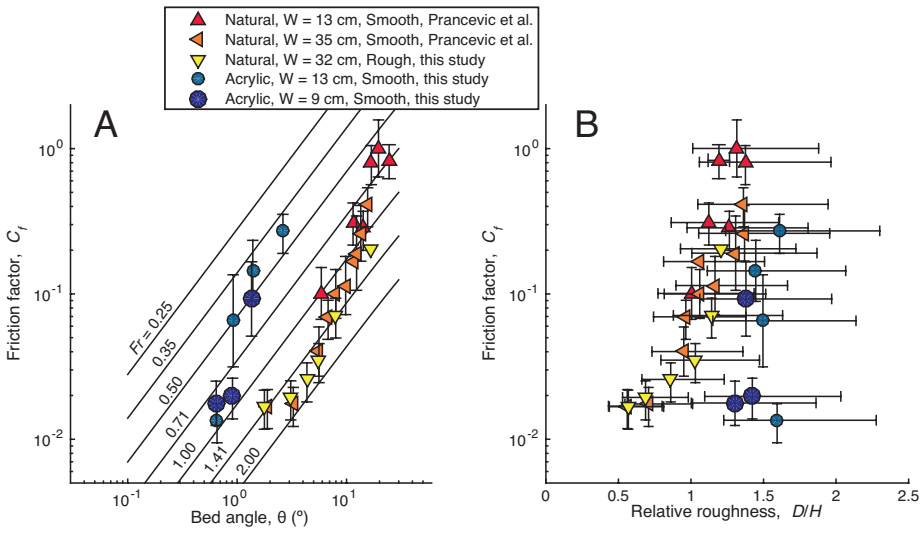

Figure 2.6: (a) Friction factor at the onset of motion as a function of bed slope for all experimental results. The parallel solid black lines are constant Froude numbers calculated by assuming steady, uniform flow and substituting $u^* = \sqrt{gH \sin\theta}$ and $U = Fr\sqrt{gH}$ into equation (2.2). (b) Friction factor as a function of relative roughness for all experimental data. The error bars indicate ±30% measurement error or bed load confidence limits (e.g., Fig. 2.4).

all data were normalized by the friction angle and bed angle term in the force balance models: $\frac{\tan\phi - \tan\theta}{1+F_L/F_D \tan\phi}$, where $F_L/F_D = 0.85$ is the assumed ratio of lift and drag forces acting on the grains (e.g., Wiberg et al., 1987; Lamb et al., 2008; Recking, 2009) (Fig. 2.7). In this space the gravel and acrylic data sets nearly collapse to the same trend. Results for the gravel show increasing τ_c^* with increasing relative roughness, with a significant increase in the slope of this trend for $D > H$ corresponding to either where particles are partially emergent from the flow or where water cascades over the particle tops (Fig. 2.1). The data trend is similar to that shown in a compilation by Bettess (1984) using gravel of uniform density, but they investigated only $D/H < 1$. For a given value of relative roughness (e.g., D/H=1.4),the acrylic data appear to have slightly smaller τ_c^* values than the gravel. These differences must be due to factors besides relative roughness that may include altered hydraulics at different slopes. For example, for $D/H =$

1.4 the gravel experiments were at much steeper bed slopes ($14° < \theta < 16°$) than the acrylic ($0.92° < \theta < 1.3°$), resulting in increased flow spilling over grains. Despite these major differences in slope, the near collapse of the acrylic and gravel data in Fig. 2.7, as compared with Fig. 2.5, shows that relative roughness was the key parameter controlling initial sediment motion in our experiments, not bed slope.

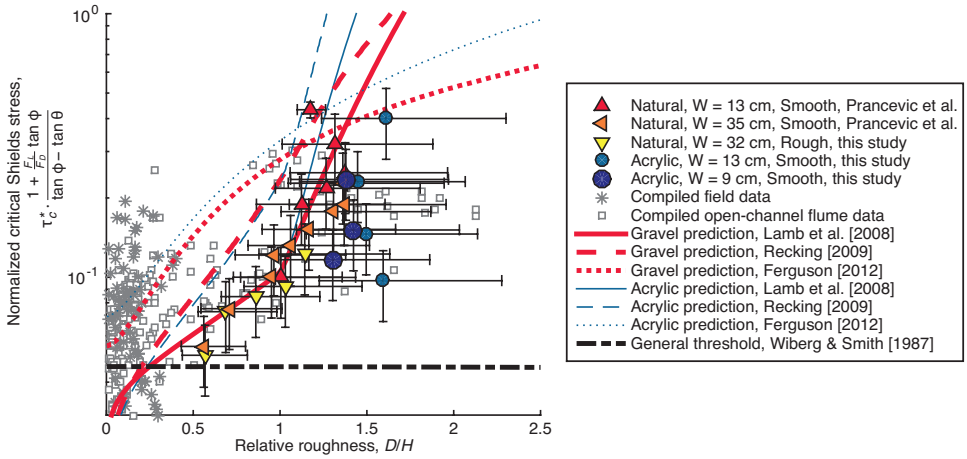

Figure 2.7: The critical Shields stress as a function of relative roughness for the same data shown in Figure 5. The sealed duct data are not included because relative roughness is not meaningful without a free surface. Note the similar trend and distribution of data to C_f versus D/H (Figure 6b). The error bars represent 30% measurement error or bed load confidence limits (e.g., Fig. 2.4).

The experimental data are in general agreement with the model predictions of Lamb et al. (2008) and Recking (2009) for the natural gravel and acrylic particles (Figures 2.5 and 2.7), although τ_c^* for the acrylic particles is overpredicted. The Ferguson (2012) model captures the general trends but overpredicts the Shields stress required to transport both materials. In contrast, the model of Wiberg et al. (1987), which does not include relative roughness as a factor, shows decreasing τ_c^* with increasing slope and is consistent only with sealed duct experiments where D/H does not vary with slope (Fig. 2.5).

2.3.2 Flow Resistance and Stream Power

In our experiments, flow resistance (C_f) at the onset of sediment motion exhibits a similar increase with D/H to the Shields stress (compare Fig. 2.6b to Fig. 2.7). The steep increase in flow resistance with relative roughness has been documented previously (Bathurst, 1985; Rickenmann et al., 2011; Ferguson, 2012), but the offset in flow resistance between acrylic and gravel data sets for a given relative roughness indicates that there may be an additional bed slope dependence, such as spilling around and over particles. Despite this potential slope effect, a strong power law relationship exists between Shields stress and flow resistance (Fig. 2.8a). Under the assumption of steady and uniform flow, and using equations (2.1)-(2.3), critical stream power can be rewritten as follows:

$$\omega_c^* = \left(\frac{\tau_c^*}{C_f^{1/3}} \right)^{3/2} \tag{2.7}$$

Equation (2.7) shows that if ω_c^* is constant, then critical Shields stress must be proportional to flow resistance to the one-third power, consistent with our observations (Fig. 2.8a). The acrylic experiments show higher values for critical stream power (Fig. 2.8b), but the data generally cluster around an average of $\omega_c^* = 0.11$ for the acrylic and $\omega_c^* = 0.085$ for the natural gravel, similar to the data compilation of Parker et al. (2011).

To compare these experimental observations to theoretical expectations of critical stream power, we employ equation (2.7) and predicted values of C_f and τ_c^* . Here we use the established flow resistance relationship of Bathurst (1985):

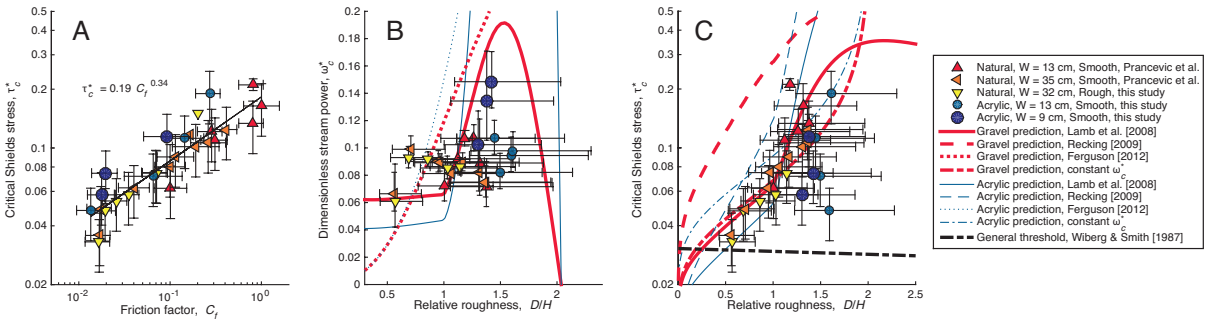

Figure 2.8: (a) Friction factor as a function of critical Shields stress for both materials and a best fit power law relating the two parameters. (b) Critical dimensionless unit stream power (equation (2.3)) as a function of relative roughness. The Lamb et al. (2008) Shields stress model has been recast to solve for the critical stream power using equations (2.7) and (2.8). (c) The critical Shields stress (uncorrected for slope and friction angle differences) as a function of relative roughness. The Lamb et al. (2008) and Recking (2009) models are shown, as well as the critical Shields stress predicted by a constant critical stream power and equations (2.7) and (2.8). The error bars represent ±30% measurement error or bed load confidence limits (e.g., Fig. 2.4).

$$C_f^{-1/2} = 5.62 \log\left(\frac{H}{D_{84}}\right) + 4 \tag{2.8}$$

and the critical Shields stress model of Lamb et al. (2008) to predict a critical stream power (Fig. 2.8b). For comparison, the model of Ferguson (2012) is also shown in Fig. 2.8b and uses the variable-power flow resistance equation of Ferguson (2007). The Lamb-Bathurst model for critical stream power predicts near-constant values for $D/H \leq 1$, similar to our experimental observations. For shallower flows ($D/H > 1$), the predicted stream power values increase sharply and diverge from observations. The Ferguson model predicts a steep relationship between ω_c^* and D/H for all values tested, diverging from most of our experimental data. The divergence of our experimental observations with these model predictions occurs because the predicted values of C_f and τ_c^* do not maintain the same one-third-power covariance as we observe in our experimental data.

In a similar inversion, we may recast a constant stream power value ($\omega_c^* = 0.085$

for the natural gravel and $\omega_c^* = 0.11$ for the acrylic) as a critical Shields stress using equations (2.7) and (2.8) (Fig. 2.8c). The Shields stresses predicted using this method are within error of measurements in the gravel experiments, with a slight underestimation for the very steep and shallow experiments ($D/H > 1$). Similar to the Lamb et al. (2008) model, the stream power inversion overestimates critical Shields stresses for the acrylic experiments, but to a lesser degree.

2.4 Discussion

2.4.1 The Effects of Flow Depth, Slope, Form Drag, and Jamming on Incipient Motion

The only variables that differ significantly between the gravel and the acrylic experiments at a given channel slope are submerged specific particle density (R) and relative roughness (D/H). The effect of submerged specific density on particle weight, however, is already accounted for in the definition of the critical Shields stress (equation (2.1)) (i.e., Archimedes, 1897), such that in the absence of relative roughness effects, the acrylic and gravel data sets should collapse to a similar trend. They do not. Therefore, the systematic offset of the acrylic data to higher τ_c^* at a given channel slope is due to the effect of increased relative roughness alone. This is the first conclusive evidence to show that increased relative roughness alone can cause heightened τ_c^* in the absence of steep channel slopes, form drag induced by bed forms, particle jamming or interlocking caused by narrow channel widths, relative grain size, or supercritical Froude numbers.

This notwithstanding, many of the compiled field data (Fig. 2.5) exhibit critical Shields stresses that are larger than our experimental results for a given channel slope. This discrepancy is likely due to other factors that were purposefully eliminated in our experiments, including particle jamming and interlocking and form drag from bed forms (Zimmermann et al., 2001; Yager et al., 2007; Zimmermann et al., 2010). In natural channels, relative roughness, bed forms, and particle jamming may be intertwined. For example, roughness due to bed forms is larger than that due to grains, and therefore bed forms may also induce larger τ_c^* through changes in relative roughness, in addition to changes in morphologic form drag.

Although we have shown that relative roughness has a profound impact on sediment mobility, the slight offset between the acrylic and gravel data in plots of Shields stress (Fig. 2.7), flow resistance (Fig. 2.6b), and stream power (Fig. 2.8b) versus D/H indicates that there may be an additional bed slope effect on these parameters that has not previously been recognized. Because C_f is a hydraulic parameter it does not depend on the material density of the grains, and a significant offset between the gravel and acrylic data should not exist. The slight offset that is present may suggest that the steeper slopes tested in the gravel experiments induced higher flow resistance. Alternatively, this offset may be due to differences in particle shape and texture (e.g., Fig. 2.1). Regardless of the cause in the offset of C_f between the two materials, the reduced flow velocities of the gravel experiments relative to the acrylic, for a given relative roughness, appear to have affected the conditions required for sediment transport. For example, the slight offset observed in τ_c^* versus D/H (Fig. 2.7) may be explained by slower local flow velocities and reduced turbulent intensity around the gravel relative to the acrylic. Conversely,

multiplying the critical shear stress by heightened flow velocities in the acrylic experiments boosts the stream power required for transport relative to the gravel in ω_c^* versus D/H (Fig. 2.8b).

2.4.2 Assessment of Models

2.4.2.1 Predicted Critical Shields Stress

Our results are consistent with models that consider the effects of relative roughness on flow hydraulics and near-bed turbulence (Lamb et al., 2008; Recking, 2009), and inconsistent with models that do not consider these effects (Wiberg et al., 1987). The Ferguson (2012) model overpredicts the critical Shields stress for most of our experimental conditions (Fig. 2.5). The Ferguson model is less mechanistic by design and performs considerably well due to the interrelated nature of flow resistance, Shields stress, and stream power. However, it lacks predictive power where the flow resistance is not known or data is scarce, such as for slopes greater than $\sim 10^\circ$ (e.g., Comiti et al., 2007). The models of Lamb et al. (2008) and Recking (2009) rely on flow resistance models as well but use them to calibrate physical mechanisms that are expected to change with slope and relative roughness, including the mean velocity profile and turbulence intensity. This mechanistic approach ultimately results in improved fits to our experimental data.

Using our experimental observations we can provide some assessment of the mechanisms employed by the models of Lamb et al. (2008) and Recking (2009). One mechanism that was violated in some cases was the expectation for particles to emerge from the flow when $D/H > 1$, which would increase the effective particle weight. Even in flows that

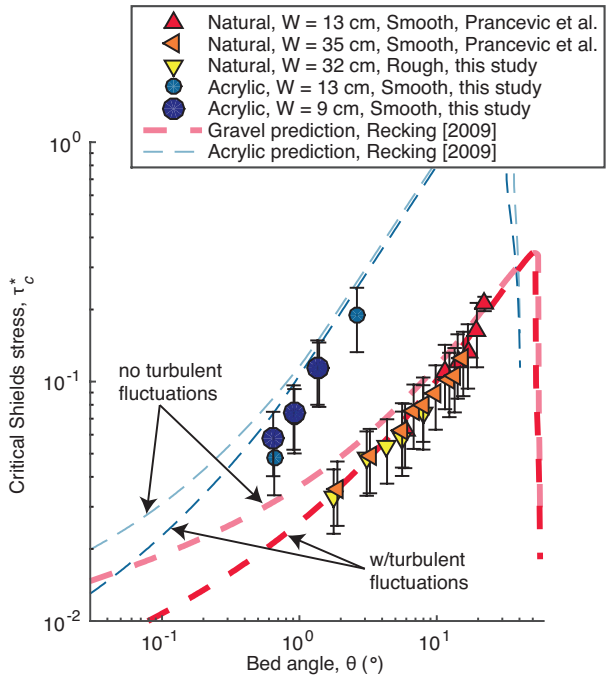

Figure 2.9: Critical Shields stress of experimental data and the Recking (2009) model versus bed angle. The original Recking model (light lines) for both materials does not include the effect of reduced turbulence intensity in shallow flows, but the modified version (bold lines) does. The error bars represent 50% confidence limits calculated from bed load curves.

were on average much shallower than the grain size, most particles remained submerged by flow traveling up and over the grain (Fig. 2.1). However, calculating buoyancy, lift, and drag forces within such cascading flow is not straightforward, as fine-scale velocity and pressure measurements in rough flows are not available. One way the Lamb et al. (2008) and Recking (2009) models differ is that the Lambmodel includes changing intensity of turbulence fluctuations with relative roughness, in addition to changes in mean flow velocity. Specifically, Lamb et al. (2008) propose that the transport- inducing drag force bearing on a grain, F_D, is not simply a function of local flow velocity (i.e., $F_D \propto u^2(z)$), but it has an additional dependence on the depth-averaged velocity:

$$F_D \propto \left\langle (u(z) + \alpha U)^2 \right\rangle \tag{2.9}$$

where $\alpha \approx 0.2$ is a constant relating U to the magnitude of turbulent fluctuations near the bed and the brackets indicate spatial averaging over the submerged height of the grain. As discussed in the next Section (2.4.2.2), the use of a depth-averaged flow velocity term is supported both by the fit of the Lamb model and reduced variability observed in our measured values of critical stream power. Indeed, adding the turbulent component to the Recking model improves its fit with our experimental observations as well (Fig. 2.9), suggesting that reduced turbulence intensity in shallow flows plays an important role in increasing the critical Shields stress for sediment transport.

2.4.2.2 Constant Critical Stream Power

A constant critical stream power predicts the onset of sediment motion within error for most experiments within a given experiment set. This collapse of the experimental data to a small range in critical stream power values indicates that multiplying the Shields stress by the respective depth-averaged flow velocity greatly reduces variability after normalizing for grain weight (e.g., equation (2.3)). This additional velocity term may be mechanistically justified. In the development of their Shields stress model, Lamb et al. (2008) propose that the magnitude of turbulent fluctuations scales with the depth-averaged flow velocity (equation (2.9)). The additional velocity term used to calculate the drag force does not yield an equation of the same form as stream power, but it does produce a critical Shields stress that depends on the depth-averaged flow velocity, providing some grain-scale justification for a constant critical stream power model.

However, offsets exist between the gravel and acrylic experiments and between the data sets compiled by Parker et al. (2011). This variability indicates that a single value of critical stream power cannot be universally applied. Moreover, the variability of critical stream power is not easily predicted because a grain-scale model that relates stream power directly to energy acting on grains has not been established. Instead, stream power models like the one presented in Section (2.3.2) rely on physically based predictions of critical shear stress that are subsequently multiplied by predicted mean flow velocities (e.g., Parker et al., 2011; Ferguson, 2012). As a result, critical stream power predictions to date account for changes in bed conditions (e.g., particle friction angle and relative grain size) only by utilizing models for critical shear stress.

2.4.3 Implications for Bed Load Transport Rates

Measured bed load transport rates in steep mountain channels are commonly an order of magnitude smaller than predicted by traditional bed load transport formulas developed for lower sloping rivers (e.g., Rickenmann, 2001; Mueller et al., 2008; Nitsche et al., 2011; Yager et al., 2012). These transport equations often have the general form:

$$q_b^* = a(\tau^* - \tau_c^*)^b \tag{2.10}$$

where a and b are empirical constants that vary from $a = 4.9$ to 8.0 and $b = 1.5$ to 1.6 (e.g., Meyer-Peter et al., 1948; Fernandez Luque et al., 1976; Wong et al., 2006). Equation (2.10) may be modified in several ways to provide a better prediction in steep channels: a and b may be adjusted to smaller values, τ_c^* may be increased, and τ^* may be replaced

with a reduced "effective" Shields stress that is available to transport sediment. The latter approach is most commonly favored and is typically conceptualized as momentum spent on morphologic form drag due to large immobile boulders, step-pools, or other bed forms (e.g., Rickenmann, 2001; Yager et al., 2007).

Our results indicate that τ_c^* increases with channel bed slope, which according to equation (2.10) should reduce bed load transport rates even in the absence of form drag from immobile obstacles or bed forms. In addition, the hydraulic mechanisms of reduced near-bed mean flow velocities and turbulent intensity in rivers with high relative roughness are not limited to the onset of sediment motion. These mechanisms should be important in reducing the expected bed load flux at all transport stages. Indeed, a recent study that evaluated sediment transport models at 13 steep mountain streams found that the best fit formulas use both an increased critical Shields stress (τ_c^*) and a reduced effective Shields stress available to transport sediment (τ^*) (Nitsche et al., 2011). Although Nitsche et al. attribute the decrease in effective Shields stress to morphologic form drag from bed forms, our results suggest that effective Shields stress can be lower than expected in steep mountain streams even with a planar bed because of changes in near-bed hydraulics associated with high relative roughness.

2.4.4 Sediment Density and Incipient Motion

In addition to the usefulness of changing density to isolate relative roughness from channel slope, our results have direct application to sediment transport of particles of different densities. These cases are relatively rare on Earth, but some prominent examples exist

elsewhere. For example, on Titan, liquid hydrocarbons (e.g., ethane and methane) are thought to transport clasts of water ice and solid organic particles, yielding a relative submerged density range of $R = 0.5$ to 2 (Perron et al., 2006; Lorenz et al., 2010; Grotzinger et al., 2013). On a relatively low bed angle of $\theta = 0.1°$, this density range yields a critical Shields stress range of $\tau_c^* = 0.021$ to 0.026 according to the Lamb et al. (2008) model. On a steeper slope of $\theta = 5°$, the range in predicted Shields stresses widens considerably to $\tau_c^* = 0.054$ to 0.14 due to the enhanced effects of large D/H for different particle densities. On Mars, the transportation of basalt-derived sediment by liquid water ($R = 1.65$ for plagioclase and $R = 1.9$ for intact basalt) should yield similar Shields stresses to those observed on Earth (e.g., Grotzinger et al., 2013). However, transport by high-density brines ($R = 1.04$) requires heightened Shields stresses for channels with the same bed slope (Tosca et al., 2011; Lamb et al., 2012). For example, on a steep slope of $\theta = 5°$, the increase in density from freshwater to dense brine should increase the critical Shields stress from 0.059 to 0.080. On Earth, differences in sediment density are typically small, with a few rare exceptions (e.g., pumice, and iron oxides and sulfides (e.g., Johnson et al., 2014)). Still, the increased density between granitic clasts ($R = 1.65$) and intact basalt ($R = 1.9$) should cause a decrease of the critical Shields stress on the order of 10% in steep channels ($\theta \geq 5°$), which is of similar magnitude as other factors affecting gravel mobility, such as the addition of 15% sand to a gravel sediment mixture (e.g., Wilcock et al., 2001). The variability of the critical Shields stress that is associated with relative submerged density indicates that sediment transport calculations should be performed in a material-specific manner, particularly on steep slopes and with exotic materials.

2.5 Conclusions

By performing flume experiments with both gravel ($R = 1.65$) and acrylic ($R = 0.15$) grains we were able to separate the relative roles of bed angle, θ, and relative roughness, D/H, in affecting the critical Shields stress required for sediment transport in open-channel flows. Both materials exhibited a sharp increase in the Shields stress at the onset of motion with increasing bed slope. For the same bed slope, the Shields stress required to mobilize the lighter acrylic material was roughly threefold larger than the gravel. Controls on bed form development and channel width indicate that the offset between our acrylic and gravel data sets is due mostly to differences in D/H at the onset of motion. Measurements of flow resistance in the same experiments confirm a strong dependence of flow resistance on D/H. A slight offset to higher flow resistance for the gravel experiments may be responsible for the higher critical Shields stresses for the gravel compared to the acrylic for a given value of relative roughness, owing to the slower velocities around the gravel grains than the acrylic grains.

The models of Lamb et al. (2008) and Recking (2009) are best suited to predict the critical Shields stress observed in our experiments because they explicitly account for particle emergence and altered velocity profiles in shallow flows. The Lamb model provides a slightly better fit by including an additional component to account for reduced intensity of turbulent fluctuations in shallow flows. Adding this component to the Recking model improved that fit as well.

Although the critical Shields stress for sediment motion was observed to increase with bed slope, the stream power at the onset of motion remained relatively constant for a

given material. Variability in the critical stream power values between experiment sets, however, indicates that a single value is not appropriate for all channel conditions and mechanistic explanations are not readily available. This notwithstanding, the consistency of critical stream power at the onset of motion in this study and others is encouraging for large-scale landscape evolution modeling (e.g., Howard, 1994; Tucker et al., 1997; Lague, 2003; Dibiase et al., 2011), which relies on parameterizing stream power using drainage area and slope.

Our results indicate that there exists no universal trend for τ_c^* with channel slope and instead that τ_c^* is a function of relative roughness, which can vary substantially with bed slope and with particle density. Moreover, the heightened critical Shields stress observed in our experiments, in which we controlled for bed forms and particle interlocking, represent baseline values that may be further augmented in natural shallow channels by morphologic form drag and particle interlocking. These relative roughness effects help to explain reduced bed load fluxes in steep channels. Our results are also important for reconstructing flow conditions on other planets, for example, where initial sediment motion of ice clasts has been used to constrain methane precipitation rates on Titan (Perron et al., 2006), or where transport of evaporite grains have been used to constrain flow rates of brines on Mars (Lamb et al., 2012).

Notation

C_f	friction factor
D	length of the intermediate axis of the median grain size (D_{50})
D_n	nth percentile grain diameter
F_D	drag force
F_L	lift force
Fr	Froude number
g	gravitational acceleration
H	flow depth
q_{surf}	surface discharge per unit width
q_{sub}	specific discharge of subsurface flow
R	relative submerged density of sediment
Re_p	particle Reynolds number
Re_s	subsurface Reynolds number
u	mean flow velocity
U	local flow velocity
u^*	shear velocity
W	channel width
α	turbulent fluctuation coefficient
θ	bed angle
ρ	density of water
ρ_s	material density of sediment
τ_b	total bed shear stress
τ^*	Shields stress
τ_c^*	Shields stress at the onset of motion
τ_{eff}^*	effective Shields stress
ϕ_g	particle friction angle of natural gravel
ϕ_a	particle friction angle of deformed acrylic spheres
ω	stream power per unit width
ω_c^*	non-dimensional stream power per unit width at the onset of motion

Acknowledgments

Funding was provided by NSF grants EAR-0922199 and EAR-1349115, the Terrestrial Hazards Observations and Reporting center (THOR) at Caltech, and the Keck Institute for Space Studies. The experimental data presented in Figures 5 to 9 are either present in Table 2.1 or may be calculated from data in Table 2.1 using equations included in the manuscript. We thank Brian Fuller for help with experiments. This paper was improved

by the helpful comments of two anonymous reviewers.

2.6 References

Aksoy, S (1973). "The influence of the relative depth on threshold of grain motion." In: *Proceedings of the International Association for Hydraulic Research International Symposium on River Mechanics*. Delft, Netherlands: Int. Assoc. for Hydraul. Res., pp. 359–370.

Archimedes (1897). "On Floating Bodies I." In: *Works of Archimedes*. Ed. by Thomas Little Heath. Cambridge University Press.

Ashida, K and M Bayazit (1973). "Initiation of motion and roughness of flows in steep channels." In: *Hydraul Res, Proc 15th Congress, Istanbul, Turkey* 1, pp. 475–484.

Bagnold, R A (1980). "An Empirical Correlation of Bedload Transport Rates in Flumes and Natural Rivers." In: *Proceedings of the Royal Society A: Mathematical, Physical and Engineering Sciences* 372.1751, pp. 453–473.

Bathurst, J C, H H Cao, and W H Graf (1984). *Hydraulics and sediment transport in a steep flume: Data from the EPFL study*. Tech. rep. Wallingford, U.K.

Bathurst, James C (1985). "Flow Resistance Estimation in Mountain Rivers." In: *Journal of Hydraulic Engineering* 111.4, pp. 625–643.

Bayazit, M (1976). "Free Surface Flow In A Channel Of Large Relative Roughness." In: *Journal of Hydraulic Research* 14.2, pp. 115–126.

Bettess, R (1984). "Initiation of sediment transport in gravel streams." In: *Proceedings of the Institution of Civil Engineers Part 2,* 77, pp. 79–88.

Buffington, J M and D R Montgomery (1997). "A systematic analysis of eight decades of incipient motion studies, with special reference to gravel-bedded rivers." In: *Water Resources Research* 33.8, pp. 1993–2029.

Buffington, John M and David R Montgomery (1999). "Effects of sediment supply on surface textures of gravelbed rivers." In: *Water Resources Research* 35.11, pp. 3523–3530.

Bunte, Kristin et al. (2013). "Critical Shields values in coarse-bedded steep streams." In: *Water Resources Research* 49.11, pp. 7427–7447.

Carollo, F, V Ferro, and D Termini (2005). "Analyzing turbulence intensity in gravel bed channels." In: *Journal of Hydraulic Engineering* 131.12, pp. 1050–1061.

Chiew, Yee-Meng and Gary Parker (1994). "Incipient sediment motion on non-horizontal slopes." In: *Journal of Hydraulic Research* 32.5, pp. 649–660.

Comiti, Francesco et al. (2007). "Field-derived relationships for flow velocity and resistance in high-gradient streams." In: *Journal of Hydrology* 340.1-2, pp. 48–62.

Costa, John (1983). "Paleohydraulic reconstruction of flash-flood peaks from boulder deposits in the Colorado Front Range." In: *GSA Bulletin* 94.8, p. 986.

Dey, Subhasish and Koustuv Debnath (2000). "Influence of streamwise bed slope on sediment threshold under stream flow." In: *Journal of irrigation and drainage engineering* 126.4, pp. 255–263.

Dibiase, Roman A and Kelin X Whipple (2011). "The influence of erosion thresholds and runoff variability on the relationships among topography, climate, and erosion rate." In: *Journal of Geophysical Research* 116.F4.

Ferguson, R I (2005). "Estimating critical stream power for bedload transport calculations in gravel-bed rivers." In: *Geomorphology* 70.1-2, pp. 33–41.

Ferguson, Robert I (2007). "Flow resistance equations for gravel-and boulder-bed streams." In: *Water Resources Research* 43, W05427.

— (2012). "River channel slope, flow resistance, and gravel entrainment thresholds." In: *Water Resources Research* 48.

Fernandez Luque, R and R Van Beek (1976). "Erosion and transport of bed-load sediment." In: *Journal of Hydraulic Research* 14.2, pp. 127–144.

Flammer, Gordon H, J Paul Tullis, and Earl S Mason (1970). "Free surface, velocity gradient flow past hemisphere." In: *Journal of the Hydraulics Division* 96.7, pp. 1485–1502.

Forchheimer, P H (1901). "Wasserbewegun Durch Boden." In: *Zeitschrift des Vereines Deutscher Ingenieure* 49-50, pp. 1736–1749–1781–1788.

Grant, Gordon E (1997). "Critical flow constrains flow hydraulics in mobilebed streams: A new hypothesis." In: *Water Resources Research* 33.2, pp. 349–358.

Gregoretti, C (2008). "Inception sediment transport relationships at high slopes." In: *Journal of Hydraulic Engineering* 134.11, pp. 1620–1629.

Grotzinger, J P et al. (2013). "Sedimentary Processes on Earth, Mars, Titan, and Venus." In: *Comparative Climatology of Terrestrial Planets* 1, pp. 439–472.

Hack, John Tilton (1957). *Studies of Longitudinal Stream Profiles in Virginia and Maryland*. U.S. Geological Survey.

Howard, A D (1994). "A detachment-limited model of drainage basin evolution." In: *Water Resources Research* 30.7, pp. 2261–2285.

Johnson, J E et al. (2014). "O2 constraints from Paleoproterozoic detrital pyrite and uraninite." In: *Geological Society of America Bulletin* 126.5-6, pp. 813–830.

Kirchner, J W et al. (1990). "The variability of critical shear stress, friction angle, and grain protrusion in waterworked sediments." In: *Sedimentology* 37, pp. 647–672.

Lague, Dimitri (2003). "Constraints on the long-term colluvial erosion law by analyzing slope-area relationships at various tectonic uplift rates in the Siwaliks Hills (Nepal)." In: *Journal of Geophysical Research* 108.B2, p. 2129.

Lamb, Michael P, William E Dietrich, and Jeremy G Venditti (2008). "Is the critical Shields stress for incipient sediment motion dependent on channel-bed slope?" In: *Journal Of Geophysical Research-Earth Surface* 113.F2, F02008.

Lamb, Michael P et al. (2012). "Were Aqueous Ripples on Mars Formed by Flowing Brines?" In: *Sedimentary Geology of Mars*. SEPM Special Publication, pp. 139–150.

Lorenz, Ralph D, Claire Newman, and Jonathan I Lunine (2010). "Threshold of wave generation on Titan's lakes and seas: Effect of viscosity and implications for Cassini observations." In: *Icarus* 207.2, pp. 932–937.

Meyer-Peter, E and R Mueller (1948). "Formulas for bed-load transport." In: *Proc. 2nd Congr. Int. Assoc. Hydraul. Res., Stockholm*, pp. 39–64.

Miller, Robert L and Robert J Byrne (1966). "The angle of repose for a single grain on a fixed rough bed." In: *Sedimentology* 6.4, pp. 303–314.

Mueller, E N et al. (2008). "Modeling bed-load rates from fine grain-size patches during small floods in a gravel-bed river." In: *Journal of Hydraulic Engineering* 134.10, pp. 1430–1439.

Mueller, E R, J Pitlick, and J M Nelson (2005). "Variation in the reference Shields stress for bed load transport in gravel-bed streams and rivers." In: *Water Resources Research* 41.4, W04006.

Nikora, Vladimir et al. (2001). "Spatially averaged open-channel flow over rough bed." In: *Journal of Hydraulic Engineering* 127.2, pp. 123–133.

Nitsche, Manuel et al. (2011). "Evaluation of bedload transport predictions using flow resistance equations to account for macro-roughness in steep mountain streams." In: *Water Resources Research* 47.8, W08513.

Parker, Chris, Nicholas J Clifford, and Colin R Thorne (2011). "Understanding the influence of slope on the threshold of coarse grain motion: Revisiting critical stream power." In: *Geomorphology* 126.1-2, pp. 51–65.

Parker, Gary, Peter C Klingeman, and David G McLean (1982). "Bedload and size distribution in paved gravel-bed streams." In: *Journal of the Hydraulics Division* 108.4, pp. 544–571.

Perron, J Taylor et al. (2006). "Valley formation and methane precipitation rates on Titan." In: *Journal of Geophysical Research: Solid Earth (1978–2012)* 111.E11.

Prancevic, J P, M P Lamb, and B M Fuller (2014). "Incipient sediment motion across the river to debris-flow transition." In: *Geology* 42, pp. 191–194.

Recking, A (2009). "Theoretical development on the effects of changing flow hydraulics on incipient bed load motion." In: *Water Resources Research* 45, W04401.

Rickenmann, D (2001). "Comparison of bed load transport in torrents and gravel bed streams." In: *Water Resources Research* 37.12, pp. 3295–3305.

Rickenmann, Dieter and Alain Recking (2011). "Evaluation of flow resistance in gravelbed rivers through a large field data set." In: *Water Resources Research* 47.7.

Scheingross, Joel S et al. (2013). "Influence of bed patchiness, slope, grain hiding, and form drag on gravel mobilization in very steep streams." In: *Journal Of Geophysical Research-Earth Surface* 118, pp. 1–20.

Shields, A (1936). "Anwendung der Ähnlichkeitsmechanik und der Turbulenzforschung auf die Geschiebebewegung." In: *Mitt. Preuss Versuchsanst. Wasserbau Schiffbau* 26.

Shvidchenko, A B and G Pender (2000). "Flume study of the effect of relative depth on the incipient motion of coarse uniform sediments." In: *Water Resources Research* 36.2, pp. 619–628.

Tosca, Nicholas J et al. (2011). "Physicochemical properties of concentrated Martian surface waters." In: *Journal of Geophysical Research* 116.E05004.

Tucker, Gregory E and Rudy Slingerland (1997). "Drainage basin responses to climate change." In: *Water Resources Research* 33.8, pp. 2031–2047.

Vollmer, Stefan and Maarten G Kleinhans (2007). "Predicting incipient motion, including the effect of turbulent pressure fluctuations in the bed." In: *Water Resources Research* 43.5.

Whipple, Kelin X and Gregory E Tucker (1999). "Dynamics of the stream-power river incision model: Implications for height limits of mountain ranges, landscape response timescales, and research needs." In: *Journal of Geophysical Research* 104.B8, p. 17661.

White, C M (1940). "The equilibrium of grains on the bed of a stream." In: *Proceedings of the Royal Society of ...*

Wiberg, Patricia L and Jim Dungan Smith (1987). "Calculations of the Critical Shear Stress for Motion of Uniform and Heterogeneous Sediments." In: *Water Resources Research* 23.8, pp. 1471–1480.

Wilcock, Peter R, Stephen T Kenworthy, and Joanna C Crowe (2001). "Experimental study of the transport of mixed sand and gravel." In: *Water Resources Research* 37.12, pp. 3349–3358.

Wong, M and G Parker (2006). "Reanalysis and correction of bed-load relation of Meyer-Peter and Müller using their own database." In: *Journal of Hydraulic Engineering* 132.11, pp. 1159–1168.

Yager, E, J Turowski, and D Rickenman (2012). "Sediment supply, grain protrusion, and bedload transport in mountain streams." In: *Geophysical Research ...*

Yager, E M, J W Kirchner, and W E Dietrich (2007). "Calculating bed load transport in steep boulder bed channels." In: *Water Resources Research* 43.7, W07418.

Zimmermann, A and M Church (2001). "Channel morphology, gradient profiles and bed stresses during flood in a step-pool channel." In: *Geomorphology* 40, pp. 311–327.

Zimmermann, André, Michael Church, and Marwan A Hassan (2010). "Step-pool stability: Testing the jammed state hypothesis." In: *Journal Of Geophysical Research-Earth Surface* 115, F02008.

Chapter 3

Particle friction angles in steep mountain channels

This chapter was adapted from the peer-reviewed journal article:

Prancevic, J. P., and M. P. Lamb, (2015) Particle friction angles in steep mountain channels, *J. Geophys. Res.*, 120 (2), 242–259, doi: 10.1002/2014JF003286

Abstract

Sediment transport rates in steep mountain channels are typically an order of magnitude lower than predicted by models developed for lowland rivers. One hypothesis for this observation is that particles are more stable in mountain channels due to particle-particle interlocking or bridging across the channel width. This hypothesis has yet to be tested, however, because we lack direct measurements of particle friction angles in steep mountain channels. Here we address this data gap by directly measuring the minimum force

required to dislodge sediment (pebbles to boulders) and the sediment weight in mountain channels using a handheld force gauge. At eight sites in California, with reach-averaged bed angles ranging from 0.5° to 23° and channel widths ranging from 2 m to 16 m, we show that friction angles in natural streams average 68° and are 16° larger than those typically measured in laboratory experiments, which is likely due to particle interlocking and burial. Results also show that larger grains are disproportionately more stable than predicted by existing models and that grains organized into steps are twice as stable as grains outside of steps. However, the mean particle friction angle does not vary systematically with bed slope. These results do not support systematic increases in friction angle in steeper and narrower channels to explain the observed low sediment transport rates in mountain channels. Instead, the spatial pattern and grain-size dependence of particle friction angles may indirectly lower transport rates in steep, narrow channels by stabilizing large clasts and channel-spanning steps, which act as momentum sinks due to form drag.

3.1 Introduction

Sediment within mountain channels moves intermittently. During active transport, sediment attacks the underlying bedrock, driving incision (e.g., Sklar et al., 2004). In large flood events, high sediment transport rates, and debris flows may pose serious hazards to life and infrastructure (e.g., Rickenmann, 2012; Prancevic et al., 2014). Between transport events, sediment provides structure to the channel bed (e.g., Church et al., 1998) that creates habitat for riverine fauna (e.g., Coulombe-Pontbriand et al., 2004)

and partly determines water flow rates (e.g., Aberle et al., 2003). Thus, determining the stability of sediment is necessary to better understand the evolution of mountainous landscapes and riverine habitats. Despite its importance, there are very few direct measurements in steep mountain streams of the particle friction angle, one of the key metrics of bed stability.

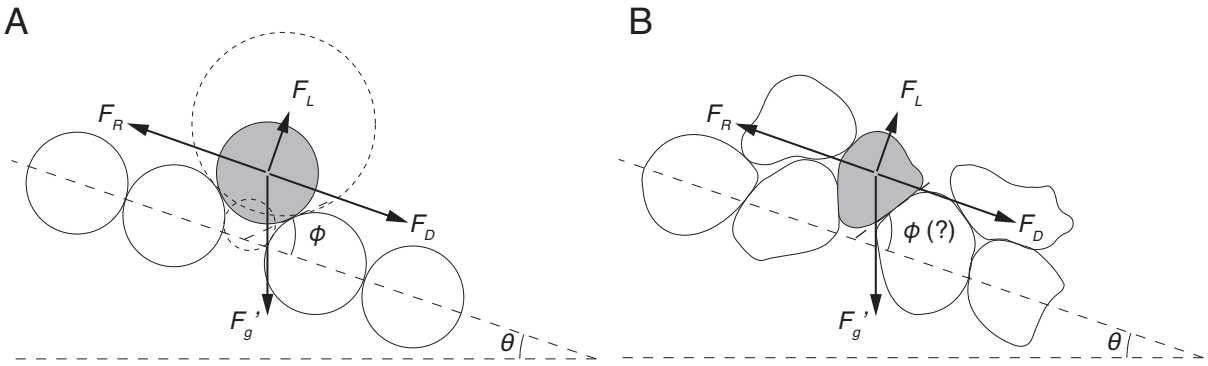

Figure 3.1: Two-dimensional schematics of (a) an idealized grain-pocket configuration and (b) a more realistic pocket with wedged and imbricated grains with relevant force vectors shown. The dotted circles in Figure (3.1a) illustrate the theorized effect of changing D/D_{50} on the particle friction angle. The small circle has a size of $D/D_{50} = 0.5$, and the large has a size of $D/D_{50} = 1.8$.

Sediment transport is the result of the driving fluid stress (skin friction and form drag) overcoming the resistive stress derived from the gravitational stability of a grain in its pocket between other grains (Fig. 3.1a) (e.g., Gilbert, 1914; Shields, 1936; Wiberg et al., 1987). Both sides of this stress balance exhibit complicated behavior due to turbulent fluid flow (e.g., Schmeeckle et al., 2007), complex bed geometry (e.g., Zimmermann et al., 2001), and a mixture of grain shapes and sizes (e.g., Miller et al., 1966). Consequently, the full distribution of driving stress-resisting stress combinations is difficult to predict, and we typically rely on representative, empirical relationships for predicting initial motion and bed load transport rates. These relationships were initially developed

for application to lowland rivers (Shields, 1936; Meyer-Peter et al., 1948; Miller et al., 1966) and are inadequate in describing sediment transport in steep, coarse-bedded environments, where bed load transport rates are typically an order of magnitude smaller than predicted (e.g., Rickenmann, 1997; Yager et al., 2007; Mueller et al., 2008). Even the onset of sediment transport in steep channels requires significantly higher bed shear stresses than expected (Bartnick, 1991; Mueller, E R et al., 2005; Lenzi et al., 2006b; Scheingross et al., 2013). There is debate as to whether the divergence between predictions and observations in steep channels is due to changes in granular stability, changes in flow hydraulics, or both (e.g., Church et al., 1998; Yager et al., 2007; Lamb et al., 2008; Recking, 2009; Zimmermann et al., 2010; Ferguson, 2012). Flume experiments with loose, unimodal sediment beds show that sediment stability increases and bed load transport rates are reduced in steeper channels with respect to predicted values, suggesting that these effects are in part due to changes in hydraulics (e.g., Gregoretti, 2008; Prancevic et al., 2014). Changes in grain stability have been difficult to evaluate in natural steep channels, however, due to limitations of standard measurement techniques (e.g., Miller et al., 1966; Kirchner et al., 1990; Buffington et al., 1992).

The resisting force that stabilizes a particle in a sediment bed is typically formulated as a simple Coulomb friction model:

$$F_R \leq \sum_i F_{n,i} \tan \phi \tag{3.1}$$

where F_R is the frictional force resisting motion, $F_{n,i}$ is the normal force exerted on grain from contact point i, and the friction coefficient is parameterized as the tangent of a

friction angle, ϕ. The particle friction angle is often idealized as the angle of inclination, relative to the channel bed slope, about the contact point between the grain in question and one of its downstream neighbors (e.g., Fig. 3.1a). This is appropriate in a simplified configuration in which, at the onset of motion, the only contact point for the grain in question is that of its downstream neighbor. In natural streambeds, this simplified configuration may not hold, however, and irregular bed packing, grain shape, and partial burial can cause multiple contact points to be important (e.g., Fig. 3.1b).

In many studies, the friction angle is measured directly using a tilting surface composed of fixed grains (e.g., natural pebbles, sand, or spheres) (Miller et al., 1966; Li et al., 1986; Kirchner et al., 1990; Buffington et al., 1992). One or more grains are placed on the fixed granular surface, which is tilted until a loose grain becomes unstable, and rolls or slides out of its pocket. The angle at which this occurs is the particle friction angle, and the driving and resisting forces are equal to the weight of the grain (W) times the sine and cosine of the particle friction angle, respectively (e.g., Miller et al., 1966). It is equivalent to measure particle friction angles in situ by measuring the force required to mobilize grains in a channel bed relative to their respective weights (Johnston et al., 1998). Laronne (1973) was the first to apply this methodology in a natural channel and the two friction angles he measured pulling parallel to the bed, $\phi = 62°$ and $\phi = 76°$, were much higher than those measured on tilting tables and typically assumed in bed load transport formulae. Following a similar methodology, Johnston et al. (1998) amassed the first extensive data set of in situ particle friction angles, but their study was limited to relatively low-sloping channels ($\theta < 3°$) and grains that lacked sorting and imbrication (Johnston et al., 1998). Downes et al. (1997) and Sanguinito et al. (2011) have also made

dislodgement force measurements in natural channels.

Results from previous laboratory (tilt table) experiments and field measurements have revealed a strong dependence on the size of the diameter of the test grain (D) relative to the roughness of the granular bed (e.g., D/D_{50}, in which D_n is the nth percentile grain size). Results show that large grains are less stable than smaller ones due to their propensity to rest higher on the surrounding grains (Fig. 3.1) and therefore at a lower angle to the average bed (Miller et al., 1966; Li et al., 1986; Kirchner et al., 1990; Buffington et al., 1992; Johnston et al., 1998). To capture this effect, mean friction angles for a specific grain size ($\overline{\phi}$) are typically modeled as a power law relationship:

$$\frac{\overline{\phi}}{\overline{\phi_{D_{50}}}} = \left(\frac{D}{D_{50}}\right)^{-\beta} \tag{3.2}$$

where $\overline{\phi_{D_{50}}}$ is the mean friction angle of the median grain size and β is an empirical constant, with typical ranges of $\overline{\phi_{D_{50}}} = 46^\circ$ to 66° and $\beta = 0.21$ to 0.46 for natural grains (Table 3.1). This relative grain size dependence in particle friction angle promotes mobility of larger grains relative to smaller grains, partially offsetting differences in grain weight (e.g., Wiberg et al., 1987; Solari et al., 2000). However, no friction angle data exist for steep mountain streams ($\theta > 3^\circ$), where particle mobility has been observed to be highly size selective (e.g., Brummer et al., 2003; Scheingross et al., 2013).

While there have been no direct measurements of particle friction angles in steep natural channels ($\theta > 3^\circ$), observations of sediment transport provide clues that grain stability may increase there relative to low-sloping channels. Researchers typically report sediment transport rates as a function of total bed shear stress (τ_b) normalized by grain

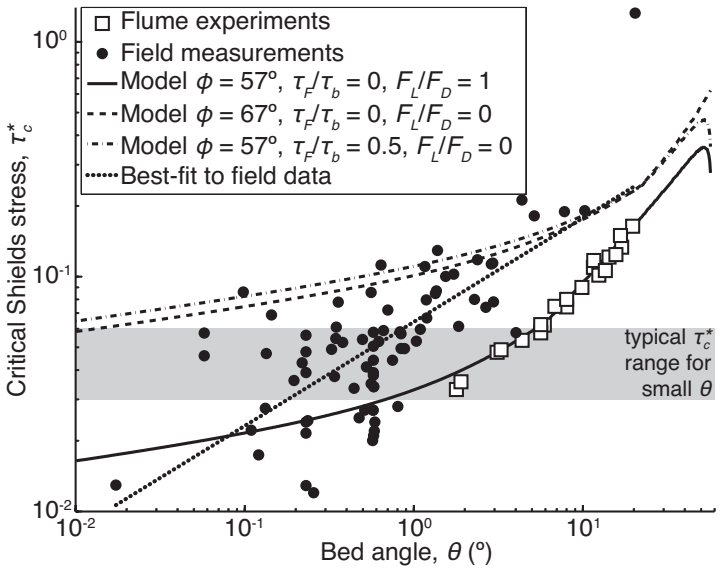

Figure 3.2: Compilation of field data and a subset of flume data (Prancevic et al., 2014) showing critical Shields stress at the onset of motion as a function of bed slope. The theoretical force balance of Lamb et al. (2008) is shown in the solid, dashed, and dash-dotted lines for various scenarios. The dotted line is the best fit curve to the compilation of field data (includes data from Montgomery et al. (1997) review and Andrews (1994) and Andrews (2000), Church et al. (2002), Whitaker et al. (2007), Mao et al. (2008), and Scheingross et al. (2013)), which are used for subsequent predictions of particle friction angle changes as a function of slope. Note that the exponent of this power law, $\tau_c^* = 0.39\tan^{0.44}\theta$, is larger than the fit presented in Lamb et al. (2008), $\tau_c^* = 0.15\tan^{0.25}\theta$, which includes both field and flume data and lacks data from Scheingross et al. (2013).

diameter (D), termed Shields stress: $\tau^* = \frac{\tau_b}{(\rho_s - \rho)gD}$, where g is the acceleration due to gravity, ρ is the material density of water, and ρ_s is the material density of sediment. Measurements at the onset of sediment motion reveal that grains require increased Shields stress to move in steeper channels in both the field (Bartnick, 1991; Andrews, 1994; Andrews, 2000; Church et al., 2002; Mueller, E R et al., 2005; Lenzi et al., 2006a; Whitaker et al., 2007; Mao et al., 2008; Scheingross et al., 2013) and laboratory flumes (Ashida et al., 1973; Bathurst et al., 1984; Olivero, 1984; Graf et al., 1987; Torri et al., 1988; Picon, 1991; Shvidchenko et al., 2000; Gregoretti, 2008; Prancevic et al., 2014) (Fig. 3.2). In addition, the threshold Shields stress required to mobilize material in the field is

higher relative to flume experiments for a given bed slope (Fig. 3.2). Researchers have also identified a correlation between changes in channel width and the threshold Shields stress such that narrower channels have grains that appear more stable (Zimmermann et al., 2010)(Fig. 3.3). Finally, this increased stability appears to continue after initial transport, and sediment transport rates are typically an order of magnitude smaller than predicted by sediment transport equations developed for lowland rivers (Rickenmann, 1997; D'Agostino et al., 1999). Despite observations that point to enhanced grain stability in steep streams, it remains an open question as to what degree this stability is due to enhanced granular friction or reduced effectiveness of water flow in transporting sediment with increasing channel slope.

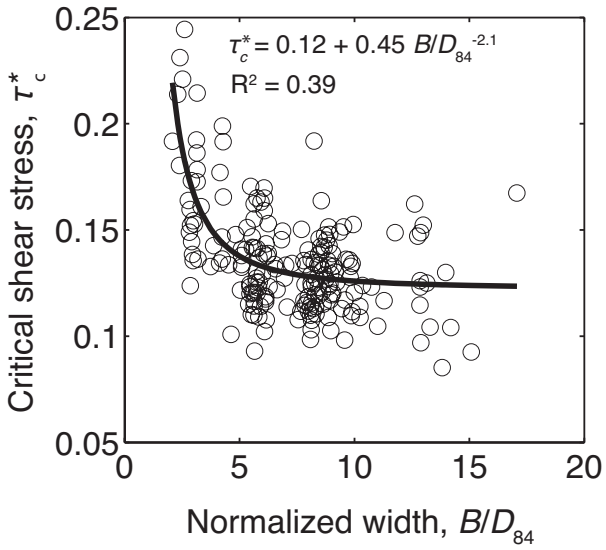

Figure 3.3: Adapted from experiments of Zimmermann et al. (2010) showing bed stability as a function of normalized width. The best fit curve is ours and is used in subsequent predictions of particle friction angle changes as a function of normalized width.

One mechanism to increase particle friction angles that is inherent to increased bed angle is the potential for increased normal forces from neighboring grains. In imbricated packing arrangements, grains become increasingly vertically stacked as slope increases.

This, however, should only have a strong effect on very steep slopes ($\theta \gg 6^\circ$), where the downstream component of gravity is of the same order as the bed-normal component. More complex grain interactions, including interlocking and jamming, may provide an additional means to alter particle friction angles. Grains in steep channels also tend to be more angular due to their small transport distances. Angular grains are known to have high particle friction angles from tilt table experiments (Miller et al., 1966), but the role of angularity in stabilizing grains may be more substantial in natural channels due to more prolonged water working and grain organization. Additional processes that may affect bed stability in steep mountain channels but are not present in lower sloping rivers ($\theta <\sim 1^\circ$) are the transport and deposition of debris flow material. The random grain organization of debris flow deposits relative to fluvial deposits may cause differences in grain stability (Major, 1997). Erosional (e.g., scour marks and plucking) and depositional (e.g., levees and snouts) evidence for debris flow transport may be found throughout the channel network steeper than $\theta >\sim 1^\circ$ due to long runout distances (Stock et al., 2006). However, experimental results suggest that fluvial transport can occur up to slopes of $\theta <\sim 22^\circ$ (Prancevic et al., 2014). Channel beds between these two bed slopes may contain debris flow deposits that have been reworked to varying degrees by subsequent fluvial transport.

The goal of this work is to characterize the distribution of particle friction angles present on steep channel beds without bias in our selection based on patchiness or imbrication. This is in contrast to the study of Johnston et al. (1998), which explicitly avoided any portions of the bed that exhibited spatial sorting or imbrication. We use in situ measurements from a force gauge collected on bed angles ranging from $\theta = 0.5^\circ$ to

Table 3.1: Compilation of relative grain size dependence

Investigator Location/Sediment type	$\overline{\phi_{D_{50}}}$	β
Miller and Byrne [1966]		
Natural Sand	57.3	0.3
Glass spheres, poorly sorted	45.7	0.32
Glass spheres, well-sorted	44.9	0.44
Li and Komar [1986]		
Crushed basalt	51.3	0.33
Spheres	20.4	0.75
Elllipsoidal natural grains	31.9	0.36
Kirchner et al. [1990] [a]		
Natural grains, poorly sorted, water-worked	55.2	0.31
Natural grains, poorly sorted, unworked	66.1	0.46
Buffington et al. [1992][a]		
Natural sediment surface, k_s = 4.1 mm	60	0.26
Natural sediment surface, k_s = 11.4 mm	51	0.28
Natural sediment surface, k_s = 14.0 mm	54	0.21
Natural sediment surface, k_s = 14.5 mm	46	0.21
Natural sediment surface, k_s = 45.0 mm	52	0.24
Johnston et al. [1998][a]		
Pacific Creek	61.9	0.28
Van Duzen River	49.1	0.45
Sagehen Creek	51.6	0.3
Colorado River	55.5	0.14
Present Study		
Sespe Ck thalweg	70.1	-0.01
Sespe Ck bar	70.1	-0.01
Rose Valley trib	65.4	-0.01
Arroyo Seco	71.2	-0.01
Block Ck	70.8	0.17
San Oline Ck	65.6	0.17
Tumble Ck	65.6	0.17
Rattlesnake Ck	67.9	0.17

[a] $\overline{\phi_{D_{50}}}$ refers to the median friction angle of the median grain size in Kirchner et al. [1990], Buffington et al. [1992], and Johnston et al.'s [1998] studies. In all other studies, $\overline{\phi_{D_{50}}}$ refers to the mean friction angle of the median grain size.

23° to test the hypothesis that increased particle friction angles in steeper channels contribute to increased threshold Shields stress. We also test the hypothesis that increased particle friction angle in natural channels compared to laboratory flumes contributes to the offset in respective threshold Shields stresses.

3.2 Theoretical Expectations

In order to establish baseline predictions for particle friction angle variability, we utilize the force balance model of Lamb et al. (2008) to solve for the particle friction angles that yield the observed critical Shields stress in Figures (3.2) and (3.3). In addition to particle friction angle, there are other unconstrained parameters in the model that could also be used to attempt to match the model to observations, including most notably momentum loss to form drag (which will be discussed in section 5.5). Moreover, there are other important factors in natural rivers (e.g., grain burial and bed surface patchiness) that are not incorporated in the simple 1-D model at all. Our goal in performing this exercise is not to assert that the model is correct nor that the discrepancy between model and observations is purely a result of systematic variations in particle friction angles. Rather, these comparisons are useful because they allow us to recast the qualitative hypothesis that systematic variations in particle friction angles can explain the change in the critical Shields stress with channel slope or jamming ratio (Figs. 3.2 and 3.3) into quantitative expectations that can be compared to field data. Nullifying this hypothesis, in contrast, would indicate that the trends in Figures (3.2) and (3.3) must be explained in part by other factors (e.g., enhanced form drag).

The Lamb et al. (2008) model follows that of Wiberg et al. (1987) by balancing the forces pulling the grain downslope (gravity and fluid drag stress, F_D) with the frictional resisting force of the pocket, F_R. Both models calculate F_R at the onset of motion by substituting the total normal force in equation (3.1) with the weight of the grain normal to the bed minus the lift force:

$$F_R = [(\rho_s - \rho)V g \cos\theta - F_L] \tan\phi \tag{3.3}$$

where V is the volume of the particle and F_L is the hydrodynamic lift force pulling the grain away from the bed (e.g., Fig. 3.1). By solving for the lift and drag forces in terms of bed shear stress, they present an expression for the Shields stress at the onset of motion as an explicit function of flow velocities around the grain:

$$\tau_c^* = \left(\frac{1}{1 - \tau_F/\tau_b}\right) \frac{2}{C_D \delta} \frac{u_*^2}{\langle u^2 \rangle} \frac{\tan\phi \cos\theta - \sin\theta}{1 + F_L/F_D \tan\phi} \tag{3.4}$$

where τ_F/τ_b is the ratio of bed shear stress expended on morphologic form drag to the total bed shear stress, C_D is the empirical drag coefficient that is set to $C_D = 0.9$ following Lamb et al. (2008), δ is a geometric variable that adjusts according to the grain ρ_s exposure to and emergence from the flow (Lamb et al., 2008), $u_* = \sqrt{\frac{\tau_b}{\rho}}$ is the shear velocity of the flow, u is the time-averaged velocity, the angle brackets indicate spatial averaging over the cross-sectional area of the grain, and F_L/F_D is the ratio of lift to drag forces acting on the grain. We can also solve equation (3.4) explicitly for particle friction angle:

$$\tan\phi = \frac{\left(\frac{1}{1-\tau_F/\tau_b}\right) \frac{2}{C_D\delta} \frac{u_*^2}{\langle u^2 \rangle} \sin\theta + \tau_c^*}{\left(\frac{1}{1-\tau_F/\tau_b}\right) \frac{2}{C_D\delta} \frac{u_*^2}{\langle u^2 \rangle} \cos\theta - F_L/F_D \tau_c^*} \tag{3.5}$$

allowing us to calculate the expected particle friction angle given a threshold Shields stress and some constraint on the velocity profile, drag coefficient, lift-to-drag ratio, and stress loss to form drag.

It is important to note that the lift force presented in equations (3.4) and (3.5) is assumed to reduce the frictional resistance by directly reducing the normal force in equation (3.1). This is appropriate if the parameterization of normal forces in equation (3.3) is correct. However, if there are additional normal forces from the weight and interlocking of surrounding grains (e.g., Fig. 3.1b), the effect of lift force on the grain of interest is convoluted by the effect of lift force on the surrounding grains. In addition, direct measurements of lift forces have shown that the lift force is consistently much smaller than drag force and it does not increase with increased drag force as expected (Schmeeckle et al., 2007). Because we cannot reliably predict the effect of lift force on particle motion, we consider a range in lift-to-drag forces between $0 \leq F_L/F_D \leq 1$ for our model predictions. In order to apply equation (3.4) to steep, shallow flows, the Lamb et al. (2008) model incorporates hydraulic changes observed in shallow conditions. The model applies a quadratic bed-normal velocity profile, $\frac{u}{u_*} = \frac{z}{0.12D_{50}}\left(1 - \frac{z}{2H}\right)$, where z is the distance from the mean bed elevation and $z = H$ at the water surface (following data from Nikora et al. (2001)). In addition, it accounts for reduced turbulent intensity in shallow flows, $\frac{\sigma_u}{u_*} = 0.2\left[5.62\log\left(\frac{H}{D_{50}}\right) + 4\right]$ where σ_u is the temporal standard deviation of flow velocity at the tops of grains (following data from Carollo et al. (2005)). In cases where the depth of flow is smaller than the size of the bed sediment, the model includes the effects of reduced buoyancy and cross-sectional exposure by adjusting δ in equation (3.4) following Lamb et al. (2008). Inclusion of these slope-dependent effects results in an acceptable fit to the experimental data without momentum loss to morphologic form drag (Prancevic et al., 2014) (Fig. 3.2). The friction angle used to compare the Lamb model against Prancevic et al. (2014) experimental study ($\phi = 57°$) was measured using

a fixed-bed tilt table, which mimicked the conditions of a fluvially unworked bed surface, devoid of interlocking and steps.

The trend of increased threshold Shields stresses on steeper slopes is offset to even higher values in the field, as compared to flume experiments (Fig. 3.2). This offset is typically attributed to form drag. It has been well established that fluid momentum is consumed by the large pressure differential across bed forms caused by flow separation (e.g., Smith et al., 1977; Kostaschuk et al., 2004). If the pressure differential that results from this separation acts on an immobile obstacle (e.g., large bed form or boulder) rather than mobile grains, then the total stress required to transport sediment increases. The stress lost to these obstacles is termed "morphologic form drag" and is the most common explanation for the observed offset of the threshold Shields stress in field studies (e.g., Wiberg et al., 1991; Millar, 1999; Nitsche et al., 2011; Ferguson, 2012; Yager et al., 2012; Scheingross et al., 2013). Reported ratios of stress lost to form drag and total stress range between $\tau_F/\tau_b = 0$ and 0.9 for natural rivers (Millar, 1999). Alternatively, this offset may be due to differences in bed structure leading to higher particle friction angles in the field than in the laboratory. Field measurements collected by Laronne (1973) suggest that naturally organized beds are more stable than laboratory beds (Table 3.1). This observed difference in particle friction angles ($\sim 10^\circ$) could explain the majority of sediment transport data from the field, according to theoretical modeling (Fig. 3.2).

By calculating a least squares linear regression to the log-transformed field data (Fig. 3.2), we can input the best fit Shields stress, $\tau_c^* = 0.064\theta^{0.44}$ ($R^2 = 0.25$), into equation (3.5) to predict how the particle friction angle needs to change as a function of slope to explain the observed field data. Note that there is no physical reason to expect a power

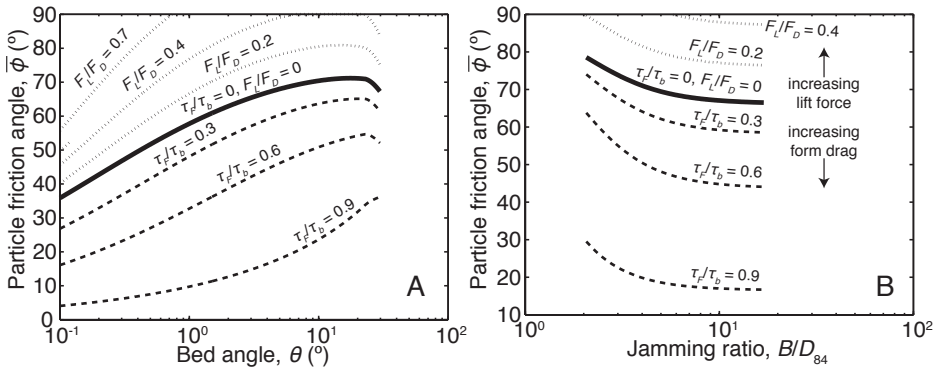

Figure 3.4: Predicted particle friction angle as a function of (a) bed angle and (b) jamming ratio. Predictions were calculated using a best fit to the available field data (Fig. 3.2) and flume data (Fig. 3.3) and equation (3.7). The solid line in each plot is the model prediction for no morphologic form drag and no lift force. The dashed lines are the contours with no lift force ($F_L/F_D = 0$) but increasing morphologic form drag. The dotted lines are the contours with no form drag ($\tau_F/\tau_b = 0$) but increasing lift force.

law relationship between τ_c^* and θ (e.g., Lamb et al., 2008), but for these field data from steep channels, it appears to be the most appropriate approximation. Fig. 3.4a shows a wide range in possible trends between particle friction angle and slope for different values of lift-to-drag ratio and momentum loss to form drag. For any constant pair of values of F_L/F_D and τ_F/τ_b, it is expected that the particle friction angle will increase by $\sim 30^\circ$ between bed angles of $\theta = 0.1^\circ$ and 10°. Note that because Lamb et al. (2008) model attempts to account for reduced effectiveness of water flow in mobilizing sediment at steep slopes, the expected variations in friction angle with bed slope are conservative. For example, should the Wiberg et al. (1987) model be used instead, friction angles would need to vary with bed angle over a much wider range to reconcile the model and observations.

Steep low-order channels also tend to have narrow widths relative to the size of bed sediment. Results from flume experiments indicate that channel narrowing relative to

grain size (i.e., decreasing jamming ratio: B/D_{84}) results in increased threshold Shields stress, independent of changes in bed slope (Zimmermann, 2010) (Fig. 3.3). The experiments revealed that interlocking grains formed stable ribs ("steps") across sufficiently narrow channel widths ($B/D_{84} <\sim 8$). Steps still formed at larger jamming ratios, but they were found to be less resistant to motion. The formation of steps has two hypothesized effects on the transport of sediment: increasing the particle friction angle of grains within the step (e.g., Zimmermann et al., 2010) and, subsequently, increasing the momentum lost to morphologic form drag (Yager et al., 2012). We used a trust-region nonlinear optimization to find the best fit between threshold Shields stress and jamming ratio (Zimmermann et al., 2010): $\tau_c^* = 0.12 + 0.45(B/D_{84})$ (R^2= 0.39). Note that the critical Shields stress is expected to be asymptotic to a base value of $\tau_c^* = 0.12$ for wide channels, which is reasonable for the typical bed slope of the experiments of Zimmermann et al. (2010) ($\theta = 4.5°$) (Prancevic et al., 2014). Inputting this best fit relationship into equation (3.5) shows that particle friction angles are expected to decrease by 10° with an increase in jamming ratio from B/D_{84}= 2 to 17 (Fig. 3.4b). We did not extend these expectations outside of the tested range of Zimmermann et al. (2010). Again, a wide range in curves results from the range of possible values of F_L/F_D and τ_F/τ_b.

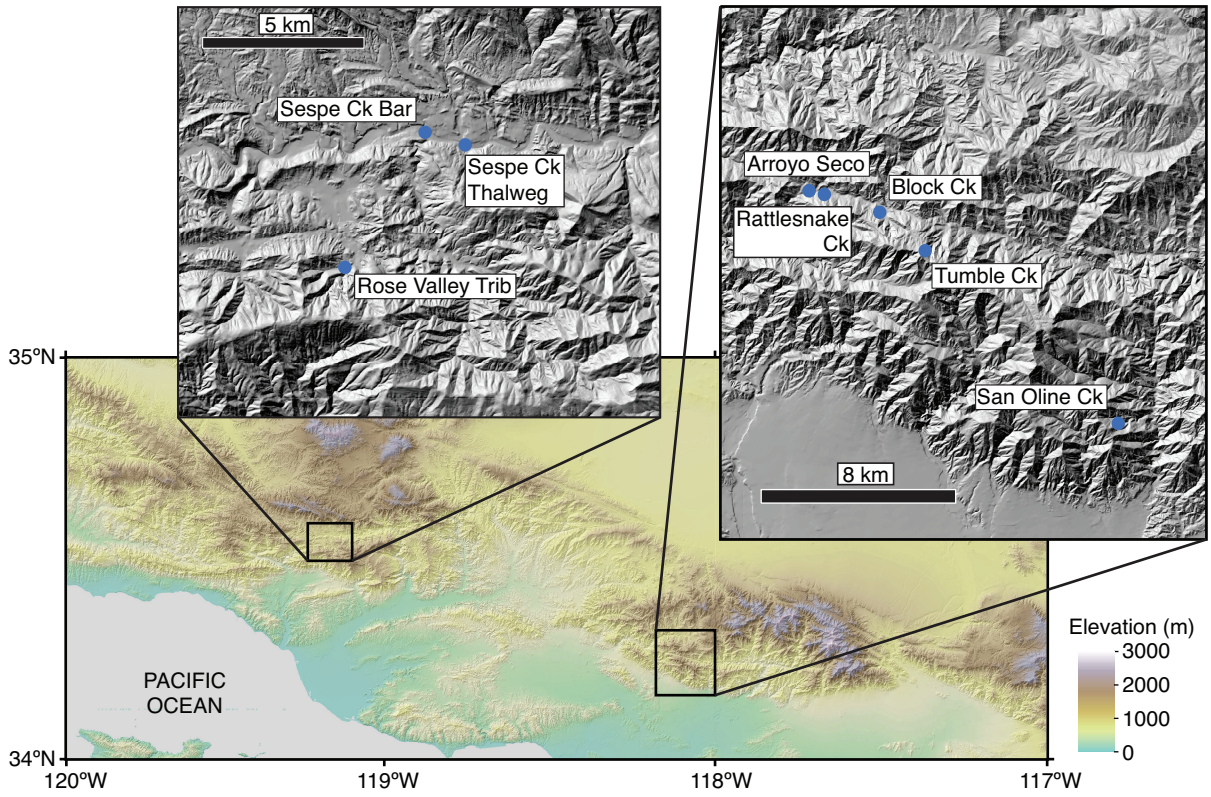

Figure 3.5: Location map of the study sites.

3.3 Methods

3.3.1 Study Sites

We visited a total of eight field sites in Southern California during the summer and fall of 2011 and 2013. The sites were located in either the San Gabriel Mountains (five sites total) or the Transverse Mountain Ranges (three sites total) in Southern California (Fig. 3.5). The sites were chosen to test a wide variety of channel slopes ($\theta = 0.5°$ to $23°$), width-to-grain size ratios ($B/D_{84} = 9$ to 64), and fluvial sorting (Fig. 3.6 and Table 3.2). Note that our smallest jamming ratio is larger than the critical jamming ratio proposed by Zimmermann et al. (2010), indicating that there should not be resistant force chains forming across the channel width. We timed visits to avoid any surface water, which

would introduce ambiguity to measured pulling forces due to concomitant buoyancy and hydraulic forces. All sites but Sespe Thalweg and Sespe Bar exhibited signs of debris flow transport with incomplete fluvial sorting, consistent with their respective proximity to hillslopes and tributaries much steeper than the critical slope for en masse failure (Prancevic et al., 2014). At each site, we laid a measuring tape longitudinally along the thalweg of the channel extending 60 to 100 m. We measured the longitudinal profile of the sampling area along this tape using a laser range finder noting the presence of steps. Channel bed slope was calculated as the slope of the best fit line to each profile. At minimum, grain size distributions were calculated by sampling a grain at every meter along this measuring tape (i.e., grid-by-number (Bunte et al., 2001)). At some sites, an additional Wolman pebble count of 100 grains was performed (Data sets S2a to S2h in the supporting information). We also made measurements of channel width at each site. For Sespe Creek Bar and Sespe Creek Thalweg, the width was measured within a discernable elevated flooding surface (Figs. 3.6a and 3.6b). Widths at Arroyo Seco, Block Creek, and Rattlesnake Creek were defined as the distance between debris flow levees (Figs. 3.6d, 3.6e, and 3.6h). Rose Valley Tributary, San Oline Creek, and Tumble Creek were flanked on either side by steep hillslopes, and the channel width was defined by the zone of exposed coarse clasts between these hillslopes (Figs. 3.6c, 3.6f, and 3.6g).

Table 3.2: Site characteristics and average friction angles

Site	Bed angle θ (°)	Width, B (m)	Grain Size, $D_{16}/D_{50}/D_{84}$ (cm)	Jamming ratio, B/D_{84}	Sorting coefficient, σ	Step cover (%)	Friction angle measurements, n	Mean norm. friction angle, $\overline{\phi_N}$(°)	Tenth percentile friction angle, ϕ_{10}(°)	Friction angle standard dev., s(°)
Sespe Ck thalweg	0.5	13	8.8/29/54	24	1.3	5	29	70.3	52.9	11.7
Sespe Ck bar	0.7	16	6.0/14/25	64	1.0	0	31	70	48	14.5
Rose Valley trib	2.9	3	5.0/12/25	12	1.2	3	32	65.4	44.1	14.2
Arroyo Seco	3.7	4	7.0/16/29	14	1.0	30	35	71.4	58.5	12.8
Block Ck	8.4	5	4.4/15/29	17	1.4	8	33	70.7	51.5	13.2
San Oline Ck	9.1	2.5	9.0/17/29	9	0.9	16	33	65.6	49.6	13.7
Tumble Ck	17	6	5.5/16/41	15	1.5	25	36	65.4	47.6	14.5
Rattlesnake Ck	23	2	3.5/8.0/14	14	1.0	3	46	68.1	47.2	13.9

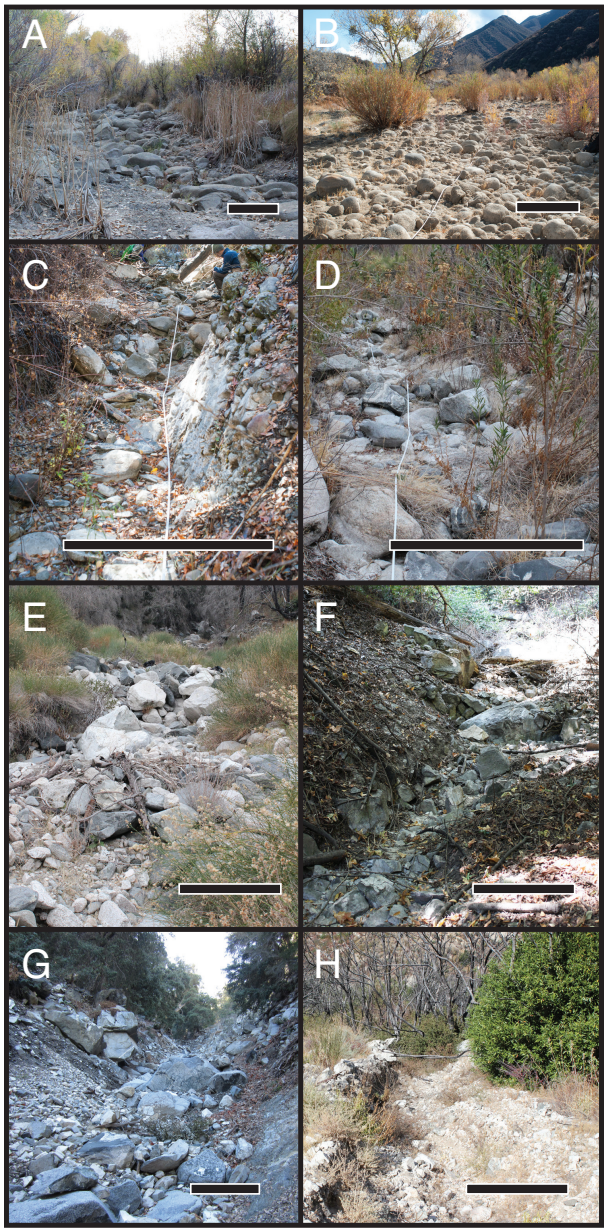

Figure 3.6: Representative photographs for all field sites. (a) Sespe Creek Thalweg, (b) Sespe Creek Bar, (c) Rose Valley Tributary, (d) Arroyo Seco, (e) Block Creek, (f) San Oline Creek, (g) Tumble Creek, and (h) Rattlesnake Creek. The scale bars correspond roughly to 1 m in the foreground.

Grain size distributions were broad at all sites (Fig. 3.7), with large sorting coefficients ($\sigma \geq 0.9$) (Inman, 1952) (Table 3.2):

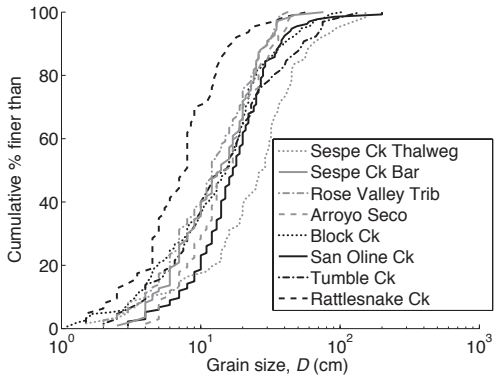

Figure 3.7: Grain size distributions for all field sites.

$$\sigma = \frac{1}{2}(\log_2 D_{84} - \log_2 D_{16}) \tag{3.6}$$

The median grain diameter for six of the eight sites is between 12 and 17 cm, while Sespe Creek Thalweg is considerably coarser (D_{50}= 29 cm), and Rattlesnake Creek is considerably finer (D_{50}= 8 cm). The channel widths generally narrow with increased slope and consequently steps occur preferentially in steeper reaches (Figs. 3.8). One clear exception is Rattlesnake Creek, which sits close to the maximum slope for fluvial transport and shows no sorting into patches or steps (Fig. 3.6h).

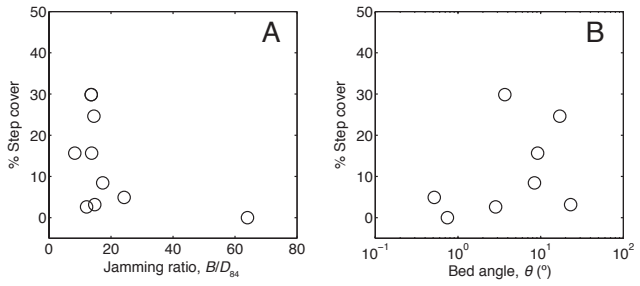

Figure 3.8: Percentage of the sampling grid composed of boulder steps for each site presented as a function of (a) jamming ratio and (b) channel slope.

3.3.2 Boulder Pulling Methodology

In order to measure particle friction angles in situ, we utilized a handheld digital force gauge to measure the force required to dislodge a particle from its pocket and the weight of that particle (Fig. 3.9). The force gauge is a Shimpo FGE-500HX, which has a 2500 N capacity (greater than our maximum pulling strength, which was limited to 2000 N under ideal pulling conditions), ±5 N accuracy, and a sampling rate of 1000 Hz. The device records the peak force during the measurement period to prevent reading error while dislodging the clast. Early measurement attempts with a force gauge that did not record peak forces resulted in much smaller recorded pulling forces, indicating substantial error that may be present in other studies as well. Working upstream along the measuring tape used for the longitudinal profile, we sampled clasts over a regular 1 m spacing. This sampling scheme yields a grid-by-number friction angle distribution (Bunte et al., 2001). Clasts were never skipped unless they were outside of our measurement force range, and a single clast was never measured twice.

In order to fasten the force gauge to the test grain, a length of webbing was wrapped around the grain and hooked to the force gauge. If the webbing could not be secured around the clast without disturbing interlocked neighboring grains, we drilled a 3/16" bolt into the clast and attached an eye bolt on which we could pull (Fig. 3.9). Grains were pulled downstream, parallel to the inferred flow direction, and along an axis that passed approximately through the center of the exposed mass to mimic an evenly distributed fluid force. For each grain that was pulled, we also measured the three principal axes, the protrusion of the grain relative to the upstream channel bed, and the plain-view

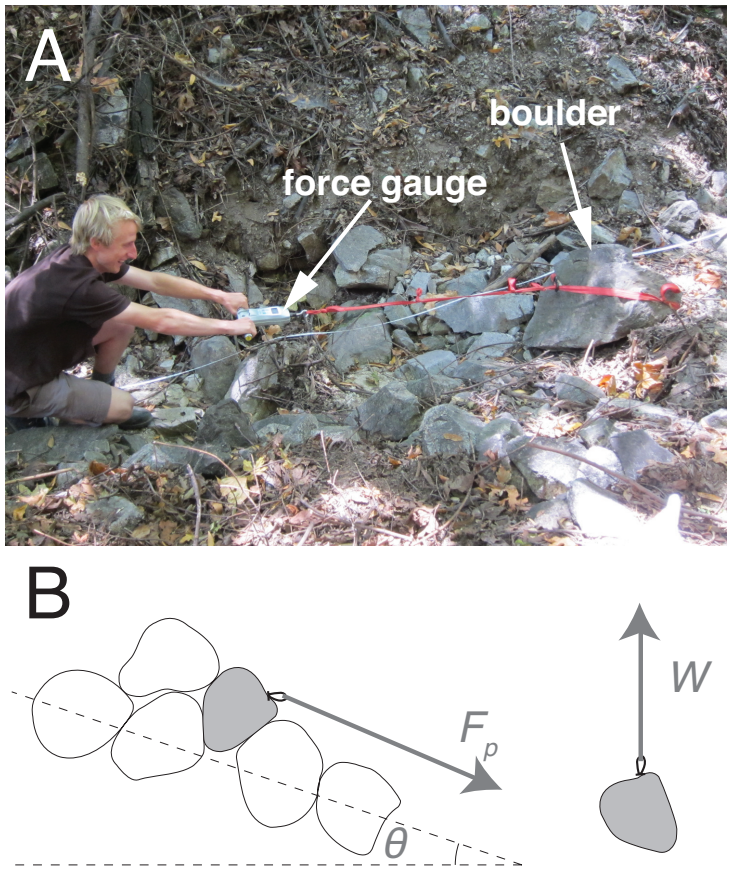

Figure 3.9: (a) Annotated photograph at San Oline Creek and (b) schematic of our setup for measuring the forces required to dislodge clasts (F_p), as well as weight (W).

cross-sectional area exposed at the surface. We made qualitative notes of particle burial, imbrication, angularity, and wedging and recorded whether or not the particle was in a step, which we identified as width-spanning breaks in elevation dominantly composed of coarse ($> D_{50}$) clasts (Montgomery et al., 1997).

During dislodgement, a dry particle experiences three forces: pulling force directed downstream (F_p), the downstream component of the weight vector ($W \sin\theta$), and the frictional resistance that is parameterized here using the bed-normal component of the weight ($\sum_i F_{n,i} = W \cos\theta$ in equation (3.1)). At the onset of motion, these forces balance along the downstream axis as

$$F_p + W \sin\theta = F_f = W \cos\theta \tan\theta \tag{3.7}$$

Rearranging, the friction angle can be solved for explicitly as

$$\tan\phi = \tan\theta + \frac{F_p}{W \cos\theta} \tag{3.8}$$

Because requisite pull force was typically higher than the weight, this led to a sampling bias at both ends of our data range. A boulder that weighs more than 2000 N will likely require a pull force higher than our strength limit and is effectively "stuck." The largest grain successfully pulled at each site was between the 83rd and 100th percentiles of its respective grain size distribution. Conversely, a small pebble with a pull force of 10 N will likely have an irresolvable weight. The lower end bias was circumvented by using grain size measurements to estimate the weight, but estimating pull forces for the higher end bias is not possible, leading to a bias toward lower friction angles for coarse grains, on average.

3.4 Results

We collected a total of 275 data points within our range of measurable forces (Fig. 3.10 and Data set S1 in the supporting information). The mobilization forces and particle weights vary over three orders of magnitude, reflecting the wide grain size distributions at each of these sites. The calculated friction angles vary between a modest $\phi = 27°$ and a near-vertical $\phi = 89°$, with sample standard deviations at each site ranging between $s = 12°$ and $15°$ (Table 3.2). Note that equation (3.8) requires the force-to-weight ratio to be

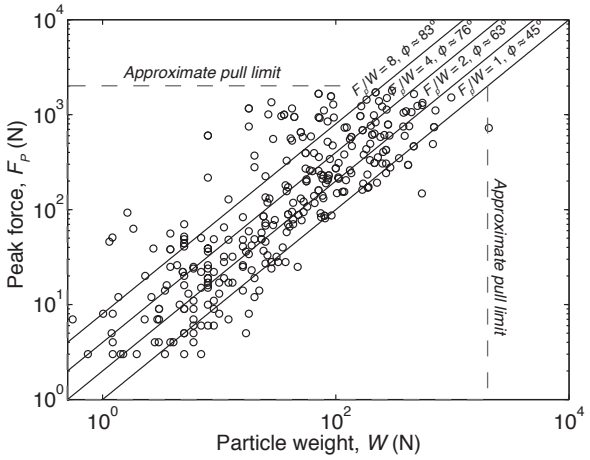

Figure 3.10: Peak force required for mobilization plotted against particle weight for all sites and measured clasts. The parallel solid lines indicate friction angle values assuming a horizontal bed. Actual values used in subsequent plots and analyses are slightly higher, reflecting the sloping bed (equation (3.7)). The dashed lines indicate the maximum force we were able to apply.

infinite to achieve a particle friction angle of $\phi = 90°$. After normalizing the collected data to remove the observed relationship between ϕ and D/D_{50}, we tested for any additional dependence on other grain characteristics, slope, and jamming ratio in order to tease out the competing effects.

3.4.1 Particle Friction Angle and Grain Characteristics

To investigate the effect of relative grain size on particle friction angle at our study sites, in this section we binned the data into four size classes with breaks at $D/D_{50} = 0.67$, 1.0, and 1.5. Because our data points are distributed over several slopes and field sites, we grouped sites that exhibited similar trends between relative grain size and particle friction angle. A clear distinction in data existed between moderately sloping sites ($\theta < 5°$) and steep sites ($\theta > 5°$), and so we chose to group the data based on this criterion. To

compare relative grain size effects across several sites, we divided all data by the mean particle friction angle of the median grain size at each site ($\phi/\overline{\phi_{D_{50}}}$). This process helps to reduce some of the variability induced by grouping sites together; however, variability due to small differences in trends (i.e., β) persists, and the global trend that results likely deviates slightly from the actual trend at each site.

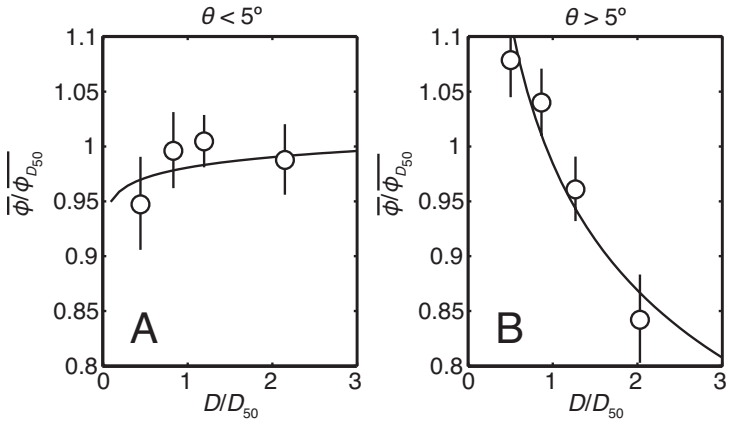

Figure 3.11: Mean particle friction angle as a function of relative grain size for (a) the relatively shallow sloping ($\theta < 5°$) and (b) steep sites ($\theta > 5°$). Friction angle values are normalized by the mean friction angle for the median grain size for each site. The error bars are the standard error of the measured values.

The power law relationship between relative friction angle ($\overline{\phi}/\overline{\phi_{D_{50}}}$) and relative grain size (D/D_{50}, equation (3.2)) for these two slope regimes was calculated by performing a least squares linear regression on all data in log-log space. Binned geometric means are shown in linear space in Fig. 3.11 for ease of viewing. Unlike most studies of particle friction angle (Miller et al., 1966; Kirchner et al., 1990; Buffington et al., 1992; Johnston et al., 1998), our measured particle friction angles for $\theta < 5°$ exhibits no trend with relative grain size outside of the standard error of $\beta = 0.014 \pm 0.032$ (Fig. 3.11a and Table 3.1). This indicates that the trend between relative grain size and particle friction angle is less pronounced compared to previous studies. A similarly reduced trend was

observed at the Pilgrim Creek and Colorado River sites in the study by Johnston et al. (1998) and is attributed to particle embedment. Data collected for $\theta > 5°$ exhibit a trend closer to those previously published (Fig. 3.11b), with $\beta = 0.180 \pm 0.032$. Still β is smaller in these channels than most previously reported values, both from tilt table experiments and Johnston et al.'s study of in situ particle friction angles (Table 3.1).

The tendency for larger-than-median grains to have lower particle friction angles is thought to be, in part, the result of larger grains resting on smaller grains with lower contact angles (Fenton et al., 1977; Kirchner et al., 1990). Within a natural streambed that lacks regular organization, relative grain size may not consistently predict the protrusion of a test grain from the bed. Grain protrusion, p, was measured independently in our field investigation as the maximum distance that the test grain extends above the bed surface (Data set S1 in the supporting information), measured relative to the height of the bed one grain-length upstream of the high point of the test grain. The correlation between p/D and ϕ for our entire data set is poor ($R^2 = 0.05$), indicating that protrusion is not a good predictor of particle friction angle.

The Corey shape factor, CSF $= c/\sqrt{ba}$, where a, b, and c are the lengths of the maximum, intermediate, and minimum principal axes of the test grain, respectively, has also been shown to correlate with particle friction angle previously (Johnston et al., 1998). However, the correlation between CSF and ϕ for our data set is also extremely poor ($R^2 = 0.006$). In order to remove the relative grain size effect from the subsequent analyses, we define a normalized friction angle of each individual measurement: $\phi_N = \phi \left(\frac{D}{D_{50}}\right)^{-\beta}$, where $\beta = 0.180$ for $\theta > 5°$ and $\beta = 0.014$ for $\theta < 5°$. This normalization allows us to collapse all measurements to the expected friction angle for the median particle size

and therefore allows us to test for the effects of channel slope and jamming ratio without covarying effects from D/D_{50}.

3.4.2 Particle Friction Angle and Channel Bed Slope

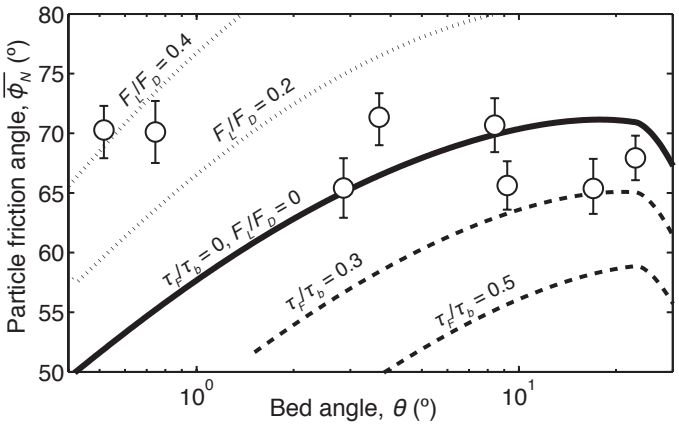

Figure 3.12: Mean normalized friction angle as a function of channel slope. The solid line is the model prediction (equation (3.4)) for no morphologic form drag and no lift force, as inverted from available field data. The dashed lines are the contours with no lift force but increasing morphologic form drag. The dotted lines are the contours with no form drag but increasing lift force.

We compare the normalized friction angles averaged at each site ($\overline{\phi_N}$) against reach bed angle (θ) to test for slope dependence in particle friction angle at our sites. It should be noted that several studies have come to the logical conclusion that those grains with the lowest particle friction angle are the first to move and therefore the most important for describing incipient motion (Kirchner et al., 1990; Johnston et al., 1998; Schmeeckle et al., 2003). The tenth percentile of each site's friction angle distribution, ϕ_{10}, generally scales with the mean (Table 3.2) and would yield similar findings in the subsequent analyses. However, due to the small number of data for each site, we use the mean normalized friction angle as a more robust characterization of the friction angle distribution.

Plotting the mean normalized friction angle and standard error versus bed slope reveals that grains are not more stable on steeper slopes for the sites visited in this study and that friction angle measurements do not match any of the predicted trends with constant values of F_L/F_D and τ_F/τ_b (Fig. 3.12). No trend, positive or negative, exists outside of the standard error of our study sites, and the standard deviation observed at any given site is much higher than the range of average values when comparing between sites (Table 3.2). The mean friction angles at all slopes are considerably higher than those previously reported for low-sloping channels and for tilt table measurements (Table 3.1).

3.4.3 Particle Friction Angle and Relative Width

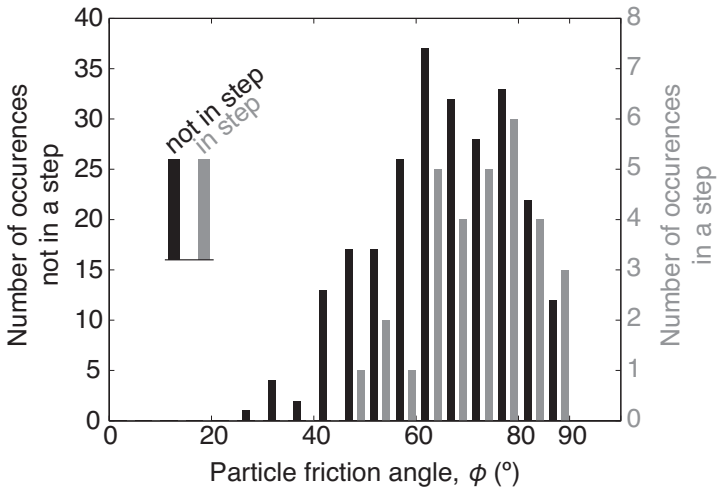

Figure 3.13: The number of particle friction angle measurements at all sites binned into 5° intervals for grains measured in steps (gray) and grains measured outside of steps (black).

In addition to channel bed slope, we compared the mean normalized friction angle, $\overline{\phi_N}$, to the jamming ratio, B/D_{84}, at each site. Step coverage within the channel increases sharply with decreased jamming ratio (Figs. 3.8a). Also, the mean of the normalized particle friction angles of grains lodged in steps is statistically higher than that of grains

measured outside of steps (two-sample t test, $p = 0.013$). In particular, histograms of normalized particle friction angles for grains in steps versus not in steps show that steps lack a small particle friction angle tail that is present in the rest of the data (Fig. 3.13). Still, the mean particle friction angle does not appear to increase systematically with decreased jamming ratio (Fig. 3.14). This is because steps only occupy a small portion of the channel bed and the grains in the tread between these steps tend to have low particle friction angles, balancing the average. For example, the mean normalized friction angle of grains outside of steps at San Oline Creek (63.2°) and Tumble Creek (63.0°), two sites with high step cover, were lower than any of the mean friction angles measured across the entire sites. Arroyo Seco was exceptional in that normalized friction angles were high both in steps (78.9°) and outside of steps (70.1°), although the mean in steps was higher.

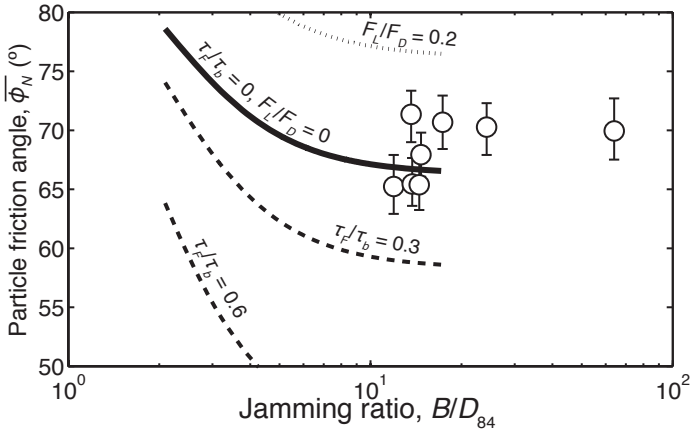

Figure 3.14: Mean friction angle as a function of jamming ratio. The solid line is the model prediction (equation (3.4)) for no morphologic form drag and no lift force, as inverted from available field data. The dashed lines are the contours with no lift force but increasing morphologic form drag. The dotted lines are the contours with no form drag but increasing lift force.

3.5 Discussion

3.5.1 Particle Friction Angle and Bed Organization

One possible explanation for the less pronounced trends between $\overline{\phi}/\overline{\phi_{D_{50}}}$ and D/D_{50} observed in Fig. 3.11 is that the reach-scale D_{50} is a poor predictor of the grain sizes immediately surrounding a sampled clast. This is certainly true in fluvially sorted beds where patches quickly develop (e.g., Nelson et al., 2010; Scheingross et al., 2013). Within an individual patch, a particular grain is more likely to be surrounded by grains of similar size rather than the reach D_{50} (Crowder et al., 1997). This should promote particle friction angles that are independent of grain size even when normalized by the reach D_{50}. While it is obvious that the D_{50} of the patch is the most appropriate length scale for comparison, characterizing grain size distributions over patches that are meter scale, as is common in low-order channels, is often not practicable for inferring reach-scale sediment transport rates.

The larger relative grain size dependence observed on steeper slopes (Fig. 3.11b) is likely due to the reduced fluvial reorganization of the sediment beds in these reaches, which all show stronger evidence for debris flow deposition of grains, and lack sorting (Fig. 3.6). Without substantial grain sorting, the reach D_{50} becomes more meaningful in describing the grains surrounding a sampled grain. For comparison, the previous study of in situ particle friction angles (Johnston et al., 1998) explicitly avoided portions of the channel bed that exhibited sorting or imbrication. Thus, the larger relative grain size dependence found at most sites of that study is consistent with our interpretation.

The effects of meter-scale bed organization also offer an explanation for the poor

correlation between the reach sorting parameter (equation (3.6)) and the mean particle friction angle (Table 3.2), contrary to previous work (Buffington et al., 1992; Johnston et al., 1998). It is likely that sorting at this smaller scale is partially responsible for the small differences in the mean particle friction angle between sites (Figs. 3.12 and 3.14), and the reach sorting parameter does not capture these effects.

3.5.2 Size-Selective Transport

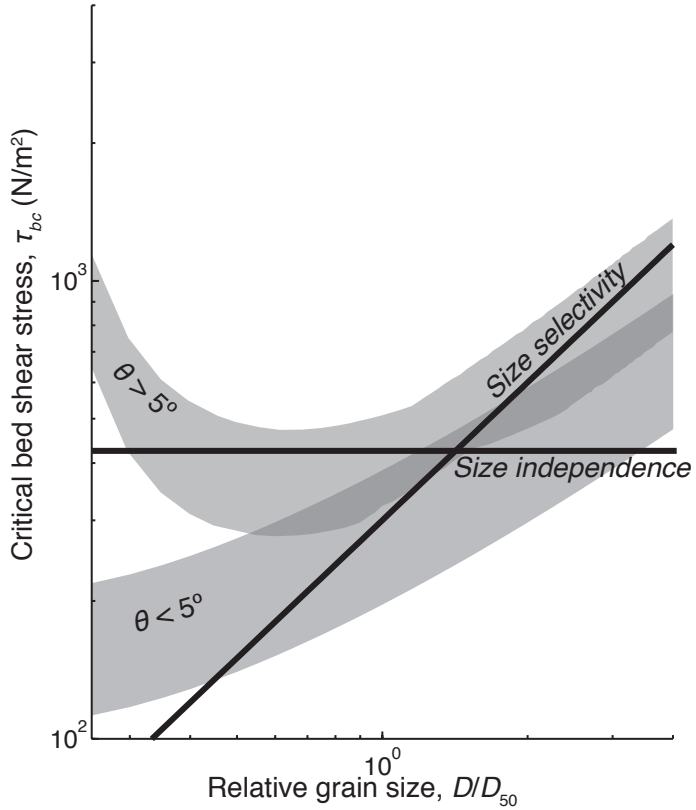

Figure 3.15: Model predictions for the critical basal shear stress required for a range of grain sizes at each site. The shaded regions indicate the distinct prediction envelopes for study sites with $\theta > 5°$ and $\theta < 5°$. The curves at each site were computed using equation (3.3); computed friction angle distributions (equation (3.2)); measured values of mean friction angle, channel slope, and grain size; and assumed values of $F_L/F_D = 0$ and $\tau_f/\tau_T = 0$.

Large sediment grains should require higher bed shear stresses for mobilization than smaller ones if weight alone was important. Several studies have shown, however, that this size selectivity is diminished due to reduced particle friction angles and increased protrusion into the flow for larger grains (Mao et al., 2008; Parker, 2008; Yager et al., 2012; Scheingross et al., 2013). This observation has led to the use of a "hiding function" to describe the degree of size selectivity in sediment transport (Parker, 1990):

$$\frac{\tau_{bc}}{\tau_{bc_{D50}}} = \left(\frac{D}{D_{50}}\right)^{1-\gamma} \tag{3.9}$$

where $\tau_{bc_{D50}}$ is the threshold bed shear stress to entrain the median grain size and γ is a nondimensional constant to describe how the threshold bed shear stress changes as a function of grain size. Note that $\gamma = 0$ indicates a linear correlation between sediment size and the threshold bed shear stress for entrainment and $\gamma = 1$ indicates that all grain sizes are mobile at the same bed shear stress ("size independence"). In a compilation of data from low-sloping channels, Parker (2008) suggests that channels are closer to size-independent transport, $\gamma = 0.79 \pm 0.16$ (standard deviation). Investigations in steep channels tend to report more size-selective values ranging from $\gamma = 0.51$ to 0.79 (Mao et al., 2008; Yager et al., 2012; Scheingross et al., 2013).

We can compare our grain size dependence on particle friction angle to these hiding functions by using the model of Lamb et al. (2008) and inputting measured slope, grain sizes, and friction angles for each channel. For simplicity, the friction angle for each D/D_{50} at each site is calculated as $\overline{\phi} = \overline{\phi_{D50}}\left(\frac{D}{D_{50}}\right)^{-\beta}$. The modeling suggests highly selective entrainment for the moderately sloping channels, $\gamma = 0.41$, and more peculiar

behavior for the steepest channels (Fig. 3.15). Within the steep channels examined here, the hiding effect is predicted to dominate for fine grains ($< D_{50}$), yielding reverse mobility, while coarse grains are predicted to exhibit highly size-selective transport. Some of the predicted size selectivity is the result of a strong dependence of the model on grain emergence from the flow surface in very steep channels (Lamb et al., 2008). However, the reduced grain size dependence in the particle friction angle appears to play an important role in size selectivity, particularly at the moderately steep slopes. These results help to reconcile the abundant observations of size-selective transport in mountain channels (e.g., D'Agostino et al., 1999; Lenzi et al., 2006b; Mao et al., 2008; Scheingross et al., 2013) with the theory that predicts that large grains should be as mobile as or even more mobile than small grains (e.g., Egiazaroff, 1965; Wiberg et al., 1987; Solari et al., 2000; Parker, 2008). This increase in size selectively ultimately renders the largest grains immobile and promotes extraction of momentum from the flow, increasing the bed shear stress required for mobilization and reducing sediment transport rates (Yager et al., 2007).

3.5.3 Sediment Mobility and Channel Bed Slope

Over the eight sites we studied, with bed angles ranging from $\theta = 0.5°$ to 23°, there was no trend between particle friction angle and bed slope (Fig. 3.12). To reject the hypothesis that the increased threshold Shields stress with increased slope is due to increased particle friction angles, corresponding measurements of the threshold Shields stress at our study sites would be ideal. In the absence of such data, however, we rely on previously established trends between threshold Shields stress and bed slope (e.g.,

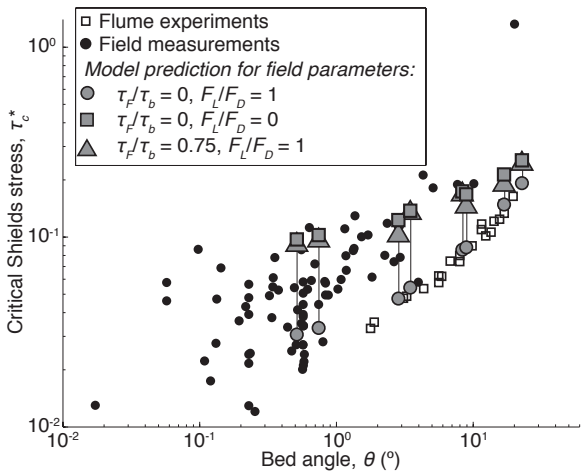

Figure 3.16: Computed critical Shields stress for the measured friction angles and respective slopes using equation (3.3) and various values of F_L/F_D and τ_F/τ_b. Field (Andrews, 1994; Montgomery et al., 1997; Andrews, 2000; Church et al., 2002; Whitaker et al., 2007; Mao et al., 2008; Scheingross et al., 2013) and flume (Prancevic et al., 2014) data from Fig. 3.2 are included for comparison.

Mueller, E R et al., 2005; Mao et al., 2008). The consistency of mean particle friction angles over the wide range in bed slopes tested here suggests that changes in grain stability, on average, are not driving the observed trend of threshold Shields stress in the field. Instead, this trend is likely caused by changes in hydraulics inherent to shallow flows (e.g., Lamb et al., 2008; Recking, 2009), with a secondary effect due to changes in stress lost to morphologic form drag (e.g., Wiberg et al., 1991; Millar, 1999; Nitsche et al., 2011; Ferguson, 2012; Yager et al., 2012; Scheingross et al., 2013). Because our data do not fall on any of the model contours in Fig. 3.12, a change in morphologic form drag or lift-to-drag ratio is required to recover the observed trend in threshold Shields stresses in the field data.

3.5.4 Sediment Mobility and Jamming Ratio

Comparing mean particle friction angles with B/D_{84} similarly shows no trend (Fig. 3.14). This result is consistent with the flume experiments of Zimmermann et al. (2010), which did not produce considerable jamming above $B/D_{84} >\sim 8$. Still we observed greater step occurrence in narrower channels (Fig. 3.8), and grains in these steps required twice the average normalized pulling strength ($\overline{F_p/W}$) to remove. Rather than stabilizing the entire channel bed, increased jamming ratio in our study sites promotes the stabilization of discrete steps. Once stabilized, these steps dramatically alter the hydraulics of the flow, increasing stress over the lip and into the plunge pool of the step and reducing stress over much of the lower-sloping step tread (Zimmermann et al., 2001). Thus, we suggest that particle friction angles inhibit sediment transport in narrow channels by increasing stability locally while focusing stress in the vicinity of the stable step.

3.5.5 Lift to Drag Ratios and Morphologic Form Drag

If the model predictions of particle friction angles based on observed threshold Shields stresses are correct, then this implies that lift-to-drag ratios and/or morphologic form drag must vary to reconcile the data sets (Figs. 3.12 and 3.14). There are infinite combinations of F_L/F_D and τ_F/τ_b that could potentially explain the available field data. Fig. (3.16) shows that by varying either parameter while holding the other constant, we can recover nearly the entire envelope of threshold Shields stresses observed in the field. In reality, both parameters are likely changing. The experiments of Schmeeckle et al. (2007) reveal considerable scatter in the lift force and do not support a generalized

ratio between lift and drag force. In addition, our own results support slope-dependent morphologic form drag through stabilization of coarse grains and steps preferentially on steep slopes. More work is needed to constrain the role of these two parameters in reducing sediment transport rates.

3.6 Conclusions

By directly measuring the force required to dislodge 275 sediment grains in eight streams of varying slope and width, we were able to assess the effect of these parameters on the particle friction angle. Interestingly, median grain sizes over all slopes in this study are, on average, more stable than previously recorded. This is likely due to the effects of particle interlocking that are necessarily ignored in tilt table measurements. In addition, friction angle measurements made in situ do not exhibit as pronounced a grain size dependence as those derived from tilt table experiments. This indicates that coarse grains are less easily mobilized than previously thought within our study sites. Increased grain stability was also observed in steps. Even so, the particle friction angle did not vary systematically with either slope or jamming ratio (above the critical value proposed by Zimmermann et al. (2010)), indicating that the threshold bed shear stress required to mobilize sediment at our study sites would not increase as a direct result of particle friction angles. Instead, an increase in threshold bed shear stress should result from changing hydraulics in steep channels, including an increase in momentum loss to immobile boulders and bed forms. It is also likely that the offset between the threshold bed shear stress for sediment mobilization in the laboratory versus the field is due to the heightened particle friction

angles in natural channels, although firm conclusions are hindered by a lack of theory for lift forces and morphologic form drag in shallow and steep flows. This work illustrates the importance of the heterogeneity of particle friction angles in natural channels, which can only be observed if measured in situ.

Notation

B	channel width
C_D	drag coefficient
D	length of intermediate grain axis
D_n	nth percentile grain diameter
F_D	drag force
F_L	lift force
F_N	normal force
F_P	pulling force
F_R	frictional force
g	gravitational acceleration
H	flow depth
u	local time-averaged velocity
u_*	shear velocity
V	grain volume
W	grain weight
z	bed-normal spatial coordinate
β	friction angle fit parameter
γ	critical shear stress fit parameter
δ	geometrical grain exposure factor
θ	bed angle
ρ	density of water
ρ_s	material density of sediment
σ	grain sorting parameter
σ_u	temporal standard deviation of flow velocity
τ_b	total bed shear stress
τ_{bc}	total bed shear stress at the onset of motion
$\tau_{bc_{D50}}$	total bed shear stress at the onset of motion of the median grain size
τ^*	Shields stress
τ_c^*	Shields stress at the onset of motion
τ_F	bed shear stress expended on immobile obstacles
ϕ	particle friction angle
$\phi_{D_{50}}$	friction angle of the median grain size ($2/3D_{50} \leq D < 3/2D_{50}$)
ϕ_N	grain-size-normalized particle friction angle

Acknowledgements

Preliminary measurements for this study were performed by Eric Kleinsasser. We would like to thank Brian Fuller, Luca Malatesta, Joel Scheingross, and Alison Piasecki for their help with field measurements. Field data and calculated friction angles can be found in the supporting information. Funding for this work was provided by NSF grants EAR-0922199 and EAR-1349115, the Terrestrial Hazards Observation and Reporting center at Caltech, and the Keck Institute for Space Studies. We thank Michael Church, Mark Schmeeckle, and an anonymous reviewer for their insightful reviews that improved this paper.

3.7 References

Aberle, J and G M Smart (2003). "The influence of roughness structure on flow resistance on steep slopes." In: *Journal of Hydraulic Research* 41.3, pp. 259–269.

Andrews, Edmund D (1994). "Marginal bed load transport in a gravel bed stream, Sagehen Creek, California." In: *Water Resources Research* 30.7, pp. 2241–2250.

— (2000). "Bed material transport in the Virgin River, Utah." In: *Water Resources Research* 36.2, pp. 585–596.

Ashida, K and M Bayazit (1973). "Initiation of motion and roughness of flows in steep channels." In: *Hydraul Res, Proc 15th Congress, Istanbul, Turkey* 1, pp. 475–484.

Bartnick, W (1991). "Determination of the critical conditions of incipient motion of bed load in mountain rivers." In: *Fluvial Hyraulics in Mountain Regions*. Ed. by Aronne Armanini and G Di Silvio. Springer-Verlag, Berlin, pp. 83–88.

Bathurst, J C, H H Cao, and W H Graf (1984). *Hydraulics and sediment transport in a steep flume: Data from the EPFL study*. Tech. rep. Wallingford, U.K.

Brummer, CJ and DR Montgomery (2003). "Downstream coarsening in headwater channels." In: *Water Resources Research* 39.10, p. 1294.

Buffington, John M, William E Dietrich, and James W Kirchner (1992). "Friction angle measurements on a naturally formed gravel streambed: Implications for critical boundary shear stress." In: *Water Resources Research* 28.2, pp. 411–425.

Bunte, Kristin and Steven R Abt (2001). *Sampling surface and subsurface particle-size distributions in wadable gravel-and cobble-bed streams for analyses in sediment transport, hydraulics, and streambed monitoring*. Tech. rep. RMRS-GTR-74.

Carollo, F, V Ferro, and D Termini (2005). "Analyzing turbulence intensity in gravel bed channels." In: *Journal of Hydraulic Engineering* 131.12, pp. 1050–1061.

Church, Michael, Marwan A Hassan, and John F Wolcott (1998). "Stabilizing self-organized structures in gravel-bed stream channels: Field and experimental observations." In: *Water Resources Research* 34.11, pp. 3169–3179.

Church, Michael and Marwan A Hassan (2002). "Mobility of bed material in Harris Creek." In: *Water Resources Research* 38.11, pp. 19–1–19–12.

Coulombe-Pontbriand, M and Michel Lapointe (2004). "Landscape controls on boulder-rich, winter habitat availability and their effects on Atlantic salmon (Salmo salar) parr abundance in two fifth-order mountain streams." In: *Canadian Journal of Fisheries and Aquatic Sciences* 61.4, pp. 648–658.

Crowder, David W and Panayiotis Diplas (1997). "Sampling heterogeneous deposits in gravel-bed streams." In: *Journal of Hydraulic Engineering* 123.12, pp. 1106–1117.

D'Agostino, Vincenzo and Mario A Lenzi (1999). "Bedload transport in the instrumented catchment of the Rio Cordon." In: *Catena* 36.3, pp. 191–204.

Downes, Barbara J, Alena Glaister, and P S Lake (1997). "Spatial variation in the force required to initiate rock movement in 4 upland streams: Implications for estimating disturbance frequencies." In: *Journal of the North American Benthological Society*, pp. 203–220.

Egiazaroff, I V (1965). "Calculation of nonuniform sediment concentrations." In: *J Hydraul Div Am Soc Civ Eng* 91.4, pp. 225–247.

Fenton, J D and J E Abbott (1977). "Initial movement of grains on a stream bed: The effect of relative protrusion." In: *Proceedings of the Royal Society of London. A. Mathematical and Physical Sciences* 352.1671, pp. 523–537.

Ferguson, Robert I (2012). "River channel slope, flow resistance, and gravel entrainment thresholds." In: *Water Resources Research* 48.

Gilbert, G K (1914). "The transportation of debris by running water." In: *US Geol. Surv. Prof Pap* 86, p. 263.

Graf, W H and L Suszka (1987). "Sediment transport in steep channels." In: *J. HydroSci. Hydraul. Eng.* 5.1, pp. 11–26.

Gregoretti, C (2008). "Inception sediment transport relationships at high slopes." In: *Journal of Hydraulic Engineering* 134.11, pp. 1620–1629.

Inman, Douglas L (1952). "Measures for describing the size distribution of sediments." In: *Journal of Sedimentary Research* 22.3.

Johnston, Christopher E, Edmund D Andrews, and John Pitlick (1998). "In situ determination of particle friction angles of fluvial gravels." In: *Water Resources Research* 34.8, pp. 2017–2030.

Kirchner, J W et al. (1990). "The variability of critical shear stress, friction angle, and grain protrusion in waterworked sediments." In: *Sedimentology* 37, pp. 647–672.

Kostaschuk, Ray, Paul Villard, and Jim Best (2004). "Measuring velocity and shear stress over dunes with acoustic Doppler profiler." In: *Journal of Hydraulic Engineering* 130.9, pp. 932–936.

Lamb, Michael P, William E Dietrich, and Jeremy G Venditti (2008). "Is the critical Shields stress for incipient sediment motion dependent on channel-bed slope?" In: *Journal Of Geophysical Research-Earth Surface* 113.F2, F02008.

Laronne, J B (1973). "A geomorphological approach to coarse bed-material movement in alluvial channels, with special reference to a small appalachian stream." PhD thesis. Montreal, QC: McGill University.

Lenzi, M A, L Mao, and F Comiti (2006a). "Effective discharge for sediment transport in a mountain river: Computational approaches and geomorphic effectiveness." In: *Journal of Hydrology* 326.1-4, pp. 257–276.

— (2006b). "When does bedload transport begin in steep boulderbed streams?" In: *Hydrological Processes* 20, pp. 3517–3533.

Li, Zhenlin and Paul D Komar (1986). "Laboratory measurements of pivoting angles for applications to selective entrainment of gravel in a current." In: *Sedimentology* 33.3, pp. 413–423.

Major, Jon J (1997). "Depositional processes in large-scale debris-flow experiments." In: *The Journal of Geology* 105.3, pp. 345–366.

Mao, Luca et al. (2008). "Field based analysis of sediment entrainment in two high gradient streams located in Alpine and Andine environments." In: *Geomorphology* 93.3, pp. 368–383.

Meyer-Peter, E and R Mueller (1948). "Formulas for bed-load transport." In: *Proc. 2nd Congr. Int. Assoc. Hydraul. Res., Stockholm*, pp. 39–64.

Millar, Robert G (1999). "Grain and form resistance in gravel-bed rivers." In: *Journal of Hydraulic Research* 37.3, pp. 303–312.

Miller, Robert L and Robert J Byrne (1966). "The angle of repose for a single grain on a fixed rough bed." In: *Sedimentology* 6.4, pp. 303–314.

Montgomery, DR and JM Buffington (1997). "Channel-reach morphology in mountain drainage basins." In: *Geological Society of America Bulletin* 109.5, pp. 596–611.

Mueller, E N et al. (2008). "Modeling bed-load rates from fine grain-size patches during small floods in a gravel-bed river." In: *Journal of Hydraulic Engineering* 134.10, pp. 1430–1439.

Mueller, E R, J Pitlick, and J M Nelson (2005). "Variation in the reference Shields stress for bed load transport in gravel-bed streams and rivers." In: *Water Resources Research* 41.4, W04006.

Nelson, Peter A, William E Dietrich, and Jeremy G Venditti (2010). "Bed topography and the development of forced bed surface patches." In: *Journal of Geophysical Research* 115.F4, F04024.

Nikora, Vladimir et al. (2001). "Spatially averaged open-channel flow over rough bed." In: *Journal of Hydraulic Engineering* 127.2, pp. 123–133.

Nitsche, Manuel et al. (2011). "Evaluation of bedload transport predictions using flow resistance equations to account for macro-roughness in steep mountain streams." In: *Water Resources Research* 47.8, W08513.

Olivero, M (1984). "Movimiento incipiente de partículas en flujo torrencial." In: *Special Report: University of Los Andes, Meridad, Venezuela*, pp. 1–169.

Parker, G (1990). "Surface-based bedload transport relation for gravel rivers." In: *Journal of Hydraulic Research* 28.4, pp. 417–436.

Parker, Gary (2008). "Transport of Gravel and Sediment Mixtures." In: *American Society of Civil Engineering Manual*. Reston, VA: American Society of Civil Engineers, pp. 165–251.

Picon, G A (1991). "Estudio experimental de transporte sedimentos en rios de montaña." PhD thesis. Merida, Venezuela: Universidad de Los Andes.

Prancevic, J P, M P Lamb, and B M Fuller (2014). "Incipient sediment motion across the river to debris-flow transition." In: *Geology* 42, pp. 191–194.

Recking, A (2009). "Theoretical development on the effects of changing flow hydraulics on incipient bed load motion." In: *Water Resources Research* 45, W04401.

Rickenmann, D (1997). "Sediment transport in Swiss torrents." In: *Earth Surface Processes and Landforms* 22, pp. 937–951.

Rickenmann, Dieter (2012). "Alluvial steep channels: Flow resistance, bedload transport prediction, and transition to debris flows." In: *GravelBed Rivers*. Chichester, UK: John Wiley & Sons, Ltd, pp. 386–397.

Sanguinito, Sean and Joel Johnson (2011). "Quantifying gravel overlap and dislodgement forces on natural river bars: implications for particle entrainment." In: *Earth Surface Processes and Landforms* 37.1, pp. 134–141.

Scheingross, Joel S et al. (2013). "Influence of bed patchiness, slope, grain hiding, and form drag on gravel mobilization in very steep streams." In: *Journal Of Geophysical Research-Earth Surface* 118, pp. 1–20.

Schmeeckle, Mark W and Jonathan M Nelson (2003). "Direct numerical simulation of bedload transport using a local, dynamic boundary condition." In: *Sedimentology* 50.2, pp. 279–301.

Schmeeckle, Mark W, Jonathan M Nelson, and Ronald L Shreve (2007). "Forces on stationary particles in nearbed turbulent flows." In: *Journal of Geophysical Research: Solid Earth (1978–2012)* 112.F2.

Shields, A (1936). "Anwendung der Ähnlichkeitsmechanik und der Turbulenzforschung auf die Geschiebebewegung." In: *Mitt. Preuss Versuchsanst. Wasserbau Schiffbau* 26.

Shvidchenko, A B and G Pender (2000). "Flume study of the effect of relative depth on the incipient motion of coarse uniform sediments." In: *Water Resources Research* 36.2, pp. 619–628.

Sklar, Leonard S and William E Dietrich (2004). "A mechanistic model for river incision into bedrock by saltating bed load." In: *Water Resources Research* 40.6.

Smith, J Dungan and S R Mclean (1977). "Spatially averaged flow over a wavy surface." In: *Journal of Geophysical Research: Solid Earth (1978–2012)* 82.12, pp. 1735–1746.

Solari, Luca and Gary Parker (2000). "The curious case of mobility reversal in sediment mixtures." In: *Journal of Hydraulic Engineering* 126.3, pp. 185–197.

Stock, Jonathan D and William E Dietrich (2006). "Erosion of steepland valleys by debris flows." In: *Geological Society of America Bulletin* 118.9-10, pp. 1125–1148.

Torri, D and J Poesen (1988). "Incipient motion conditions for single rock fragments in simulated rill flow." In: *Earth Surface Processes and Landforms* 13.3, pp. 225–237.

Whitaker, Andrew C and Donald F Potts (2007). "Analysis of flow competence in an alluvial gravel bed stream, Dupuyer Creek, Montana." In: *Water Resources Research* 43.7.

Wiberg, Patricia L and Jim Dungan Smith (1987). "Calculations of the Critical Shear Stress for Motion of Uniform and Heterogeneous Sediments." In: *Water Resources Research* 23.8, pp. 1471–1480.

Wiberg, Patricia L and J Dungan Smith (1991). "Velocity distribution and bed roughness in highgradient streams." In: *Water Resources Research* 27.5, pp. 825–838.

Yager, E M, J W Kirchner, and W E Dietrich (2007). "Calculating bed load transport in steep boulder bed channels." In: *Water Resources Research* 43.7, W07418.

Yager, E M et al. (2012). "Prediction of sediment transport in step-pool channels." In: *Water Resources Research* 48.W01541.

Zimmermann, A and M Church (2001). "Channel morphology, gradient profiles and bed stresses during flood in a step-pool channel." In: *Geomorphology* 40, pp. 311–327.

Zimmermann, André (2010). "Flow resistance in steep streams: An experimental study." In: *Water Resources Research* 46.9, W09536.

Zimmermann, André, Michael Church, and Marwan A Hassan (2010). "Step-pool stability: Testing the jammed state hypothesis." In: *Journal Of Geophysical Research-Earth Surface* 115, F02008.

Chapter 4

Experimental tests of seepage-induced slope failure and landslide size

Abstract

The stability of inclined, unconsolidated sediments subjected to groundwater flow on hillslopes and steep channel beds is important for both landscape evolution and natural hazards. Force-balance models, beginning with those developed by Taylor (1948), have been used for seven decades to predict the stability of slopes to landsliding, but they generally underpredict the degree of saturation required to destabilize sediment. Researchers often appeal to heightened stabilizing forces from root and mineral cohesion, and friction acting on the margins of the failure to explain this underprediction. Surprisingly, infinite-slope stability models in their simplest form have never been tested under con-

trolled laboratory conditions. To address this gap in data, we perform a set of controlled laboratory experiments with slope-parallel seepage in the simplest possible configuration. We performed 47 experiments in a 5 m laboratory flume with 4 grain sizes (D_{50} = 0.7, 2, 5, and 15 mm) and a wide range in bed angles ($\theta = 20°$ to 43°), spanning both Darcian and turbulent subsurface flow regimes. Our experiments show that granular slopes were more stable than predicted by Taylor force balance models in experiments that lack root or mineral cohesion for all grain sizes. Despite the smooth plastic walls of our flume and a long experimental test section, we found that wall and toe friction substantially enhanced bed stability, and including these stresses in the model led to more accurate predictions. Experimental landslides did not span the entire length of the flume, and instead short failures were favored with a characteristic aspect ratio of $L/W \approx 2$, consistent with field observations. Our experiments also show that the initial depth of failure increases on steeper slopes and is set by a competition between relative saturation level and wall stress, both of which increase with deeper failure planes. These results provide a validation of slope stability models for application to landslide prediction, and provide a basis for estimating failure geometries.

4.1 Introduction

Mass failure of inclined sediments experiencing subsurface flow produce landslides and debris flows that drive landscape evolution (e.g., Stock et al., 2006) and pose a significant hazard to human life and infrastructure (e.g., USGS, 2005; Petley, 2012). Shallow landslides can occur wherever steep deposits of unconsolidated sediment experience suf-

ficient downslope seepage stress and buoyant forces to become unstable (Taylor, 1948; Haefeli, 1948; Skempton et al., 1957; Lambe et al., 1969; Takahashi, 1978; Iverson et al., 1986). Consequently, these events are common on both soil-mantled hillslopes (e.g, Iverson et al., 1997) and (partially-)alluviated channel beds (e.g., Rickenmann et al., 1993; Prancevic et al., 2014). Once destabilized, landslides can move a short distance before depositing locally or runout downstream as erosive debris flows (e.g, Iverson et al., 1997; Stock et al., 2006). Regardless of initiation location or runout behavior, the physical processes driving initial failure are the same, with the exception that root cohesion is common on vegetated hillslopes and usually absent in channel beds. To predict the occurrence of these events, one-dimensional force-balance models have provided a physical basis for understanding the amount of water needed to destabilize soil of a given bulk friction angle, inclination angle, density, and porosity Taylor (1948), Haefeli (1948), and Lambe et al. (1969). Despite the importance of seepage-induced mass failure of sediments and the widespread application of these slope stability models in both engineering and geomorphology, the most basic version of the model has not been verified with controlled observations.

There are four primary forces typically considered in infinite slope (1-D) stability analyses: 1) the buoyant weight of sediment under the force of gravity; 2) frictional resistance at the basal and lateral failure planes; 3) seepage stress exerted on sediment grains by water flowing through the subsurface; 4) and cohesion due to root strength, electrostatic forces, or cementation, if applicable. Aside from cohesion (4), which is difficult to adequately measure (e.g., Waldron et al., 1981; Schmidt et al., 2001), prediction of the remaining forces (1-3) is relatively tractable, enabling the development of sim-

ple momentum-balance models over the past seven decades (Taylor, 1948; Haefeli, 1948; Skempton et al., 1957; Lambe et al., 1969; Iverson et al., 1986). The simplest formulation of this momentum balance casts these forces into a one-dimensional model that assumes homogenous conditions (slope, subsurface discharge, soil properties, and soil thickness) infinitely in the cross-slope and along-slope directions. This assumption is never satisfied but may serve as an acceptable approximation when soil thickness is thin relative to the downslope length and cross-slope width.

Independent observations of the hydrologic conditions at the time of slope failures are rare, but where available they have shown that the infinite slope stability model is a poor predictor of slope failure (Montgomery et al., 1994; Berti et al., 2005; Montgomery et al., 2009; Prancevic et al., 2014). In many recorded cases, sediment is observed to be more stable than predicted by slope stability models. For example, in a monitoring effort of a natural slope failure, Montgomery et al. (2009) found that the typical formulation for infinite slope stability predicted failure to occur in a completely unsaturated state, even when a soil cohesion term was included. In order to make the prediction match the observed conditions at failure, the tensile strength of all roots penetrating the slide sidewalls were added to the slope strength. In their examination of debris-flow initiation by failure of a channel bed, Berti et al. (2005) found that the infinite slope stability relationship for surface failures (Takahashi, 1978) under-predicted the flow discharge required to initiate their observed bed failures by an order of magnitude. Because this bed failure took place within a channel bed, soil cohesion and root strength are unlikely to account for such a discrepancy. However, this channel bed contained sufficiently coarse sediment such that the subsurface flow may have not have been Darcian, which is an

explicit prerequisite stated in several derivations of the infinite slope stability model (e.g., Bear, 1972; Iverson et al., 1986). Iverson et al. (1986) have also shown theoretically that infinite slope stability predictions are erroneous if groundwater seepage vectors are not oriented parallel to the bed, but these seepage vectors are difficult to measure in a natural channel bed. Enhanced stability relative to the infinite slope model has also been observed at the landscape scale, where the density of landslide occurrence is consistently much lower than the predicted portion of the landscape predicted to be unstable (Montgomery et al., 1994; Stock et al., 2011).

On slopes that are not sufficiently wide or long, additional resisting stresses acting on the margins of the landslide must be taken into consideration. Although these stresses are generally ignored, several studies have suggested that marginal stresses should play a crucial role in the stability of hillslopes (Burroughs, 1984; Dietrich et al., 2007; Montgomery et al., 2009; Milledge et al., 2014). Not only do these stresses exert some control on the stability of a hillslope, several studies have shown theoretically that stresses at the margins of the failure play a substantial role in determining both the depth and areal extent of the initial failure (Dietrich et al., 2007; Milledge et al., 2014). By setting the initial size of failures, marginal stresses might be critically important in determining landslide risk and geomorphic impact. In order to assess the validity of these predictions versus simpler, more commonly applied infinite slope models, we require controlled observations of slope stability, granular, and hydrologic conditions in the absence of other confounding factors.

Laboratory flume experiments provide a controlled setting to test slope stability models, but few have been performed. In some of these experiments, landslides have been

initiated by exfiltrating water from a cut-slope geometry and cannot provide a test of the infinite slope model (Eckersley, 1990; Wang et al., 2003). In other experiments, researchers have rained on laboratory hillslopes for the purposes of measuring pore pressure responses during the onset of failure (Moriwaki, 1993; Yagi et al., 1987; Reid et al., 1997; Iverson et al., 2000; Okura et al., 2002; Wang et al., 2003; Moriwaki et al., 2004). These studies are useful for understanding how flows are fluidized once ruptured, but the overhead application of rainfall complicates the comparison against the infinite slope stability model. Specifically, the discharge and saturation level increases with distance downslope and surface infiltration introduces a bed-normal seepage component, both of which violate key assumptions in the infinite slope model. Many of these studies also don't report the necessary soil characteristics and/or flow depth with respect to the bed surface.

In another study, Prancevic et al. (2014) observed heightened bed stability in a laboratory flume that lacked cohesion, roots, or stabilizing seepage vectors. However, this study was limited to relatively low-sloping experiments ($\theta \leq 33.0°$) that utilized only coarse-grained sediment ($D_{50} = 15$ mm). In these experiments, the bed destabilized only when surface flow was present, resulting in shallow failures of a limited number of grains. Dry measurements of the particle friction angle indicated that these small failures were more stable than larger failures. When a heightened particle friction angle was applied to the infinite slope stability model it matched the experimental data. It is also possible, however, that the increased stability was again due to coarse grain sizes ($D_{50} = 15$ mm) and the observed non-Darcian flow conditions (Prancevic et al., 2014). Consequently, these experiments were unable to determine the relative role of increased frictional re-

sistance and reduced seepage stress due to turbulence in enhancing the stability of the sediment bed.

In this study we perform a new series of laboratory flume experiments with a range of bed slopes, grain sizes, and bed thicknesses to test the infinite slope stability model, and assess potential stabilizing mechanisms. We conduct five sets of experiments with each set corresponding to a particular grain size and bed thickness. Each set is conducted over a wide range of bed slopes. Grain size is varied in order to test for the effect of turbulence in reducing subsurface flow velocities and stabilizing the bed. We compare the results of these experiments to an infinite slope stability model and to a model that considers frictional stresses at the margins of the failures.

4.2 Model for slope stability

4.2.1 Infinite-slope stability model

The original one-dimensional slope-stability models, proposed first by Taylor (1948) and Haefeli (1948), have served as the basis for subsequent models that incorporate a variety of effects from cohesion, wall friction (e.g., Lambe et al., 1969), non-parrallel seepage vectors (Iverson et al., 1986), partially saturated flow conditions (Lu et al., 2008), etc. The model begins with a Mohr-Coulomb failure criteria:

$$\tau = \sigma \tan \phi_b \tag{4.1}$$

where τ is shear stress acting on the failure plane, σ is the normal stress acting on the failure plane, and ϕ_b is the friction angle of the failure plane. Two alterative parameterizations of τ and σ have been proposed: one that considers the Coulomb friction of only the solid phase with buoyant and seepage forces acting on that solid phase, and another that considers the Coulomb friction model of the wet bulk material with basal pore pressure (u) reducing the effective normal stress, (i.e., $\overline{\sigma} = \sigma - u$). These two formulations have previously been shown to be equivalent (e.g., Lambe et al., 1969).

Here, we detail the Mohr-Coulomb stress balance in the parameterization that considers seepage and buoyant forces acting only on the solid phase. In this one-dimensional model, a soil layer of thickness Z is saturated to an arbitrary depth of flow, H, measured in the bed-normal direction relative to the sediment-bedrock interface (Fig. 4.1). The inclination angle, θ, is assumed to be the same for the bedrock, soil, and water surfaces and seepage is directed parallel to these surfaces. If the driving shear stresses are higher than the resisting stresses for some portion of the bed, then that portion of the bed is predicted to fail and slide downslope. The failure plane is defined as the surface where the driving stresses are exactly equal to the resisting stresses at some distance from the bed, z_f. Consequently, it is useful to define a water-flow thickness, $h = H - z_f$, and failure thickness, $z_t = Z - z_f$, measured relative to the failure plane (Fig. 4.1).

On slopes that are sufficiently steep, it is expected that failure will occur under subsaturated conditions (i.e., $h_c < z_t$). To solve for the conditions at failure, the unit buoyant weight of a partially saturated granular column can be defined as:

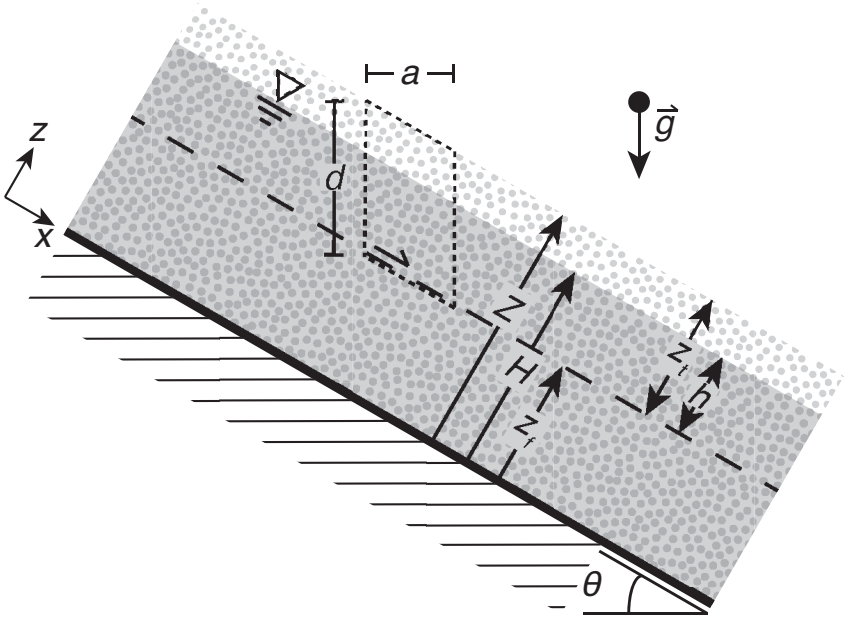

Figure 4.1: Schematic of an infinitely long and wide granular slope with subsurface seepage flow. The dashed line indicates the failure plane in the sediment bed, above which the stresses pulling the sediment downslope have overcome the frictional resisting stresses acting at the margins of the failure. This bed is assumed to extend infinitely in the along-slope and cross-slope (normal to the page) directions.

$$\gamma_{b,sub} = \frac{1}{z_t}\left[\underbrace{\int_{z=z_f}^{Z} \rho_s(1-\eta)g dz}_{\text{grain weight}} - \underbrace{\int_{z=zf}^{H} \rho_f(1-\eta)g dz}_{\text{buoyant force}}\right] \tag{4.2}$$
$$= (\rho_s - \rho_f \frac{h}{z_t})(1-\eta)g$$

where g is gravitational acceleration, ρ_s is the material density of the sediment grains, ρ_f is the fluid material density, and η is the characteristic porosity. Similarly the average unit weight of the pore water is defined as the density of water multiplied by gravitational acceleration and the saturation level of the bed:

$$\gamma_f = \frac{h}{z_t}\rho_f g \tag{4.3}$$

Following Lambe et al. (1969, Fig. 24.5), we can use the buoyant unit weight of the soil to compute the normal force that control volume ad exerts on the failure plane as (Fig. 4.1):

$$\overline{N} = \gamma_{b,sub} ad \cos\theta \tag{4.4}$$

The shear force exerted by control volume ad on the failure plane is composed of the downslope component of the buoyant unit weight of the soil, and also the seepage stress exerted by the fluid on the grains:

$$T = \underbrace{\gamma_{b,sub} ad \sin\theta}_{\text{buoyant weight}} + \underbrace{\gamma_f ad \sin\theta}_{\text{seepage stress}} \tag{4.5}$$

We assume here that the direction of seepage is directed exactly downslope and that the fluid is not accelerating. When these conditions are satisfied the downslope seepage stress balances the gravitational hydraulic gradient of the pore fluid. We make no explicit assumption here that the seepage flow must be Darcian, although this requirement has been specified in previous derivations of eq. (4.5) (Bear, 1972; Iverson et al., 1986).

Failure is predicted to occur when the control volume satisfies the Mohr-Coloumb failure criteria, i.e.:

$$\frac{T}{\overline{N}} = \tan\phi_b \tag{4.6}$$

where ϕ_b is the bulk friction angle for the dry granular material. Substituting eqs. (4.4) and (4.5) into eq. (4.6) yields:

$$\frac{h_c}{z_t} = \frac{\rho_s}{\rho_f} \frac{\frac{\tan\phi_b}{\tan\theta} - 1}{\frac{\eta}{1-\eta} + \frac{\tan\phi_b}{\tan\theta}} \tag{4.7}$$

In addition to Lambe et al. (1969), eq. (4.7) is the critical saturation predicted to produce failure in all previous derivations of infinite slope stability (Taylor, 1948; Haefeli, 1948; Skempton et al., 1957; Iverson et al., 1986). Despite being derived in numerous texts and ubiquitously applied, eq. (4.7) has never been experimentally verified in its simplest form.

4.2.1.1 Supersaturated failure conditions

On slopes that are sufficiently shallow, eq. (4.7) will yield a critical flow depth that is predicted to be greater than the soil thickness $\left(\frac{h_c}{z_t} \geq 1\right)$ and eq. (4.7) is no longer applicable. Note that there is no change to eq. (4.3) for calculating the seepage stress and h/z is permitted to exceed 1 in order to account for the dilute surface flow over the bed surface. However, eq. (4.2) must be modified to limit the magnitude of the buoyant force acting on the grains within the supersaturated regime:

$$\gamma_{b,surf} = (\rho_s - \rho_f)(1-\eta)g \tag{4.8}$$

This new buoyant grain weight can then be applied in eq. (4.6) for a super-saturated prediction for the critical flow depth:

$$\frac{h_c}{z_t} = \frac{\rho_s - \rho_f}{\rho_f}(1-\eta)\left(\frac{\tan\phi_b}{\tan\theta} - 1\right) \tag{4.9}$$

which is the equation first derived by Takahashi (1978), and subsequently used by Prancevic et al. (2014) to calculate the flow depth required to predict failures in the supersaturated regime.

4.2.1.2 Failure thickness

Failure thickness, z_t, is not explicitly defined in eqs. (4.7) and (4.9), but can be predicted by the calculated stress distributions with depth. For the subsaturated regime, the weakest failure plane is expected to be the deepest one possible ($z_t = Z$) (Takahashi, 1978). For the case of sub-saturated failure ($H_c < Z$), the deepest failure plane always experiences the highest saturation level (i.e., the maximum value of h_c/z_t is H_c/Z). On the contrary, for the case of supersaturated flow ($H_c > Z$), dilute surface flow concentrates stress at the surface of the bed and the preferred failure plane is expected to abruptly shift to the shallowest possible failure plane, which is equal to the thickness of a single grain ($z_t = D_{50}$) (Takahashi, 1978; Prancevic et al., 2014).

4.2.2 Stability with wall and toe stresses

When a slope is not infinitely wide or long, then some of the frictional resistance to failure is borne by the lateral and downslope margins of the failure plane (e.g., Lambe et al., 1969; Montgomery et al., 2009; Milledge et al., 2014; Bellugi et al., 2015). At the lateral margins, the sides of the mobile slab must slide against the walls of the failure scarp. For a failure that is finite in length, the failure plane must eventually return to the soil surface at the toe of the failure. The simplest finite failure-plane geometry is a soil wedge to be displaced at the toe of the upslope slab (Fig. 4.2). This wedge exerts resisting stresses

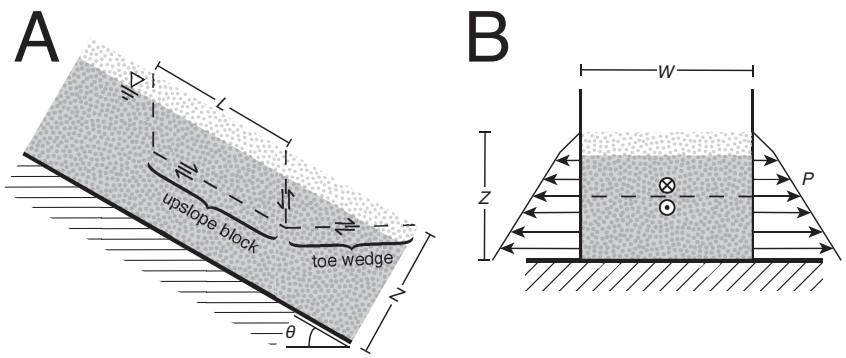

Figure 4.2: Schematic of a finite granular slope with subsurface seepage flow with A) a cross-slope perspective, similar to Fig. (4.1) and B) an along-slope perspective looking in the down-slope direction. The dashed line in both panels indicates the failure plane in the sediment bed, above which the stresses pulling the sediment downslope have overcome the frictional resisting stresses acting at the margins of the failure. This failure is broken into two masses: the upslope block that has an initial direction of motion that is directly downslope, and the toe wedge that has a component of motion that is towards the surface of the sediment bed. Note that this difference in initial trajectories results in some friction at the interface between the two masses.

in the form of friction along the base of the wedge (on the failure plane) and friction between the wedge and the upslope slab, which are mobilized with different trajectories. In order to overcome these additional resisting stresses an increased saturation level is required to initiate failure.

Following Lambe et al. (1969), the depth-integrated wall and toe resistance in subsaturated conditions $\left(\frac{h_c}{z_t} \leq 1\right)$ can be estimated using the following respective relationships:

$$\tau_{w,sub} = \frac{1}{2} K_w z_t \left(\rho_s - \frac{h^2}{z_t^2}\rho_f\right)(1-\eta) g \tan\phi_w \tag{4.10}$$

$$\tau_{t,sub} = \frac{1}{2} K_t z_t \left(\rho_s - \frac{h^2}{z_t^2}\rho_f\right)(1-\eta) g \tan\phi_b \tag{4.11}$$

where $\tan\phi_w$ is the frictional coefficient between the bulk sediment grains and flume walls, and K_w and K_t are the coefficients relating the weight of overbearing sediment to the earth pressure exerted on the walls and toe, respectively. The most commonly used

earth pressure coefficient for wall stress is based on an empirical study by Jaky ("The coefficient of earth pressure at rest. (in Hungarian)"):

$$K_w = (1 - \sin\phi_b) \tag{4.12}$$

Several theoretical formulations of the toe (or "passive") earth pressure coefficient have been proposed. These earth pressure coefficients vary in the assumed behavior and shape of the wedge of sediment at the toe that must be displaced in order for the upslope block to translate downslope (see discussion in Milledge et al., 2014). For this study, we employ the Coulomb passive earth pressure coefficient because it accounts for the frictional force acting between the toe wedge and the upslope block in the form of the explicit relationship:

$$K_t = \cos\phi_b \left(1 - \left(\frac{\sin(2\phi_b)\sin(\phi_b + \theta)}{\cos\phi_b \cos\theta}\right)^{0.5}\right)^{-2} \tag{4.13}$$

The wall and toe stresses are acting over different areas than the basal stresses defined in eqs. (4.4) and (4.5), and in order to combine all stresses into the Mohr-Coulomb stress balance (eq. 4.1), the stresses must be integrated and normalized over their relevant surface areas. Multiplying the stresses by their relevant surface areas, adding the toe and wall stress terms to eq. (4.1), and normalizing by LWz_t yields the following Mohr-Coulomb force balance:

$$\underbrace{\gamma_b \sin\theta}_{\text{buoyant grain weight}} + \underbrace{\gamma_f \sin\theta}_{\text{seepage weight}} = \underbrace{\gamma_b \cos\theta \tan\phi_b}_{\text{basal friction}} + \underbrace{2\frac{\tau_{w,sub}}{W}}_{\text{wall friction}} + \underbrace{\frac{\tau_{t,sub}}{L}}_{\text{toe friction}} \tag{4.14}$$

We now substitute the relevant expressions for γ_b, γ_f, $\tau_{w,sub}$, and $\tau_{t,sub}$ into eq. (4.14) to calculate the critical flow depth. The resulting equation can be rearranged as:

$$0 = \left(\frac{h_c}{z_t}\right)^2 \left(\frac{z_t}{W}\tan\phi_w K_w + \frac{z_t}{2L}\tan\phi_b K_t\right) + \frac{h_c}{z_t}\left(\frac{\eta}{1-\eta}\sin\theta + \cos\theta\tan\phi_b\right) + \frac{\rho_s}{\rho_f}\left[\sin\theta - \cos\theta\tan\phi_b - \frac{z_t}{W}\tan\phi_w K_w - \frac{z_t}{2L}\tan\phi_b K_t\right) \tag{4.15}$$

Equation (4.15) is quadratic in terms of $\frac{h_c}{z_t}$. Before solving for $\frac{h_c}{z_t}$, it is useful to introduce some substitutions for terms that do not depend on h_c or z_t:

$$K_c = \tan\phi_w K_w + \frac{W}{2L}\tan\phi_b K_t \tag{4.16}$$

$$K_A = \sin\theta - \cos\theta\tan\phi_b \tag{4.17}$$

$$K_N = \frac{\eta}{1-\eta}\sin\theta + \cos\theta\tan\phi_b \tag{4.18}$$

With these substitutions, solving for $\frac{h_c}{z_t}$ yields:

$$\frac{h_c}{z_t} = \frac{-K_N + \left[K_N^2 - 4\frac{\rho_s}{\rho_f}\frac{z_t}{W}K_c\left(K_A - \frac{z_t}{W}K_c\right)\right]^{1/2}}{2\frac{z_t}{W}K_c} \tag{4.19}$$

Inspection of eq. (4.19) reveals that the critical saturation for failure $\left(\frac{h_c}{z_t}\right)$ decreases as the width, W, and length, L, of the failure increase. This suggests that larger failures should be less stable than smaller ones because the proportion of frictional resistance exerted by the margins is smaller.

4.2.2.1 Supersaturated failure model with wall and toe stresses

Wall and toe stresses in the supersaturated regime are expected to be considerably smaller due to the relatively thin failure thicknesses, but they should still stabilize the sediment

relative to the infinite slope model. We solve for a slightly higher critical flow depth for failure by calculating new expressions for wall and toe stresses for the supersaturated regime:

$$\tau_{w,surf} = \frac{1}{2} K_w z_t \left(\rho_s - \rho_f\right)(1-\eta) g \tan\phi_w \tag{4.20}$$

$$\tau_{t,surf} = \frac{1}{2} K_t z_t \left(\rho_s - \rho_f\right)(1-\eta) g \tan\phi_b \tag{4.21}$$

These definitions of $\tau_{w,surf}$ and $\tau_{t,surf}$ differ from eqs. (4.10) and (4.11) only in that $\frac{h^2}{z_t^2}$ is equal to unity. Substituting the definitions of $\gamma_{b,surf}$, $\tau_{w,surf}$, and $\tau_{t,surf}$ into eq. (4.14) and solving for $\frac{h_c}{z_t}$ yields:

$$\frac{h_c}{z_t} = \frac{\rho_s - \rho_f}{\rho_f}(1-\eta)\left(\frac{\tan\phi_b}{\tan\theta} + \frac{z_t}{W}K_w\frac{\tan\phi_w}{\sin\theta} + \frac{1}{2}\frac{z_t}{L}K_t\frac{\tan\phi_b}{\sin\theta} - 1\right) \tag{4.22}$$

Again, it is clear from eq. (4.22) that failures with larger surface areas (L and W) will fail with shallower flow depths.

4.2.2.2 Solving for the failure thickness with wall and toe stress

Solving eqs. (4.19) and (4.22) for h_c again requires that z_t is known. In addition, z_t varies with L and W when failure margins contribute to bed stability. For the purposes of this study, $L = 4$ m and $W = 9.7$ cm should be defined by the geometry of our experimental test section (see Section 4.3), because the largest failure is predicted to be the least stable. In cases with more complicated topographic or hydrologic conditions, the shape (L and W) and depth (z_t) of failure associated with the most susceptible failure geometry must be solved numerically (Milledge et al., 2014; Bellugi et al., 2015).

Because L and W are defined in our experiments we can solve directly for the most susceptible depth of failure, z_t. For failures that occur with surface flow present (eq. 4.22), the shallowest possible failure plane (a single grain layer) will be favored because of the high ratio of driving stress to resisting stress at the bed surface. This is exactly the same failure depth predicted by the infinite slope model (Sec. 4.2.1.2). However, failures occurring under subsaturated conditions will not necessarily fail at the deepest possible failure plane, as predicted by the infinite slope model. Although the saturation value is highest at the deepest possible failure plane ($[h_c/z_t]_{max} = H_c/Z$), the total resisting force exerted by the margins increases quadratically with depth. The most susceptible failure plane is therefore determined by a competition between linearly increasing driving stress and a quadratically increasing resisting stress with depth. We solve for the weakest failure plane by minimizing the total critical flow depth, H_c. We then solve for the critical $z_{t,c}$ by substituting $h_c = H_c - Z + z_t$ into eq. (4.19) and finding the minimum value of H_c. Differentiating eq. (4.19) with respect to z_t, setting $\frac{dH_c}{dz_t} = 0$, and solving for $z_{t,c}$ gives the failure thickness of the failure induced at the minimum saturation level required to initiate failure:

$$z_{t,c} = \frac{WK_A}{K_c} + \frac{\sqrt{\left[\frac{\rho_s}{\rho_f}K_A\left(\frac{\rho_s}{\rho_f}-1\right)\right]^2 - \frac{\rho_s}{\rho_f}\left(\frac{\rho_s}{\rho_f}-1\right)\left[\left(\frac{\rho_s}{\rho_f}\right)^2 K_A^2 - \left(\frac{\eta}{1-\eta}\sin\theta - \cos\theta\tan\phi_b\right)^2\right]}}{\frac{\rho_s}{\rho_f}\frac{K_c}{W}\left(\frac{\rho_s}{\rho_f}-1\right)} \tag{4.23}$$

Note that there are physical limits to $z_{t,c}$ that are not predicted by eq. (4.23). The failure cannot be thicker than the total thickness of unconsolidated material, Z, and it cannot be thinner than the diameter of a single grain size, D (Takahashi, 1978). If the predicted failure thickness is outside those physical bounds, then the failure thickness is

equal to the bounding value. We now have explicit equations to calculate the critical depth of failure across the supersaturated and subsaturated failure regimes, with and without accounting for the additional resistance generated by wall and toe stresses.

Inspection of eq. 4.23 (along with eqs. 4.16 - 4.16) suggests that failures on steeper slopes should occur with a smaller degree of saturation and therefore failure planes should be deeper. This progressive deepening of the failure plane on steeper slopes was predicted previously by Milledge et al. (2014), but it has yet to be tested experimentally.

4.3 Experimental procedure

4.3.1 Flume setup

To test the validity of eqs. (4.9), (4.7), (4.19), and (4.22), we conducted 47 slope stability experiments at the Caltech Earth Surface Dynamics Laboratory (Fig. 4.3). Our goal was to conduct experiments with a long section of uniform hydrologic conditions, uniform cohesionless sediment, and constant slope geometry to best approximate a one-dimensional stress state (e.g., Fig. 4.1). In order to accomplish this, our experimental test section was 5 meters in length with smooth vertical walls (spaced 9.7 cm apart) and a uniform sediment bed thickness for the middle 4 m section (Fig. 4.3). The upstream mounting location of the test section was on a pivot that allowed the inclination angle to be adjusted by changing the height of the downstream support (Fig. 4.3). Water was introduced only at the upstream inlet to the test section and was drained only at the downstream outlet of the flume, providing a uniform discharge throughout the length of

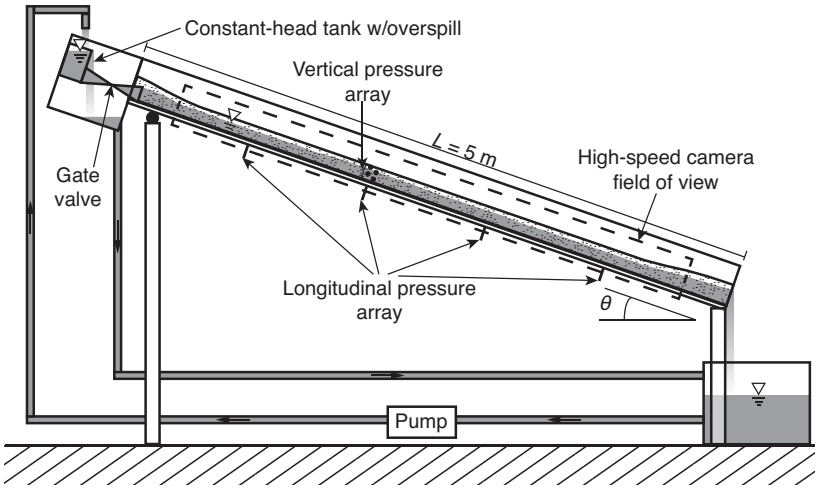

Figure 4.3: Schematic of the experimental flume.

Table 4.1: Sediment properties

Material	Median grain size, D_{50} (mm)	Material density, ρ_s (g/cm^3)	Porosity, η	Bulk friction angle, ϕ_b (°)	Friction angle with wall, ϕ_w (°)
Fine sand	0.7	2.7	0.42	38.4	28.2
Coarse sand	2	2.69	0.39	38.8	15.4
Fine gravel	5	2.65	0.43	41.1	16.7
Coarse gravel	15	2.65	0.43	45.6	15.2

the flume. The downstream boundary of the test section was a fixed mesh that allowed water to drain but provided a buttress for the granular material. This buttress forces the toe wedge of the failure (e.g., Fig. 4.2) to be located somewhere upstream of the outlet of the test section. The basal boundary condition of the experiments was a single layer of glued sediment grains that prevented sliding of the sediment along the otherwise smooth flume surface. The size of the glued grains varied with the sediment size of the experiment set (see below).

We conducted a total of 5 experiment sets. These experiment sets used different bed sediment size (D_{50}) and different bed thicknesses (Z). To test for the effects of

non-Darcian subsurface flow, we used four distinct unimodal grain sizes: D_{50} = 0.7, 2.0, 5, 15 mm. For each grain size we measured the material density (ρ_s), bulk porosity (η), dry bulk friction angle (ϕ_b), and the static coefficient of friction between the bulk material and the flume sidewalls (ϕ_w) (Table 4.1). Density was calculated by measuring displaced water volume in a graduated cylinder and the associated sediment mass with a balance. Bulk porosity was measured by filling a 5-gallon bucket with sediment and then measuring the increased mass associated with filling the pore space with water. Dry bulk friction angle was measured by placing an even thickness of dry sediment in a 1 m-long, 13 cm-wide flume and measuring the inclination angle of the surface at the time a granular avalanche was initiated. The coefficient of friction between the acrylic walls and each sediment type was measured by gluing the sediment to a block of wood, placing that rough block on an acrylic board, and measuring the inclination angle associated with the sliding of that block.

Each experiment began with planar bed of unsaturated sediment within the middle 4 m of the test section. For each experiment set we used a single bed thickness, ranging between 6 and 19.5 cm (Table 4.1). These bed thicknesses were chosen through a process of trial and error in an effort to minimize upstream and downstream boundary effects. To test for any effects of varying bed thickness relative to grain size (Z/D_{50}), we conducted two experiment sets with the coarse gravel: Z = 10 cm and 19.5 cm. In preliminary experiments for each grain size, failures would sometimes occur at one of the boundary conditions of the test section, either due to return flow at the downstream boundary contributing a bed-normal component of seepage stress (Iverson et al., 1986), or due to the generation of overland flow at the entrance to the test section, which quickly

Table 4.2: Experimental sets

Experimental set	Material	Slope range θ (°)	No. of obs. failures	Experimental bed thickness, Z (cm)	Average Reynolds number, Re
1	Fine sand	23.9 to 38.0	29	6	1.94
2	Coarse sand	23.9 to 36.5	31	8	28.1
3	Fine gravel	19.6 to 39.2	14	18	181
4	Coarse gravel	33.1 to 43.1	14	10	1040
5	Coarse gravel	41.2	2	19.5	1115
Prancevic et al. (2014)	Coarse gravel	25.2 to 33.0	8	10	921

entrained surface grains and grew into a self-sustaining debris flow. Either scenario represents failure conditions that violate our model assumptions, and these experiments were excluded from our analysis. In order to inhibit these premature failures, the upper and lower 0.5 m of the bed was graded into a thicker sediment bed, ensuring lower H/Z values at the boundaries, and encouraging failure to occur away from the boundaries (Fig. 4.3). Of the remaining failures that occurred within the zone of slope-parallel seepage, the failure locations were evenly distributed throughout the test section. The lack of a preferred failure location gives confidence that the stress distribution was consistent throughout the length of our test section for most experiments.

Within each experimental set, we varied bed angle as the independent variable and measured the flow depth required to initiate bed failure at that bed angle. The range in bed angles for most of the experimental sets extended from a value close to the bulk friction angle of the material down through the slope range in which subsaturated failures occur (Table 4.2). The one exception to this was Experiment Set 5, which tested failure conditions at only one bed angle.

After the test section was prepared (bed angle set and sediment planed), experiments

proceeded by incrementally increasing the discharge flowing into the top of the test section until the conditions for failure were reached. For the 0.7 mm and 2.0 mm sand, water discharge entering the test section was controlled using a valve connected to a constant head tank (Fig. 4.3). The maximum discharge of the constant head tank was too low for use with the highly permeable 5 mm and 15 mm gravels and instead a centrifugal pump was used to overspill water into the test section from the head box. For all experiments, increments of increased discharge were limited to 10% of the preceding discharge. At each new discharge, the flow was allowed to achieve a steady-state depth throughout the entire length of the test section before any measurements were made. The steady-state condition was determined by monitoring the pressure readings from four basal pressure sensors, and the time required to achieve steady state ranged from 15 s for the coarse gravel to 720 s for the fine sand.

Once a steady state was achieved, we made measurements of the hydrological conditions. We calculated flow discharge by collecting water at the outlet of the flume over a known time interval and weighing it. For most experiments we recorded flow depth using two methods: 1) by making visual observations of pore saturation once per each stable discharge at 1 mm resolution, and 2) continuously by measuring basal pore pressure with transducers mounted through the floor of the flume at distances of 1, 2, 3, and 4 m from the inlet of the test section (Fig. 4.3). The partial saturation in the fine sand prohibited the visual estimation of saturated depth, and we rely only on pressure measurements for this experimental set. All pressures sensors were gauge sensors (pressure measured relative to atmospheric) made by Omega (PX409) with 0.06 mbar (0.6 mm water-pressure head) specified accuracy. They were calibrated several times per week to 1 mm accu-

racy and were tared before being submerged for each experiment. We were able to use these basal pressure measurements to continuously monitor flow depths by assuming a hydrostatic pressure distribution: $H = p/(\rho_w g \cos\theta)$, where p is measured pressure.

Failures typically occurred within a few minutes of an increase in discharge. We utilized a Phantom high-speed camera to record each experimental failure. The camera captured the entire 4 m planar section of the flume with frame rates up to 250 fps. The camera was synced with the pressure sensors to precisely record the timing of the failure and was also used to estimate the depth of the failure plane, z_t. Using the observed time of failure from the videos and the continuously recorded pressure data, we calculated critical flow depths, $H_{c,P}$, within one second of each failure. The water surface was not visible in the high-speed video due to low contrast between the air and water, but visual estimates of flow depth noted during experiments, $H_{c,v}$, provided a redundant measurement of the critical flow depth for conditions just prior to failure.

4.3.2 Sources of experimental error

4.3.2.1 Potential error from depth measurements

Visual observations of flow depth and the distribution of measured pore pressures indicate that, on average, flow depths were approximately uniform throughout the length of the flume for most failures. Consequently, we were able to use the average of the multiple pressure measurements along the length of our flume to calculate flow depths to average out some of the error associated with individual measurements. Occasionally, we would measure large spatial anomalies in pressure ($\pm > 20\%$) at one or more sensor at the time

of failure. If inspection of the high-speed video suggested that this anomalous pressure was not associated with any real change in flow depth and the pressure measurement was not within 1 m of the failure then we excluded the pressure measurement as erroneous in our calculation of flow depth. After any anomalous pressure data was removed, we characterized the error of an individual experiment as the average standard error of all remaining pressure measurements at the time of failure. If the standard deviation of critical flow depths between repeat experiments with the same experimental condition was larger than the standard error associated with the pressure measurements, then this standard deviation was reported in the error bars (Fig. 4.7).

To further characterize our uncertainty, we have plotted both our visual estimates of flow depth within 5 min of failure (continuous observations are not available) and the average flow depth as calculated from the pressures measured within 1 s of failure. Small differences between these two depth measurements are expected because they were not collected at the same time, and in many cases they may have been collected at slightly different discharges. Still, a general agreement between these two measurements for a given experimental condition should provide greater certainty of our results.

4.3.2.2 Potential error from bulk flow accelerations

Although the middle 4 m of the flume was planed to an even thickness, we did observe some variability in the depth of flow in the subsurface (e.g., Fig. 4.6). These flow depth variations likely represent some downstream variability in porosity and/or hydraulic conductivity. They can contribute to bed stability through two primary mechanisms: 1) momentum gain or loss due to spatial accelerations of the flow and 2) non-parallel seep-

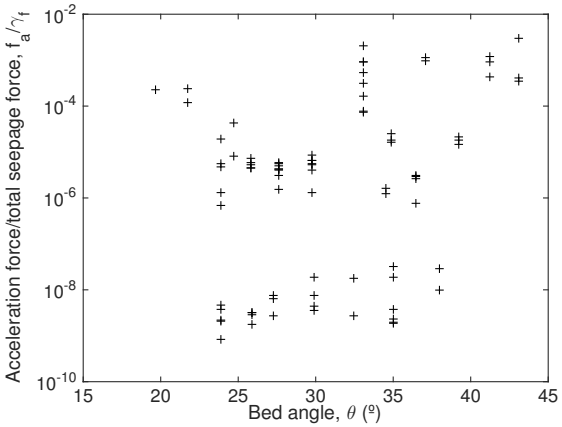

Figure 4.4: The relative forces exerted on the bed from acceleration of the flow and the total seepage stress, as a function of bed angle. All experimental data are plotted.

age vectors that can push grains away from or towards the floor of the flume. We examined our longitudinal pressure profiles and flow depth notes and found that depth variations greater than 2 cm between two pressure sensors (1 m distance) were extremely rare. This indicates that seepage vectors very rarely deviated by more than 1° from the average bed angle, even when potentially erroneous pressure measurements (Sec. 4.3.2.1) were included. Also, the force density associated with this change in flow depths is equal to:

$$f_a = \rho_f \frac{\Delta H}{\Delta x} \frac{\overline{U}^2}{\overline{H}} \tag{4.24}$$

where U is the spatially-averaged velocity of the pore fluid, which we calculated by continuity and using measurements of flow discharge and depth. Eq. (4.24) was always calculated to be several orders of magnitude smaller than the downstream component of the unit weight of pore water in our experiments. Our analysis indicates that this change in momentum contributes at most 0.3% of the total seepage stress (Fig. 4.4). In addition, on average there was not a systematic slope in the water surface in our experiments. This means that a local drop in seepage stress would need to be compensated by an increase

in seepage stress elsewhere, which should lead to locally higher values of seepage stress and premature destabilization of the bed. This effect would be small, though, and well within our reported error bars.

4.3.3 The expected effect of wall and toe stresses

By using smooth walls and a long experimental flume we have attempted to minimize the stresses due to wall and toe friction (eqs. 4.19 & 4.22). Still, the width and length of the experimental test section is finite and wall and toe resistance will provide some stabilizing forces to the bed. Because our experiments utilize a simple geometry and have well-constrained bed properties, we can predict the influence of each stress on our slope stability models. The results will allow us to test the validity of wall and toe stress calculations (eqs. 4.10, 4.11, 4.20 & 4.21). By adding wall stress and toe stress to the infinite slope model sequentially we can predict the relative stabilization associated with these stresses. For example, for Experiment Set 1, wall stress is expected to increase the subsurface saturation level required for failure by up to 2 cm (Fig. 4.5). This indicates that, despite the smooth walls used in the construction of our test section, the relatively narrow width is expected to stabilize the bed. This stabilizing effect is maximized on steep slopes where failures are deep and wall stresses are high, and is almost negligible within the surface failure regime where failure depths become small relative to the flume width (Fig. 4.5). In contrast, the model predictions suggest that the stabilizing effect of toe stresses is small due to the long flume length relative to the bed thickness ($L/Z = 67$), even on steep slopes. The increased saturation level required to overcome toe stress in

our 4 m test section (as compared to an infinitely long one) is less than 0.16 cm, which is only 2% of the total bed thickness: $Z = 8$ cm (Fig. 4.5).

Wall and toe stress are also expected to have a substantial impact on the depth of failure. For the same experiment set (Set 1), we can calculate the expected depths of failure (z_t) for an infinite slope and with wall and toe stresses. As discussed in Section 4.2.1.2, the infinite slope model predicts an abrupt shift from the shallowest possible failure plane in the supersaturated failure regime to the deepest possible failure plane in the subsaturated failure regime. However, because wall and toe stresses increase quadratically with depth, failure planes in finite sediment beds are expected to gradually transition from shallow failure planes to deep failure planes (Fig. 4.5). In general, adding stresses at the margins results in shallower failures unless the thickness of the failure is limited by the total thickness of the bed. For bed angles steeper than $\theta > 30°$ in this experimental configuration, the failure plane depths converge to the flume floor for all models (Fig. 4.5). Again, most of the shallowing of the failure plane is predicted to occur due to wall stress because our long experimental flume minimizes the effect of toe stress.

4.4 Experimental Results

4.4.1 Failure characteristics

All examined experimental conditions exhibited *en masse* failure of the granular slope. Failure behavior commonly varied between different grain sizes. The finest material ($D_{50} = 0.7$ mm) rarely exhibited catastrophic failures, and instead failed as slumps that

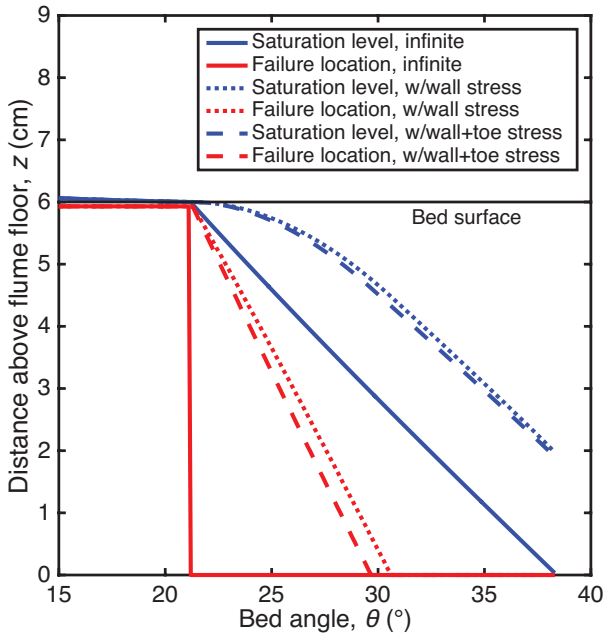

Figure 4.5: Prediction of the water level (blue line) and failure plane location (red line) for Experiment Set 1, as measured relative to the flume floor in the bed-normal direction. The solid lines are the predicted locations for an infinite slope, the dashed lines includes the stabilizing effects of wall stress, and the dotted lines include both wall and toe stresses. On steeper slopes, the saturation level and failure plane location move deeper into the bed, approaching the flume floor ($z = 0$ cm). For a given slope, adding stabilizing forces (wall and toe stress) push the saturation level and failure plane location towards the surface. For predictions including wall and toe stresses, the failure length ($L = 4$ m) and width ($W = 9.7$ cm) are assumed to be set by the size of the test section.

moved downslope slowly, sometimes stalling after moving only several centimeters. These slumps often left ~ 1 cm-high headscarps that were supported by suction stress near the bed surface (Fig. 4.6A). In many experiments, the coarse sand ($D_{50} = 2$ mm) also exhibited slow-moving slides that would continue downslope in pulses. At the steepest slopes tested with the coarse sand, however, catastrophic failures rapidly accelerated downslope, evacuating the entire sediment bed (Fig. 4.6B). Both of the gravel materials ($D_{50} = 5$ and 15 mm) primarily failed in this latter fashion, and high-speed video was required to visualize the rapid deformation of the sediment bed (Fig. 4.6C, Supplemental video). The gravel experiments also tended to fail with a failure thickness, z_t, that was

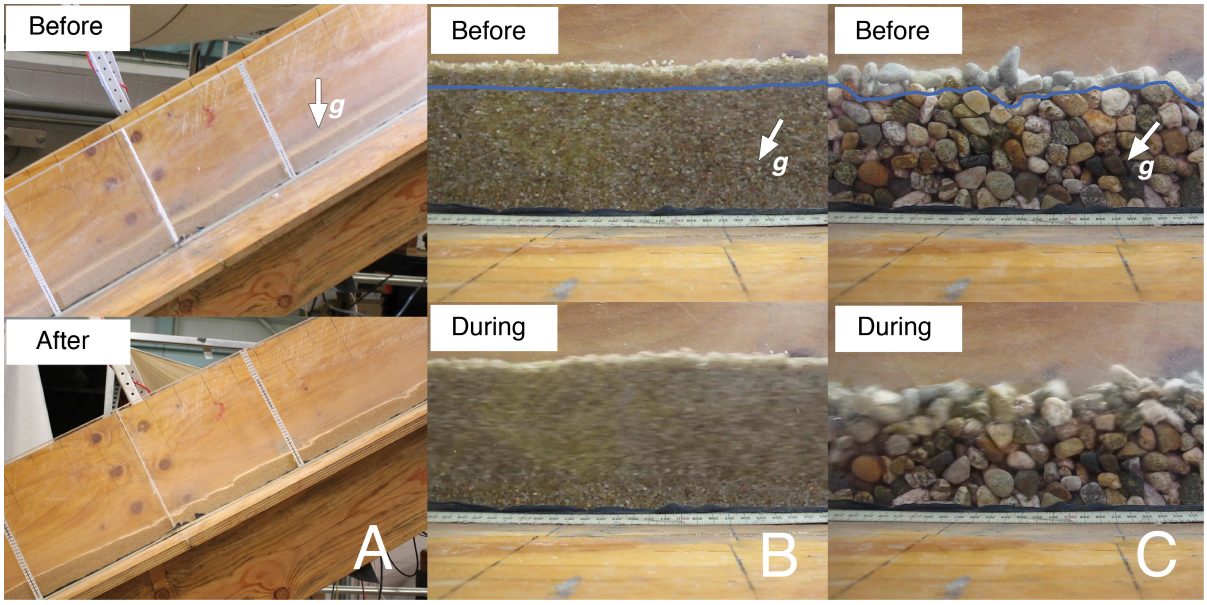

Figure 4.6: Photos of experimental slope failures using A) 0.7 mm sand, B) 2 mm sand, and C) 15 mm gravel. Although the flume was tilted to $\theta = 34.5°$ and 41.2° in (B) and (C), respectively, the photographs were captured with the camera mountain parallel with the flume floor. A gravity vector in each panel shows the vertical downward direction. The top half of each panel shows the sediment bed prior to slope failure. The bottom half shows the bed after the failure (A) or while the slope is actively failing (B) and (C). The motion blur of panels (B and C) provides a visualization of the depth of initial failure in those experiments.

closer to the surface than the sand experiments (Fig. 4.6C), which will be discussed in detail in Section 4.4.3.

Table 4.3: Experimental results

Experiment set no.	Bed angle, θ (°)	Number of measured failures	Average critical flow depth (visual), H_c (cm)	Standard deviation of repeat critical flow depths (cm)	Average critical flow depth (pressure), H_c (cm)	Standard error of pressure readings (cm)	Failure thickness, z_t (cm)	Standard deviation of thickness (cm)
Set 1	23.9	5	-	-	6.53	0.622	2.1	1.90
Fine sand	25.9	5	-	-	6.31	0.487	4.2	1.11
($D_{50} = 0.7$ mm)	27.3	3	-	-	6.13	0.370	4.6	0.39
$Z = 6$ cm	29.9	4	-	-	5.77	0.242	5.3	0.50
	32.4	2	-	-	5.24	0.498	5.8	0.00
	35.0	8	-	-	3.90	0.385	5.2	0.63
	38.0	2	-	-	3.87	0.244	5.6	0.59
Set 2	23.9	5	8.3	0.340	9.26	0.246	2.4	1.49
Coarse sand	25.8	5	8.0	0.000	8.18	0.493	5.1	0.73
($D_{50} = 2$ mm)	27.6	8	8.0	0.000	8.35	0.405	4.4	1.31
$Z = 8$ cm	29.8	7	8.3	0.255	8.19	0.461	6.0	1.45
	34.5	2	6.4	1.013	7.24	0.353	7.9	0.21
	36.5	4	7.2	0.277	6.69	0.299	7.9	0.12
Set 3	19.6	1	18.4	0.000	18.71	0.316	0.6	0.00
Fine gravel	21.7	2	18.5	0.000	17.79	1.045	1.1	0.00
($D_{50} = 5$ mm)	24.7	2	17.6	0.141	18.12	0.592	2.7	1.57
$Z = 18$ cm	33.1	3	17.7	0.065	16.66	0.552	5.8	2.23
	34.8	3	16.5	1.276	17.60	0.610	8.2	1.23
	39.2	3	13.4	1.008	13.58	0.857	11.3	3.17
Set 4	33.1	5	10.0	0.354	10.41	0.388	3.0	0.76
Coarse gravel	37.1	2	9.8	0.223	10.51	0.582	2.4	0.37
($D_{50} = 1.5$ cm)	41.2	5	11.0	1.420	10.13	0.360	3.3	1.03
$Z = 10$ cm	43.1	4	9.2	0.825	9.13	0.128	4.8	1.63
	25.2*	2	11.4	0.354	-	-	-	-
	27.9*	2	10.9	0.163	-	-	-	-
	30.1*	2	10.7	0.233	-	-	-	-
	33.0*	2	10.2	0.005	-	-	-	-
Set 5	41.2	2	19.1	0.685	19.24	0.3727	4.2	0.75
Coarse gravel								
($D_{50} = 1.5$ cm)								
$Z = 19.5$ cm								

* The last four experiments of Set 4 are from Prancevic et al. (2014). Pressure data and failure thicknesses are not available from these experiments.

4.4.2 Degree of saturation at failure

In general, failures for all grain sizes exhibit the expected trend of decreasing critical flow depth, h_c, with increasing bed slope (Table 4.3, Fig. 4.7). The observed critical flow depths for all experiments are higher than predicted by the infinite slope stability model (eq. 4.7). Some of this enhanced stability is likely due to wall and toe stresses in our finite experimental configuration. Surprisingly, though, the bed was observed to be much more stable than is even predicted by our model predictions that include these additional stresses. With the exception of the steepest experiments, most failures were not initiated until the subsurface flow depth was within 1 cm of the bed surface. Even at slopes approaching the dry bulk friction angle of each material, critical flow depths were never observed to be shallower than 50% of the bed thickness ($H_c/Z \geq 0.5$). The pore pressure measurements and visual estimates of flow depth are in general agreement regarding this enhanced stability for all experiments. In addition, the enhanced stability exists for all experiment sets regardless of grain size, indicating a common stabilizing mechanism and suggesting that the degree of turbulence in the subsurface does not measurably affect stability.

4.4.3 Depth of failures

We observed considerable scatter in the failure thickness at the time of initiation, z_t, resulting in large error bars for any particular experimental configuration (Fig. 4.7, Table 4.3). However, within each experiment set we generally observed that the failure plane gradually deepened on steeper slopes. This is in contrast to the infinite slope stability

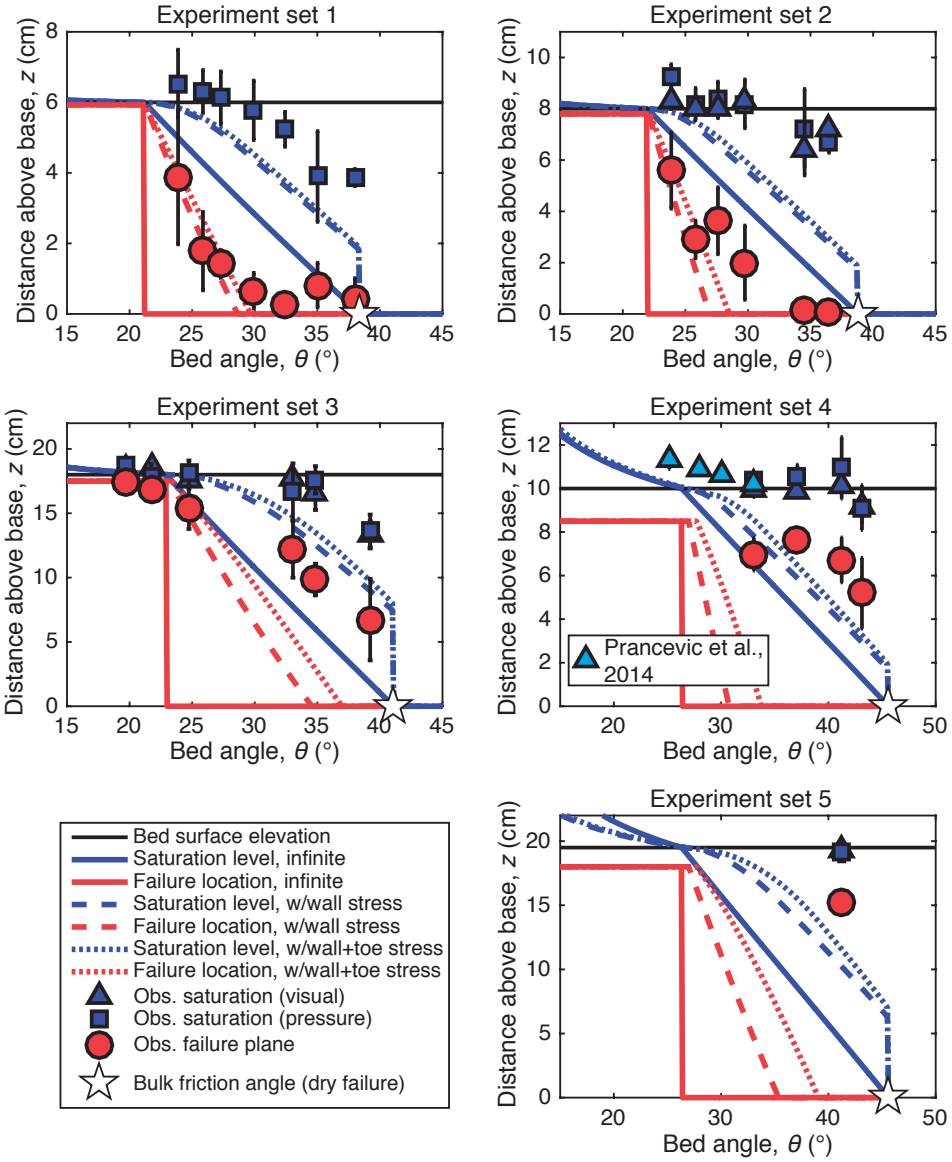

Figure 4.7: The critical flow depth required to initiated slope failure and the initial failure plane depth as a function of slope for all 5 experiment sets. The base of the sediment bed (flume floor) is located at $z = 0$ cm, while the horizontal black line indicates the bed surface for each experiment set. The data points correspond to paired experimental observations of critical flow depth (blue squares and triangles) and initial failure plane depth (red circles). The error bars represent either the standard deviation between repeat experiments at the same bed slope (failure plane depths and saturation levels) or the standard error of the four longitudinal pressure measurements at the time of failure, if larger (saturation levels only). Three model predictions are shown for each experimental set: the stability of an infinite slope (solid lines), the stability of a slope with finite width and wall stress (dashed lines, $W = 9.7$ cm), and the stability of a slope with finite width and depth (dotted lines, $W = 9.7$ cm and $L = 4$ m). Paired predictions are shown for each model output of both the failure plane location (red lines) and critical saturation level (blue lines). If a model prediction is correct, the data points for saturation level and failure plane depth should fall on the same respective line style for the paired predictions (dotted, dashed, or solid).

model (eqs. 4.7 & 4.9), which predicts that the failure plane abruptly shifts from the surface grain layer in the supersaturated failure regime ($H_c > Z$) to the deepest possible failure plane ($z_t = Z$) in the subsaturated regime ($H_c > Z$). Instead, our observations are consistent with the model that includes the stabilizing stresses of wall and toe stress, which predicts a gradual steepening due to the depth-dependence of earth pressure. The failure thickness values predicted by the slope stability model that includes wall and toe stress does not match all of our experimental data (the depths of failure for the gravel material is generally overpredicted compared to our observations), but the general trends are correct (Fig. 4.7).

Outside of these trends, there is stratification in the depth of failure between experiment sets. Relative to bed thickness, failures in both sets of sand experiments were generally deeper than in the gravel experiments. In particular, at slopes close to the bulk friction angle, the sand experiments had failure planes that approached the floor of the test section and the failure planes for the gravel experiments were relatively close to the surface (Fig. 4.7). However, the total bed thickness for the gravel experiments was also larger than for the sand experiments. In terms of absolute failure thickness, the gravel and sand experiments are more similar. This suggests that failure thickness does not scale linearly with total bed thickness.

4.4.4 Length and width of failures

Marginal stresses are expected to have a greater stabilizing effect on the bed as failures becomes shorter and narrower (refer to eqs. 4.22 & 4.19), suggesting that longer and wider

failures will be favored, as is assumed in our model predictions. For our experiments, this suggests that the most susceptible failure plane should extend for the entire length of the uniform sediment bed (4 m) and across the entire width (9.7 cm). Consistent with this theoretical expectation, the width of all failures spanned the entire width of the test section in our experiments. However, contrary to the expected preference for long failures, our experimental failures rarely initiated throughout the entire length of our test section. Estimating the initial length of failures was difficult because failures typically grew very quickly once initiated. Visual assessment of the high speed videos suggest that failures typically initiated with a length between 0.3 m and 1 m. However, these estimated lengths are only approximate and vary considerably between experiments. In addition, it was difficult to visually distinguish the upslope slab from the toe wedge (e.g., Fig. 4.2) and these failure lengths are a measure of the entirety of the mobilized mass. In terms of model inputs, these estimated failure lengths correspond roughly to upslope slab lengths between $L = 0.1$ and 1 m.

This ambiguity of the initial failure length limits our ability to accurately assess our predictions of the critical saturation level. However, the range in failure lengths provides us with a range of predicted critical saturation levels. For most of our experimental conditions, the predictions associated with this range in failure lengths bracket our experimental observations (Fig. 4.8). The conditions where this range of predictions remains somewhat inaccurate is for the steepest experiments using the coarse gravel. The error bars for these experimental observations lie slightly outside of our model predictions, even when the failure length is predicted to be only 10 cm long. The tendency for the coarsest material to be more stable than the rest of the tested materials may be a result of the

small ratio of width to grain size ($W/D_{50} = 6.5$). This ratio is within the width regime where particle jamming is expected to occur ($W/D < 7$), meaning that force chains between particles can span the width of the test section to provide an additional stabilizing force. Outside of these experiments, the model predictions that assume a short failure length are adequate to predict a the critical saturation level required for failure.

4.5 Discussion

4.5.1 Stability and Reynolds number

In some derivations of infinite slope stability researchers have proposed that the model should only hold if the flow is within the Darcy regime (Bear, 1972; Iverson et al., 1986), although other derivations do not specify this requirement (Lambe et al., 1969; Takahashi, 1978). Our experiments that use gravel material have very high particle Reynolds numbers ($Re = 181$ and 666) and also exhibit a non-linear relationship between specific subsurface discharge, q_s, and bed slope (Fig. 4.9), which is expected for flows that are outside of the Darcy regime. The Reynolds number of the fine sand used in our experiments ($Re = 1.94$) is within the commonly reported range for Darcian flow ($Re <\sim 10$)(Bear, 1972, p. 126). The coarse sand has an average Reynolds number that is just outside of this regime ($Re = 28.1$), but both sandy materials display a relationship between q_s and $\tan\theta$ that are approximately linear. This suggests that the Darcian assumption is satisfied in our experiments with fine sand, and is close to being satisfied in our coarse sand experiments. Despite the wide range in Re for our

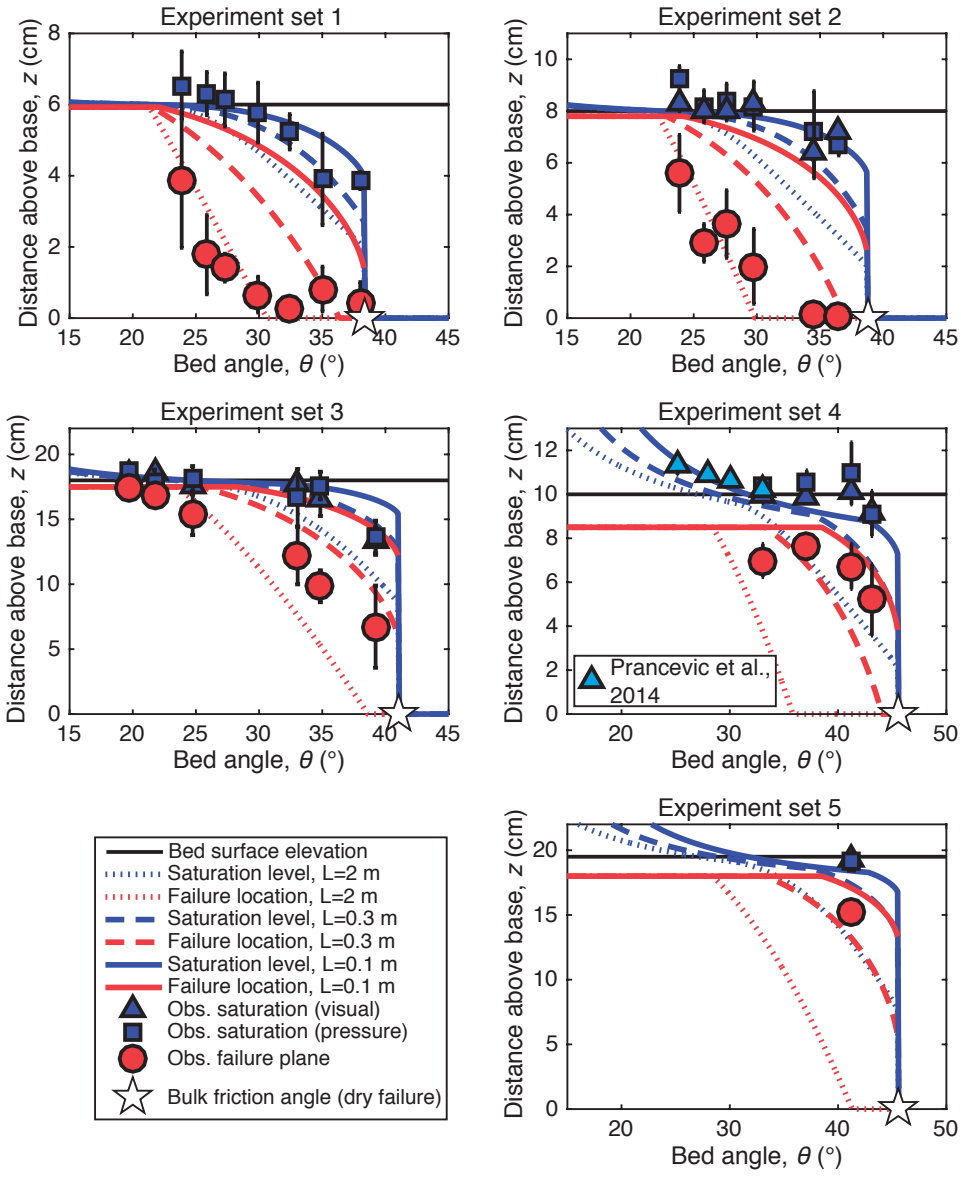

Figure 4.8: The same plots as shown in figure (4.7), but with new model predictions made for short failures. The new model predictions show how the length of failure is expected to affect both the saturation level required to initiate failures (blue lines) and the initial depth of failure (red lines). Decreasing the failure length to $L = 0.3$ m or $L = 0.1$ m yields a predicted increase in the stability of the beds, and improves the fit with our observed experimental conditions.

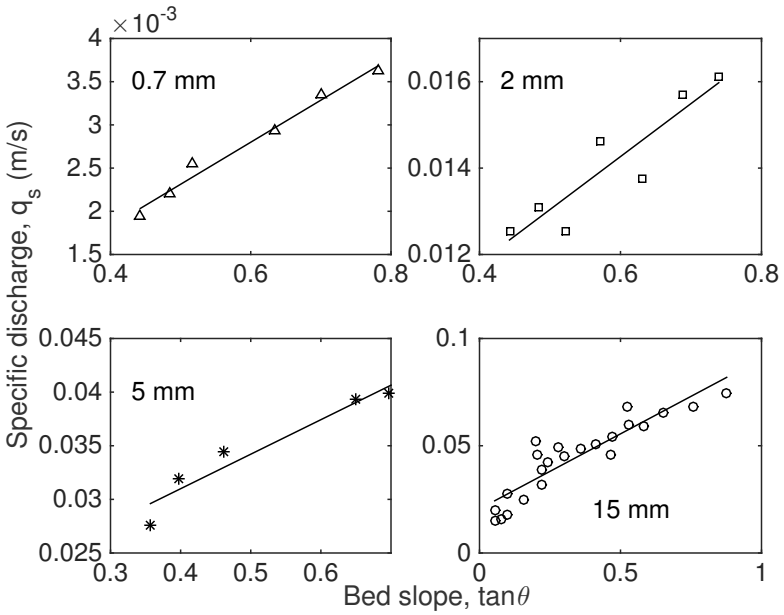

Figure 4.9: Specific discharge as a function of bed slope for each material. A good fit to a linear trend (shown in solid lines for each material) indicates that the subsurface flow is Darcian while a curve that rolls over at steep slopes suggests non-Darcian flow.

different granular materials, the offset between our results and the model predictions is surprisingly consistent between the various grain sizes (Fig. 4.7). These results suggest that the infinite slope stability model is equally valid in both Darcian and non-Darcian subsurface flow regimes.

4.5.2 What sets failure size?

4.5.2.1 Failure length

Slope stability models indicate that longer failures experience a smaller relative contribution of stabilizing toe stress compared to the overall weight of the failing mass (eqs. 4.19 & 4.22). Consequently, it is expected that long failures should initiate at saturation levels that are lower than those required for short failures (Fig. 4.8). However, when

we input the maximum failure length possible in our experimental test section, our slope stability model underpredicts the stability of the bed for all experiments. This underprediction resulted from failures not initiating along the entire length of the test section, and instead favoring failure lengths that were between $L = 0.1$ and 1 m. The shorter length of typical failures, and the increased relative contribution of toe stress of such geometries, provides a mechanism to accurately reconcile slope stability predictions with observed failure conditions (Fig. 4.8). Unfortunately, though, our model failed to predict the length of failures, indicating missing component(s) or violated assumption(s) in our slope stability derivation.

One potential explanation for the unexpected preference for smaller failures in our experiments is spatial variability in the stress state along the length of the experimental bed. The slope stability model presented here explicitly assumes that hydrologic and granular conditions are uniform along the length of the test section. Although we attempted to construct the bed in a uniform manner before each experiment, natural granular material is inherently non-uniform at the grain scale. This variability at the grain scale can result in larger-scale heterogeneities in the bulk friction angle, permeability, and porosity, as evident by standard deviations on the order of 10% in pressure measurements (Table 4.3). Therefore, despite a uniform slope geometry, bed thickness, and water discharge, the stress balance determining the stability of natural grains is spatially variable. In addition, such variability is likely dependent on the scale of the failure, with variability at the grain scale being largest and then decaying over larger volumes as heterogeneities are balanced out. So, although the stabilizing effects of wall and toe stresses may be higher for small failures, deviations from the mean conditions are also

likely more pronounced over shorter length scales.

In our experiments, this competition between heterogeneities in the stress balance over short length scales and reduced relative contribution of toe stress for long failures likely results in a preferred length of failure. Although our visual estimation of failure lengths is uncertain, we did not notice systematic trends in failure length between our experimental sets. This may indicate that failure length does not scale strongly with grain size or the total bed thickness. The lack of scaling with bed thickness is expected in our experiments because failure planes rarely initiated along the base of the sediment bed. In other words, with the exception of Experiment Set 1, in which deep failures were observed, the failures generally did not feel the base of the sediment bed and behaved independently of bed thickness. In settings where the sediment bed is thinner, the total sediment thickness may have an impact on the length (and perhaps width) of the failure.

Unlike bed thickness, failures in our experiments always occupied the entire width of the test section and we have calculated wall stress to significantly enhance the stability of the bed. Although shorter failures are predicted to be overall more stable, the relative contribution of wall stress to the total stabilizing stress is smaller for shorter failures. Perhaps in reducing the failure length, the failure achieves some optimal ratio between wall and toe stress that allows stress heterogeneities to promote failures. If true, this suggests that there is some optimal ratio between the length and width of failures. Based on our visual estimations of failure length and the fit between our experimental observations and model predictions (Fig. 4.8), the optimal length-to-width ratio of our experiments is $L/W = 1$ to 3. These values are consistent with previous observations of landslide scars in the field that all report typical length-to-width ratios of $L/W \approx 2$

(Reneau et al., 1987; Dai et al., 2002; Taylor et al., 2015). The typical explanation for this persistent ratio is that it reflects the characteristic aspect ratio of convergent hollows (e.g., Reneau et al., 1987). However, the preference for these length-to-width ratios in our experiments, despite our long experimental test section, suggests that this optimal ratio may be driven by internal stress balances rather than external geometries. If true, this simple scaling between length and width would reduce landslide prediction from a 3-dimensional problem to a 2-dimensional problem.

Before this ratio is applied, however, a clearer mechanistic explanation must be developed and verified. In particular, only limited data is available to characterize the variability of bulk friction angles and seepage stress stress as a function of grain size and bed geometry. More data on this variability will be crucial to simplifying landslide predictions.

4.5.2.2 Failure depth

The failure depth data presented here show that a landslide of a given surface area is likely to be deeper on a steep slope than it is on a lower slope (Fig. 4.7). The transition to deep failures is not abrupt, as suggested by the infinite slope stability model (Takahashi, 1978). Instead, our data show that in finite failures that lack cohesion, failure depth gradually deepens on steeper slopes. In thick sediment beds (e.g., Experiment Sets 3, 4, and 5), wall and toe stresses may prevent the initial failure plane from the reaching the base of the sediment bed even at slopes close to the bulk friction angle (Fig. 4.8). In shallow sediment beds (e.g., Experiment Sets 1 and 2), the failure plane moves deeper into the subsurface on steeper slopes until it reaches the base of the sediment bed, where

it remains up to slopes approaching the bulk friction angle. This is consistent with our predictions and those of Milledge et al. (2014), both of which consider the stabilizing effects of wall and toe stresses.

Slope is not the only factor in determining the depth of a bed failure. Although it was not tested in our experiments, the stability models presented here and in Milledge et al. (2014) predict that deeper failure planes should occur in longer and wider failures (e.g., Fig. 4.8). This is expected because wall and toe stresses become smaller compared to basal friction as failures become wider and longer, allowing the increased saturation of deeper failures to dominate the stress balance.

In addition, our experimental results suggest that grain size may affect the depth of failure, even within the subsaturated failure regime. Within the supersaturated failure regime, where the shallowest possible failure plane is favored, it is expected that the representative grain diameter sets the failure plane depth (Takahashi, 1978). We did not extensively probe the surface failure regime in our sandy experiments, but comparing the low-sloping data for Experiment Sets 3 and 4 shows the occurrence of shallower failure planes for the 5 mm gravel, compared to 1.5 cm gravel (Fig. 4.8). What is more surprising is our observation that deeper failures occurred in the sand experiments (Sets 1 and 2) than in the gravel experiments (Sets 3-5) within the subsurface failure regime. There is no clear explanation for this observation, and the phenomenon is not predicted by our slope stability model. For the coarse gravel experiments (Sets 4 and 5), the large grain diameter relative to channel width ($W/D_{50} = 6.5$) could have resulted in an additional jamming stress that anomalously resists failure at depth. This could explain the extremely shallow failures observed in those experiments. The difference in

failure plane depths could also reflect a bias in our measurements in which we were able to visually identify failures in the coarser material sooner after initiation. If the fine-grained experiments had more entrainment of underlying grains before the failure plane could be identified, then this would bias our depth measurements toward deeper failure planes for those experiments. Higher-resolution observations of the failure plane in future experiments could help exclude or confirm this possibility.

4.5.3 The role of total saturation at failure

The preference for relatively small failures has driven both the failure plane and the critical saturation level closer to the surface. This occurs regardless of total bed thickness, particularly when the failure depth is above the bottom of the sediment bed. To show this, we have plotted the width-normalized distance from the bed surface to the water surface ($(H_c - Z)/W$) as a function of normalized bed slope (Fig. 4.10). Normalizing the distance by width does not affect the display of our results in any way, as all of our experiments used the same width, $W = 9.7$ cm, but because wall stresses appear to play an important role in determining failure thickness, we expect that the critical flow depth to initiate failure scales with width more than bed thickness. Our experiments utilized a wide range in grain sizes and bed thicknesses, and despite this, the flow depth measured relative to the bed surface nearly falls onto a single curve for all of our experiments (Fig. 4.10). In fact, in 23 of the 28 experimental conditions presented here, the water surface was within 1 cm of the bed surface before failure was initiated (Table 4.3). This is a surprisingly tight distribution of saturation depths given our wide range in bed angles:

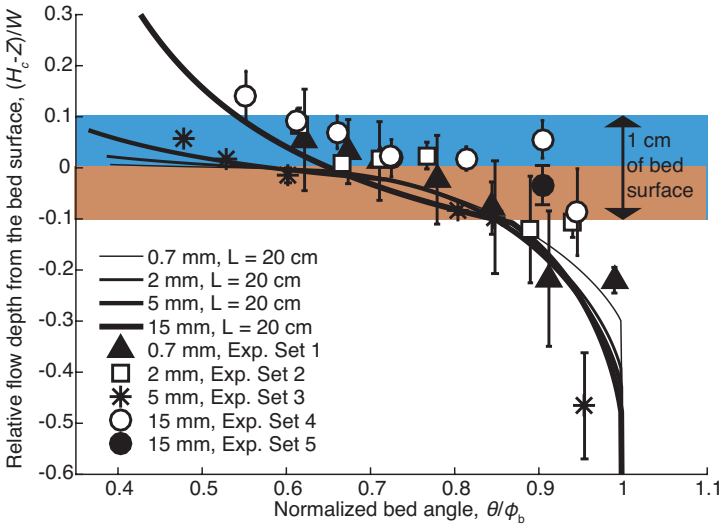

Figure 4.10: The critical flow depth measured relative to the bed surface and normalized by channel width, as a function of relative bed angle. All curves are model predictions of slope stability for the grain sizes tested with a length of failure, $L = 0.2$ m. Experimental data points represent the average of depths estimated visually and those measured with the pressure sensors. The blue and brown shaded backgrounds correspond to 1 centimeter above and below the bed surface, respectively.

19.6° to 43.1°.

4.5.4 Application to field predictions

If this observation of failures only occurring very close to saturated conditions holds in the field, it could greatly simplify landslide modeling, both for landslide hazard prediction and landscape evolution modeling. There are significant complexities on natural hillslopes that are not present in our laboratory experiments, by design. For example, root cohesion is extremely variable and difficult to predict (Schmidt et al., 2001). In addition, the failures in our experiments were constrained to a very narrow width, relative to bed thickness. In unconfined failures, width may be very large relative to the bed thickness. We expect that in the cases where the failure width is much larger than the bed thickness, there will be two major differences in predictions: 1) failure planes are predicted to reach

the base of the shallow sediment bed ($z_t = Z$), and 2) the relative contributions of wall and toe stresses will be significantly reduced. In such cases, the enhanced stability that we have observed in our experiments due to large marginal stresses will be less pronounced. We also expect that the saturation level required for failure will be dominantly set by the total bed thickness, rather than the channel width (e.g., Fig. 4.10), since the total bed thickness will set the depth of failure.

As a result, we expect the stabilization by marginal stresses will be most pronounced when failures are constrained laterally. Such a constraint could be in the form of immobile (bedrock) walls flanking the failure, lateral variability of root strength or friction angle, or the concentration of driving stress over a finite width. This latter scenario is perhaps most common in continuously soil mantled landscapes, where failures are typically initiated in swales where subsurface flow converges in the concave portion of the topography. If a valley is highly concave, such that runoff is focused into a narrow strip of soil, then our results suggest that marginal stresses will be substantial and will affect the stability of that terrain. It is potentially these marginal stresses that lead topographic landslide prediction models to generally overpredict the occurrence of failures in highly convergent topography, while failing to predict some failures on planar hillslopes (e.g., Montgomery et al., 1994).

In rockier landscapes where soil mantling is discontinuous, exposed bedrock could laterally constrain failure width. There is an increased recognition that within rocky landscapes debris flows are commonly initiated in very steep colluvial channels (Rickenmann et al., 1993; Berti et al., 2005; Cannon et al., 2008; Kean et al., 2011). These channel beds typically lack significant cohesion and often have well-defined width con-

straints, making them quite similar to our experimental conditions. The marginal stresses acting to stabilize failures in these environments may large, depending on valley width relative to colluvial thickness.

4.6 Conclusions

We have conducted the first experimental tests of the stability of a sediment bed undergoing steady, slope-parallel seepage in an effort to verify the infinite slope stability model. Because our experimental setup had a relatively narrow width, we also compare our results to model predictions that include stabilizing stresses at the margins (walls and toe wedge). We found that the infinite slope model underpredicts the stability of all tested grain sizes at all slopes. Incorporating additional frictional stress at the toe and walls of our failures significantly improved the fit between stability models and our data. However, our experimental failures were observed to be substantially shorter than predicted, typically spanning only a few decimeters in length, while failures spanning the entire length of the test section (4 m) are predicted to be most susceptible to failure. This preference for short failures is not predicted by the models we tested but it is consistent with field studies that consistently report length-to-width ratios of $L/W \approx 2$.

These results support several broad conclusions regarding the stability of slopes subjected to groundwater flow. Marginal stresses stabilizing the wall and toe of the failure drive the failure plane surface and the critical saturation level closer to the bed surface. In our experiments, failures typically occurred only when the bed was nearly completely saturated, despite testing a wide range in grain sizes over a wide range in slopes. Natu-

ral channels can vary significantly from our experimental conditions in their dimensions, soil properties, and presence of roots, but in cases that are well-approximated by these experiments, the tendency for failures to occur close to saturation may greatly simplify slope stability predictions.

Our data also show that the depth of failures gradually increase from the surface grain layer to the full thickness of the bed as bed angle increases. We found that slope stability models accurately predicted the trend of increasing failure depth with slope but did not accurately predict the values we observe in our experiments. This has implications for the relative hazard associated with shallow and steep slopes, particularly where soils are thick.

Finally, the occurrence of an aspect ratio consistent with field observations ($L/W \approx 2$), indicates that this persistent value may not result from characteristic hillslope or channel geometries. Instead, this aspect ratio may result from some critical combination of marginal stresses and soil heterogeneities, both of which scale with failure length. If true, this observation would effectively simplify slope stability predictions from a 3-D to a 2-D problem.

Acknowledgements

This chapter is in preparation for publication in a peer-reviewed journal with co-authors Michael P. Lamb, Marisa Palucis, and Jeremy Venditti. Brian Fuller helped greatly with the experimental design and instrumentation. Jabari Jones helped to conduct several of the experiments. Our theoretical considerations benefitted from discussions with

David Milledge, Richard Iverson, Bill Dietrich, Jim Rice, and Melany Hunt. Funding for this work was provided by NSF Grant EAR-0922199 and EAR-1349115, the Terrestrial Hazards Observation and Reporting center (THOR) at Caltech.

4.7 References

Bear, Jacob (1972). *Dynamics of Fluids in Porous Media*. New York, NY: Elsevier.

Bellugi, Dino et al. (2015). "A spectral clustering search algorithm for predicting shallow landslide size and location." In: *Journal Of Geophysical Research-Earth Surface* 120.2, pp. 300–324.

Berti, M and A Simoni (2005). "Experimental evidences and numerical modelling of debris flow initiated by channel runoff." In: *Landslides* 2.3, pp. 171–182.

Burroughs, E. R. (1984). "andslide hazard rating for portions of the Oregon Coast Range." In: *Proceedings of the symposium on effects of forest land use on erosion and slope stability: Honolulu, University of Hawaii*, pp. 265–274.

Cannon, Susan H et al. (2008). "Storm rainfall conditions for floods and debris flows from recently burned areas in southwestern Colorado and southern California." In: *Geomorphology* 96.3-4, pp. 250–269.

Dai, FC and CF Lee (2002). "Landslide characteristics and slope instability modeling using GIS, Lantau Island, Hong Kong." In: *Geomorphology* 42.3, pp. 213–228.

Dietrich, WE et al. (2007). "The prediction of shallow landslide location and size using a multidimensional landslide analysis in a digital terrain model." In: *C. L. Chen and J.J. Major (editors), Debris-Flow Hazards Mitigation: Mechanics, Prediction,*

and Assessment: Proceedings 4th International DFHM Conference, Chengdu, China, September 10-13, 2007, pp. 1–12.

Eckersley, D (1990). "Instrumented laboratory flowslides." In: *Geotechnique* 40.3, pp. 489–502.

Haefeli, R (1948). "The stability of slopes acted upon by parallel seepage." In: *International Conference on Soil Mechanics and Foundation Engineering*, pp. 57–62.

Iverson, R M, M E Reid, and R G LaHusen (1997). "Debris-flow mobilization from landslides." In: *Annual Review of Earth and Planetary Sciences* 25, pp. 85–138.

Iverson, R M et al. (2000). "Acute sensitivity of landslide rates to initial soil porosity." In: *SCIENCE* 290.513.

Iverson, Richard M and Jon J Major (1986). "Groundwater Seepage Vectors and the Potential for Hillslope Failure and Debris Flow Mobilization." In: *Water Resources Research* 22.11, pp. 1543–1548.

Jaky, J. "The coefficient of earth pressure at rest. (in Hungarian)." In: *J. Soc. Hung. Eng. Arch. (Magyar Mernok es Epitesz-Egylet Kozlonye)*, pp. 355–358.

Kean, J, D M Staley, and S H Cannon (2011). "In situ measurements of post-fire debris flows in southern California: Comparisons of the timing and magnitude of 24 debris-flow events with rainfall and soil moisture conditions." In: *Journal of Geophysical Research* 116.F04019.

Lambe, T W and R V Whitman (1969). *Soil Mechanics*. New York, NY: John Wiley & Sons.

Lu, Ning and Jonathan Godt (2008). "Infinite slope stability under steady unsaturated seepage conditions." In: *Water Resources Research* 44.11.

Milledge, David G et al. (2014). "A multidimensional stability model for predicting shallow landslide size and shape across landscapes." In: *Journal Of Geophysical Research-Earth Surface* 119.11, pp. 2481–2504.

Montgomery, David R et al. (2009). "Instrumental record of debris flow initiation during natural rainfall: Implications for modeling slope stability." In: *Journal Of Geophysical Research-Earth Surface* 114.F, F01031.

Montgomery, DR and WE Dietrich (1994). "A Physically-Based Model for the Topographic Control on Shallow Landsliding." In: *Water Resources Research* 30.4, pp. 1153–1171.

Moriwaki, H (1993). "Behavior of pore-water pressure at slope failure." In: *Proceedings of the seventh International Conference and Field Workshop on Landslides in Czech and Slovak Republics. Landslides, Balkema, Rotterdam.* Proceedings of the Seventh International Conference & Field Workshop on Landslides, pp. 263–268.

Moriwaki, H et al. (2004). "Failure processes in a full-scale landslide experiment using a rainfall simulator." In: *Landslides* 1.4, pp. 277–288.

Okura, Yoichi et al. (2002). "Landslide fluidization process by flume experiments." In: *Engineering Geology* 66.1-2, pp. 65–78.

Petley, David (2012). "Global patterns of loss of life from landslides." In: *Geology* 40.10, pp. 927–930.

Prancevic, J P, M P Lamb, and B M Fuller (2014). "Incipient sediment motion across the river to debris-flow transition." In: *Geology* 42, pp. 191–194.

Reid, ME, RG LaHusen, and RM Iverson (1997). "Debris-flow initiation experiments using diverse hydrologic triggers." In: *Debris-Flow Hazards Mitigation, Proceedings, C. Chen, ed., American Society of Civil Engineers*, pp. 1–11.

Reneau, SL and WE Dietrich (1987). "Size and location of colluvial landslides in a steep forested landscape." In: *IAHS-AISH publication* 165, pp. 39–48.

Rickenmann, D and M Zimmerman (1993). "The 1987 debris flows in Switzerland: documentation and analysis." In: *Geomorphology* 8, pp. 175–189.

Schmidt, K M et al. (2001). "The variability of root cohesion as an influence on shallow landslide susceptibility in the Oregon Coast Range." In: *Canadian Geotechnical Journal* 38.5, pp. 995–1024.

Skempton, A W and F A DeLory (1957). "Stability of natural slopes in London clay." In: *International Conference on Soil Mechanics 2*, pp. 378–381.

Stock, Jonathan D and William E Dietrich (2006). "Erosion of steepland valleys by debris flows." In: *Geological Society of America Bulletin* 118.9-10, pp. 1125–1148.

Stock, Jonathan D and Dino Bellugi (2011). "An Empirical Method to Forecast the Effect of Storm Intensity on Shallow Landslide Abundance." In: *5th International Conference on Debris-Flow Hazards Mitigation: Mechanics, Prediction, and Assessment.*

Takahashi, T (1978). "Mechanical Characteristics of Debris Flow." In: *J Hydr Eng Div-ASCE* 104.HY8, pp. 1153–1169.

Taylor, D W (1948). *Fundamentals of Soil Mechanics*. New York, NY: John Wiley & Sons.

Taylor, Faith E, Bruce D Malamud, and Annette Witt (2015). "What Shape is a Landslide? Statistical Patterns in Landslide Length to Width Ratio." In: *EGU General Assembly Conference Abstracts, Vienna*. Vol. 17.

USGS (2005). "Landslide Hazards–A National Threat." In: *United States Geological Survey Fact Sheet* 2005-3156.

Waldron, L J and Suren Dakessian (1981). "Soil Reinforcement by Roots: Calculation of Increased Soil Shear Resistance From Root Properties." In: *Soil Science* 132.6, p. 427.

Wang, Gonghui and Kyoji Sassa (2003). "Pore-pressure generation and movement of rainfall-induced landslides: effects of grain size and fine-particle content." In: *Engineering Geology* 69.1-2, pp. 109–125.

Yagi, N and R Yatabe (1987). "Prediction method of slope failure in sandy soil due to rainfall." In: *Proceedings, 8th Asian Regional Conference on Soil Mechanics and Foundation Engineering*, pp. 217–220.